NANOSTRUCTURED POLYMERS FOR ADDITIVE MANUFACTURING

Antigoni Paspali

A thesis submitted in partial fulfilment of the

requirements of London South Bank University

for the degree of Doctor of Philosophy

April 2019

School of Engineering

London South Bank University

Contents

Contents i

Acknowledgements v

Publications vii

Abstract viii

Abbreviations x

List of figures xii

List of tables xvi

Chapter 1: Introduction 18

1.1 Motivation and problem statement 18

1.2 Research aim and objectives 20

1.3 Thesis outline 20

Chapter 2: Literature review 22

2.1 Stereolithography (SLA) 23

2.2 Powder-bed 3D printing 24

2.3 Selective laser sintering (SLS) 24

2.4 Fused filament fabrication 24

2.4.1 Process overview 25

2.4.2 Important process parameters 27

2.5 Polymer/clay nanocomposites 30

2.5.1 Clays 32

2.5.2 Polymer matrix 38

2.6 Polymer/clay nanocomposites in 3D printing 40

2.6.1 Preparation of polymer/clay nanocomposite filaments 41

2.6.2 Characterisation of polymer/clay nanocomposites 42

Chapter 3: Methodology 45

3.1 Introduction 45

3.2 Materials 45

3.3 Compounding and filament extrusion 49

3.4 Design of test specimens 51

3.5 3D printer 52

3.5.1 Overview 52

3.5.2 Tool path generation 53

3.5.3 Calibration 54

3.6 Experimental design 54

3.6.1 3D printing of neat PLA 55

3.6.2 3D printing of PLA/clay and PLA/grafted-PLA/clay composites 59

3.7 Characterisation of 3D printed samples 59

3.7.1 Mechanical characterisation 59

3.7.2 Structural characterisation 61

3.7.3 Melt flow rate 61

3.7.4 Die swell ratio 62

3.8 Statistical analysis 62

3.8.1 One-way ANOVA 63

3.8.2 Independent-samples t-test 64

Chapter 4: Optimisation of printing parameters 66

4.1 Effect of infill orientation 66

4.2 Effect of layer thickness 70

4.3 Effect of infill density 74

4.4 Summary 76

Chapter 5: 3D printing of PLA/Cloisite nanocomposites 78

5.1 Selection of PLA Ingeo:clay composite system 78

5.2 Tensile properties of printed PLA/clay composites 81

5.3 Flexural properties of printed PLA/clay composites 85

5.4 Structure 88

5.4.1 Mesostructure of PLA/Cloisite composites 88

5.4.2 Micro- and nanostructure of PLA/Cloisite composites 91

5.5 Modelling the elastic modulus of PLA/Cloisite composites 93

5.6 Effect of clay intercalation on the mechanical performance of PLA/Cloisite composites 96

5.7 Summary 99

Chapter 6: 3D printing of PLA/Garamite nanocomposites 100

6.1 Mechanical properties 101

6.2 Structure and rheology 104

6.3 Summary 107

Chapter 7: 3D printing of MAH-g-PLA/PLA/clay composites 108

7.1 MAH-g-PLA/Clo5 system 108

7.2 MAH-g-PLA/GA system 112

7.3 Summary 117

Chapter 8: Conclusion 118

8.1 Conclusions 118

8.2 Original contribution to knowledge 120

8.3 Recommendations 122

References 123

Appendix 136

Material database 136

Acknowledgements

The last three years have been a period of intense learning for me, not only on a professional/educational level but also on a personal level. I would like to reflect on the people who have supported and helped me so much throughout this period.

I would first like to thank my supervisors at London South Bank University, School of Engineering, Professor Yuqing Bao and Professor David Gawne for their ongoing support, academic guidance and positive vibes. You definitely provided me with the tools that I needed to make the right choices and successfully complete my PhD. Thank you for your excellent cooperation, for listening and for giving me the chance to carry out this research project.

This PhD project would not have been possible without the support of BYK Chemie GmbH, in terms of feedstock filaments and materials, analytical tests and know-how. In specific, I am grateful to Dr Frederik Piestert and Dr Sebastian Reinelt for their excellent collaboration. I really enjoyed my secondment time in the BYK Chemie facilities in Wesel, Germany, and gained useful hands-on experience on the filament processing.

I am also grateful to Mr Paul Elsdon for his technical assistance with the mechanical tests, to Mr Simon Black for his help in setting up the printing equipment, to Mr Mehdi Zahir for his assistance with repairing the 3D printer, and to Mr Silvio Lavandeira for his help in designing 3D CAD models. I would also like to thank Dr Ousmane Oumar and Professor Mohammad Tokhi for providing me with plenty of physical space to perform my experiments.

Many thanks to my colleagues and London besties: Dr Ridouan Chaouki, Dr Ousmane Oumar, Dr Hassan Zabihi and Mr Farzin Vajihi, for their wonderful collaboration at the office and the quality time we spent together at LSBU. Last but

not least, I would like to thank my parents, Chris and Catherine, and my sister, Anastasia, for their sympathetic ear and support. You have always been there for me and I am grateful to you.

Thank you very much, everyone!

Antigoni Paspali

Publications

A. Paspali et al., *The influence of nanostructure on the mechanical properties of 3D printed polylactide/nanoclay composites*, Composites Part B: Engineering, Volume 152, 1 November 2018, Pages 160-168

A. Paspali et al., *Effect of composition on the mechanical properties of 3D printed polymer nanocomposites*, 25th International Conference on Composites/Nano-Engineering (ICCE-25), Rome, Italy, July 16-22, 2017

A. Paspali et al., *Effect of infill morphology on the mechanical properties of 3D-printed polylactide*, London South Bank University, Postgraduate Research Summer School 2016, 11-15 July 2016, London, UK

Abstract

Fused filament fabrication (FFF) is one of the most widely employed techniques of additive manufacturing, which produces three dimensional (3D) printed objects by the layering of melt-extruded thermoplastic-based filaments. Despite its ease of use and environmentally friendly nature, FFF has so far only provided a narrow range of potential applications due to the limited number of materials (mostly thermoplastic-based composites, with metal or ceramic fillers) compatible with this technique. Another obstacle for the wider application of 3D printed parts is their inferior mechanical performance compared to that of their conventionally-manufactured counterparts. A strategy for overcoming this deficiency is by merging polymer/clay nanocomposites with 3D printing. However, the incorporation of clays in the nanocomposite feedstock filament usually incurs several processing challenges, including clay agglomeration to the detriment of the formation of the printed part. This research aims to provide a systematic investigation and understanding of the influence of clay fillers and additives (coupling agents) on the mechanical properties and morphology of 3D printed nanocomposites. A series of polylactide (PLA)/clay nanostructured composite filaments were developed and successfully printed by an open-source 3D printer based on FFF. The effect of filament composition on the mechanical properties and morphology was investigated and correlated with the extent of intercalation of different clay types. The mechanical behaviour of the printed composite samples was influenced significantly by the clay type and content. For example, the samples containing organoclay with the same clay content exhibited a higher modulus of elasticity and strength than those with natural clay. In addition, the Halpin-Tsai model was found to be successful in predicting the moduli of the PLA/clay systems. Based on the experimental results, the mechanical properties of

the PLA/clay composite systems were shown to be correlated to the extent of clay intercalation. An implication from the model is that clay intercalation was more effective as a reinforcement technique than raising the total clay content. Upon the introduction of Garamite clay in the polymer matrix, the flowability of the melt was improved followed by a decrease in the die swell ratio of the composite samples. As a consequence, the composite feedstock filaments provided an enhanced print resolution compared to neat PLA and resulted to a printed part with a more compact mesostructure. The research showed that the dispersibility of the nanophase was a general difficulty affecting nanocomposite performance. As a result, grafted PLA was added to act as a compatibiliser to the Garamite and Cloisite composite systems, in order to promote the dispersion of clays in the polymer matrix. It was found that the mechanism underlying the mechanical performance of the grafted PLA/PLA/clay composites was dependent on the clay morphology. Upon the addition of grafted PLA in the PLA/Cloisite composite, the mechanical properties were improved due to the increased interfacial interaction and wetting between PLA and Cloisite platelets. In the case of the PLA/Garamite system, however, the addition of various concentrations of grafted PLA did not substantially improve the mechanical properties. These findings could act as a guideline in the design and development of feedstock filaments for 3D printing.

Abbreviations

3D	Three dimensional
ABS	Acrylonitrile butadiene styrene
Al	Aluminium
AM	Additive manufacturing
ANOVA	Analysis of variance
Ca	Calcium
CAD	Computer-aided design
Clo116	Cloisite 116
Clo20	Cloisite 20
Clo5	Cloisite 5
FDM	Fused deposition modelling
FESEM	Field emission scanning electron microscope
FFF	Fused filament fabrication
GA	Garamite
K	Potassium
MAH	Maleic acid anhydride
MAH-g-PLA	Maleic acid anhydride-grafted polylactide
Mg	Magnesium
MMT	Montmorillonite
M_w	Molecular weight
MVR	Melt volume flow rate
Na	Sodium
OMMT	Organomodified montmorillonite

PLA	Polylactide
PP	Polypropylene
RepRapPro	Replicating rapid prototyper
SEM	Scanning electron microscope
SLA	Stereolithography
SLS	Selective laser sintering
STL	Standard triangle language
TEM	Transmission electron microscopy
TPO	Thermoplastic polyolefin

List of figures

1: Current application and potential of 3D printing by type of industry.

2: Basic steps of the FFF process.

3: Schematic of the FFF process.

4: a) 3D printed tensile test specimen. The layered structure is emphasized in the zoomed inset. b) Illustration of internal voids (circled) of 3D printed objects. c) Scanning electron microscope (SEM) micrograph of the fracture surface of printed ABS specimen, where air voids (dark triangular spots) are present.

5: Illustrations of three infill orientations; a) 0^{o}, b) 45^{o} and c) 90^{o}. The lines represent the printing toolpaths or polymer beads. The angle between the longest dimension of the specimen and the printing path of the infill defines the infill orientation.

6: Schematic of different types of nanofillers with the corresponding nanoscale dimensions noted.

7: Comparison of modulus reinforcement for composites of TPO with nanofiller (MMT) vs composites with talc.

8: Molecular structure of montmorillonite.

9: Organomodification of natural clays with ammonium cations.

10: Structures of polymer/clay composites.

11: Mechanism of (organo)clay dispersion during melt processing. The high shear forces applied to the system break up the aggregates of clay stacks to smaller stacks of clay platelets. Given that the affinities of the polymer and the clay match, the polymer chains diffuse into the interlayer space between the platelets, leading to the delamination of the clay platelets.

12: a) Structure of the MAH-grafted base polymer, and b) structure of maleic acid anhydride.

13: Schematic of the preparation of polymer/clay nanocomposite filaments.

14: Schematics of die swelling during the 3D printing process.

15: Twin-screw extruder system.

16: Filament extruder.

17: a) Schematics of the a) ASTM D638-10 Type IV tensile test specimen, b) the addition of circular pads in the corners of the specimens to prevent warping

during printing, and c) ISO 178:2003 flexural test specimen. All dimensions are in mm.

18: RepRapPro Huxley 3D printer.

19: Workflow of the process followed in 3D printing.

20: a) Typical sliced CAD model of a tensile test (dumbbell) specimen. The lines represent the printing paths or polymer beads. The angle between the longest dimension of the specimen and the printing path of the infill defines the infill orientation and b) Infill orientations tested.

21: a) Tensile test setup with extensometer attached on the specimen, and b) bending test setup. All noted dimensions are in mm.

22: Typical stress-strain curves of 3D printed PLA samples for each infill orientation.

23: Digital images of 3D printed PLA with the following infill orientations: a) 0^o, b) 45^o, c) 90^o, and d) $0^o/90^o$, showing the through-thickness fracture after tensile test.

24: FESEM micrographs of the fracture surface of 3D printed PLA dumbbell specimens with a) 0^o, b) 45^o, c)90^o, and d) $0^o/90^o$ infill orientation. Illustrations of each corresponding cross-section are depicted in the insets.

25: Printing time of 3D printed PLA specimens vs layer thickness.

26: a) Modulus of elasticity and b) tensile strength of 3D printed PLA specimens vs layer thickness.

27: FESEM micrographs of the fracture surface of 3D printed PLA dumbbell specimens with a layer thickness of a) 0.1mm, b) 0.2mm, c) 0.3mm, and d) 0.4mm.

28: Printing time of 3D printed PLA specimens vs infill density.

29: a) Modulus of elasticity and b) tensile strength of 3D printed PLA specimens vs infill density.

30: Digital images of 3D printed PLA with the following infill densities: a) 25%, b) 50%, c) 75%, and d) 100%, showing the through-thickness fracture after tensile test.

31: a) Modulus of elasticity/printing time per specimen and modulus of elasticity/weight per specimen vs infill density, and b) tensile strength/printing time and tensile strength/weight vs infill density.

32: FESEM micrograph of the fracture surface of a neat PLA specimen after the tensile test, printed using the optimal parameters.

33: Typical stress-strain curves of 3D printed PLA samples.

34: Digital images of 3D printed a) PLA 2003D and b) PLA 3251D specimens, showing the through-thickness fracture after the tensile test.

35: Typical tensile stress-strain curves of 3D printed neat PLA and PLA/clay samples for clay content of a) 1 wt%, and b) 5 wt%.

36: Digital images of 3D printed a) PLA 2003D and b) PLA/clay composite specimens, showing the through-thickness fracture after tensile test.

37: Typical flexural stress-strain curves of 3D printed neat PLA and PLA/clay samples.

38: FESEM micrographs of the fracture surface of 3D printed dumbbell specimens of a) PLA/1wt% Clo5, b) PLA/5wt% Clo5, c) PLA/1wt% Clo20, d) PLA/5wt% Clo20, e) PLA/1wt% Clo116 composite specimens, and f) neat PLA.

39: Porosity of the 3D printed PLA/clay composites and neat PLA samples.

40: a) Typical SEM micrograph of organomodified Cloisite powder, and b) typical TEM micrograph showing the dispersion of clay platelets in the polymer matrix.

41: Normalised modulus of elasticity (Ec/Em) for the PLA/clay composites, as determined from both experimental measurements and theoretical calculations based on the Halpin-Tsai model for a) Clo5 and Clo20 and b) Clo116 composite samples.

42: Typical SEM micrograph of organomodified clay powder of Garamite 1958.

43: Typical tensile stress-strain curves of 3D printed neat PLA and PLA/GA samples for clay content of a) 1 wt%, and b) 5 wt%.

44: FESEM micrographs of the fracture surface of 3D printed dumbbell specimens of a) 1wt% and b) 5wt% GA in PLA 2003D.

45: Typical stress-strain curves for neat PLA2003D, PLA/ Clo5 (5wt%) and MAH-g-PLA (10wt%)/PLA/Clo5 (5wt%) composites.

46: Schematics of possible reaction mechanism for PLA, MAH-g-PLA and Cloisite clay.

47: FESEM micrographs of the fracture surface of 3D printed dumbbell specimens of Clo5-based nanocomposites: a) PLA/Clo5(5wt%) and b) MAH-g-PLA(10wt%)/PLA/Clo5(5wt%).

48: Typical stress-strain curves for neat PLA2003D, PLA/ GA (5wt%) and MAH-g-PLA (10wt%)/PLA/GA (5wt%) composites.
49: a) Modulus of elasticity, b) tensile strength, and c) ductility of the printed neat PLA and MAH-g-PLA/PLA/GA(5wt%) composites.

50: FESEM micrographs of the fracture surface of 3D printed dumbbell specimens of PLA 2003D based nanocomposites at 5wt% GA content, and the following content of MAH-g-PLA: a) 10wt%, b)7.5wt%, c) 5wt% and d)2.5wt%.

List of tables

1: Typical properties of PLA grades employed in current work.

2: Typical properties of clay fillers employed.

3: Composition of PLA 2003D-based feedstock filaments employed in this work.

4: Composition of PLA 3251D-based feedstock filaments employed in this work.

5: Specifications of RepRap Huxley printer.

6: General printing parameters used in 3D printing.

7: Printing parameters used in the 3D printing of PLA specimens during the optimisation process of the infill orientation. The varied parameter is in bold.

8: Printing parameters used in the 3D printing of PLA specimens during the optimisation process of the layer thickness. The varied parameter is in bold.

9: Printing parameters used in the 3D printing of PLA specimens during the optimisation process of the infill density. The varied parameter is in bold.

10: Printing parameters used in the 3D printing of nanocomposites.

11: Structure of one-way ANOVA results in SPSS.

12: Tensile properties of the printed PLA samples with different infill orientations.

13: Optimised printing parameters used in the 3D printing of polymer/clay composite filaments.

14: Tensile properties of the printed neat PLA and PLA/clay composite samples.

15: Tensile properties of the printed PLA 2003D/Cloisite samples and results of t-tests (p-value).

16: Flexural properties of the printed samples and results of t-tests (p-value).

17: Composition of the PLA/clay filaments investigated.

18: Tensile properties of the printed PLA 2003D Garamite samples and results of t-tests (p-value).

19: MVRs and die swell ratios of neat PLA 2003D and PLA/clay composite samples.

20: Tensile properties of the printed neat PLA and MAH-g-PLA/PLA/clay composites and results of t-tests.

Chapter 1: Introduction

1.1 Motivation and problem statement

Additive manufacturing (AM) or three-dimensional printing (3D printing) is a group of manufacturing techniques that are based on a revolutionary technology that creates 3D physical objects from digital designs. Some of the benefits offered by 3D printing are the minimum material waste, its ease of use, and the ability to obtain objects of high complexity within one fabrication step [1]. 3D printing is currently in the spotlight of both the industry and the academia worldwide, due to its versatile applications and potential in a diverse range of fields, including but not limited to car and aircraft manufacturing, prosthetics and orthodontics, architecture and consumer products manufacturing [2].

At present, one of the most widely employed 3D printing techniques is fused filament fabrication (FFF), which produces components or prototypes by the layering of melt-extruded thermoplastic feedstock filaments[1]. Due to the melting and extrusion involved in the process, only thermoplastic or thermoplastic-based materials with suitable thermal, rheological and mechanical properties are at present compatible with FFF [3-5]. This limitation narrows down the utilisation of printed parts to low or non-load bearing applications such as spare parts or custom tools and manufacturing aids [6], as well as prototypes in architecture and design [7].

[1]FFF is based on fused deposition modeling (FDM), which was originally developed and patented by Stratasys Inc. FFF is a synonymous term to FDM and was introduced in order to overcome any legal constraints imposed by the trademark FDM© of Stratasys [8]. *FFF* is used in this work to describe the aforementioned printing process. The objects obtained through the FFF process are referred to as *printed* objects.

A strategy for expanding the application range of FFF is the development of new composite printing materials by the introduction of nanomaterials (fillers) in the thermoplastic polymer feedstock (matrix). The formed polymer nanocomposites are expected to exhibit enhanced mechanical performance compared to the starting thermoplastic polymer [4,9-12]. Nanomaterials (such as nanotubes, nanofibres, nanoclays) are preferred to conventional fillers (such as talc, fibres, calcium carbonate), as they typically exhibit a weight advantage at low filler loadings [13,14].

Clays are a group of low-cost silicate nanofillers that have been widely employed in the synthesis of polymer nanocomposites. Polymer/clay nanocomposites exhibit improved properties relative to the polymer matrix, of which mechanical reinforcement is the most pronounced [11,15-17]. The incorporation of clays in the polymer feedstock usually involves several processing and fabrication challenges. Clay loading beyond a certain threshold can stimulate the agglomeration of clays and the deterioration of the mechanical properties of the nanocomposites, compared to the properties of the matrix [16,18,19]. In addition, clays alter the melt viscosity and the mechanical properties of the feedstock filament to the detriment of the formation of the printed part or the processability of the filament [3,5].

In order to preserve the processability of the feedstock filament upon the addition of clays, additives can be added for both enhancing the dispersion of clays in the polymer matrix and fine-tuning the properties of the feedstock material [9,20]. In this way, the feedstock filaments are expected to exhibit similar processability to the polymer matrix (and thus be compatible with FFF), as well as reinforced mechanical properties, due to the homogeneous dispersion of the clays in the matrix.

To date, the incorporation of polymer/clay nanocomposites in FFF is not a fully-explored field yet and so far has demonstrated only a few promising examples [11,21-

24]. The merging of polymer/clay nanocomposites with 3D printing could facilitate advances in both fields [5,10]. Thus, a systematic investigation and understanding of the influence of clays and additives in the mechanical properties and morphology of 3D printed nanocomposites are necessary.

1.2 Research aim and objectives

The aim of this work is to understand the mechanisms underlying the formation of high mechanical performance printed polymer/clay nanocomposites. This is a key step towards controlling the properties of the corresponding 3D printed parts and extending the applicability of FFF.

The key objectives are:

- Establishing process routes and design of polymer/clay nanocomposite feedstock materials for FFF.
- Optimising the printing parameters of polymer/clay nanocomposites, with regards to the quality of the final part.
- Performing mechanical and microstructural characterisation of the printed polymer/clay nanocomposites and identifying their performance mechanisms.
- Understanding the interplay between the mechanical, microstructural, and rheological properties of printed polymer/clay nanocomposites.

1.3 Thesis outline

The following work is organised in seven chapters. Chapter 2 includes a brief introduction in additive manufacturing, followed by a literature review on

polymer/clay nanocomposites and their applications in additive manufacturing. Chapter 3 comprises the research methodology and the experimental details, including information on the grade and properties of the employed materials, on the processing of feedstock filaments and the 3D printing of the composite samples, as well as insights on the utilised characterisation techniques and statistical analysis. In Chapter 4, the results of the optimisation of printing parameters are presented. The optimised printing parameters are employed in Chapters 5, 6 and 7 in order to 3D print the polymer/clay composite samples. Chapter 5 and Chapter 6 include the results and discussion of the mechanical and structural characterisation of the printed Cloisite and Garamite composites respectively. In Chapter 7, the results from introducing additives in the polymer/clay systems are discussed. The last Chapter includes the conclusions and original contribution to knowledge, as well as recommendations for future work.

Chapter 2: Literature review

AM processes create 3D objects additively from a digital model, by the selective joining of material, following a bottom-up approach, compared to traditional subtractive manufacturing techniques [1]. This fundamental difference -adding rather than subtracting- delivers a vast potential in transforming the manufacturing process. AM offers the ability to fabricate 3D objects with complex geometries (in fact complexity is free) directly from a digital file, allowing thus for faster product redesign and process development. Multifarious printed structures can be obtained within one fabrication step, without the need for further assembling or machining, reducing both the production time and cost. AM is environmentally friendly, due to the reduced material waste and the ability to use recycled materials [1].

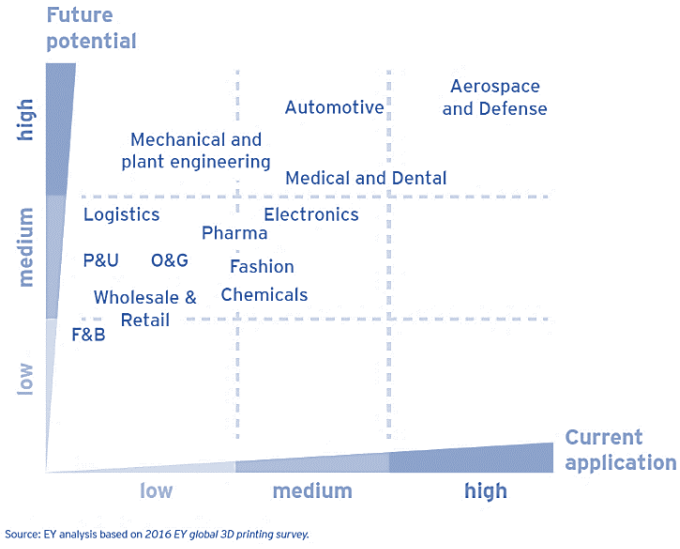

Figure 1: Current application and potential of 3D printing by type of industry [25].

Although the 3D printing hype is relatively new, the technology has actually been around for more than 30 years. Chuck Hull invented the first AM process called *stereolithography* in 1983. 3D printing was limited mostly to industrial uses until 2009 when the patent for FDM expired and the consumer 3D printing market took off [2].

The application range of 3D printing is even more remarkable. Recent global reports [25,26] reveal that AM exhibits applications in various fields including the aerospace, automotive, biomedical and electronics industries (Figure 1), with most applications being oriented towards product development, prototyping, innovation and fabrication of customised products [27].

Over the years, several 3D printing techniques have been developed, each one with its own advantages and limitations. Although most of them employ the same layer-by-layer deposition approach, the printing mechanism varies significantly among them. Below, the most established 3D printing techniques are presented.

2.1 Stereolithography (SLA)

This technique is based on photoinitiated polymerisation of a photocurable resin [4]. An ultraviolet (UV) laser beam is directed towards the desired printing path in the resin reservoir, and the photocurable resin polymerises into a 2D patterned layer. After each layer curing, the platform lowers down and another layer of uncured resin is placed on top of the solidified (cured) resin for subsequent curing [3,4]. Arylic and epoxy resins are some of the typical polymeric materials used in SLA. Photoinitiators and UV absorbers can be added in the resin to control the depth of polymerisation. The main advantage of SLA is the ability to print parts with high resolution. However, the high cost of this system is a main concern for industrial application [3].

2.2 Powder-bed 3D printing

This printing technology was patented by the Massachusetts Institute of Technology. It is based on powder processing. Powdered materials are spread on the build platform and then selectively joined together, in a 2D pattern, by a liquid binder, which is sprayed through an inkjet printhead. After the desired 2D pattern is formed, the build platform lowers and the next layer of powder is spread. The internal structure of the printed part can be controlled by controlling the amount of the deposited binder. The key advantage of this technology is the large variety of compatible materials, such as ceramic, metal, polymers and their composites. However, the limited printing resolution and possible contamination of the binder still remain a challenge of powder-bed 3D printing [3,4].

2.3 Selective laser sintering (SLS)

Selective laser sintering is similar to the powder-bed 3D printing technique, as they are both based on powder processing. Instead of using a liquid binder, in SLS, a high power laser beam selectively sinters the powder particles to fuse them together and form a 2D pattern. The printed materials can be supported by the powder itself, so overhangs can be printed without the use of supporting parts. The surface finish of SLS printed parts is better than powder-bed 3D printed parts, but still not as good as SLA printed parts. The printing cost is high, due to the expensive high power laser source used [3,4].

2.4 Fused filament fabrication

This is the employed 3D printing technique in this project. At present, one of the most widely employed 3D printing techniques is fused filament fabrication (FFF), followed closely by selective laser sintering (SLS) and stereolithography (SLA) [27]. FFF produces components or prototypes by the controlled layering of melt-extruded thermoplastic feedstock filaments onto a printing platform, where layers subsequently fuse together and rapidly solidify forming solid parts. Common materials used in FFF are polymeric filaments such as acrylonitrile butadiene styrene (ABS), polylactide (PLA), polyamide, polycarbonate, polypropylene (PP), and polyphenylsulfones. Among others, this technique has inexpensive maintenance and is office-friendly since FFF systems make no use of hazardous solvents.

2.4.1 Process overview

In its simplest form (Figure 2), the printing[2] process begins with a digital 3D model of the solid object to be printed. This model can be designed using a computer-aided design (CAD) tool and is then converted into a mesh of triangles (standard triangle language-STL file) that represents the surface of the solid model.

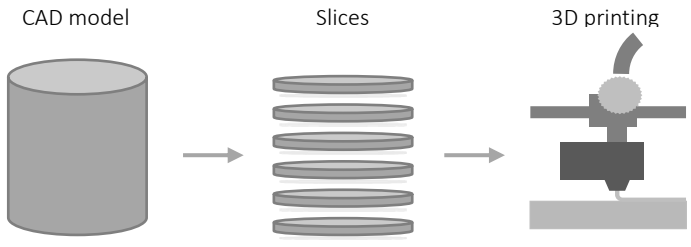

Figure 2: Basic steps of the FFF process

[2] From this point and throughout the rest of this work, *printing* or *3D printing* refer specifically to the FFF process.

The STL file is sliced down into a number of thin layers by a slicing software. Finally, the information is transformed into a file (g-code) readable by the printer. The final file is the printing plan and contains all the necessary information (in the form of generated tool paths) required by the printer, in order to build up a physical replica of the digital model [2,9].

Figure 3 illustrates the FFF process, in which a feedstock filament is supplied to the printer through a pinch roller mechanism. The filament is driven towards a heated nozzle where it melts. The upstream, still solid, filament acts as a piston, extruding the molten material through the nozzle, on top of the print platform, on a predetermined tool path created during the generation of the g-code [28].

The extruded polymer beads fuse with the adjacent ones, forming bonds through a thermally driven process and rapidly solidify [29]. The nozzle moves along the plane of the print platform, based on the generated tool paths in the g-code used, and it deposits material accordingly. Once a layer of extruded material has been printed, the nozzle moves upward by a fraction, where a new layer will be printed on top of the previous one [9]. The printer will continue adding layers on top of each other until the desired solid is obtained.

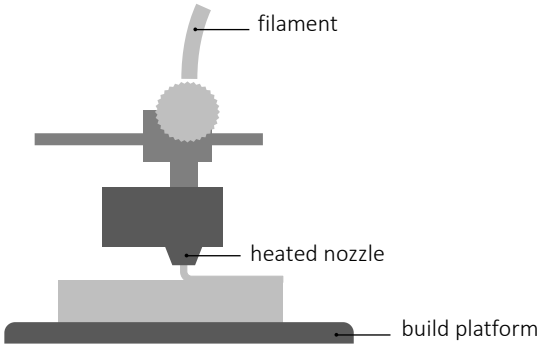

Figure 3: Schematic of the FFF process

3D printers based on FFF have proliferated on the market, since the expiration of the first FDM patent [30], as mentioned in Section 2.1. The self-replicating rapid prototyper (RepRapPro) [8] is a popular open-source, consumer-grade printer based on the FFF technology. Currently, several low-cost (<£500) printers are available on the market and are typically compatible with melt-extrusion of PLA, ABS and polyamide. Such printers have been employed in several research studies [31-35] for investigating the properties of parts printed by open-source printers in realistic environmental conditions, providing useful information to standard users. In fact, it has been reported that the mechanical performance of components printed by open-source 3D printers matches the performance of parts fabricated by industrial printing systems [34].

Due to the material limitation imposed by the extrusion involved in the printing process, FFF has so far demonstrated applications mostly in household items and consumer products and prototyping or non-load bearing components. Exotic applications include the fabrication of porous scaffolds with shape memory properties [36], nanocomposite earmuffs [21] or patient-specific implants [37].

2.4.2 Important process parameters

As shown in Figure 4a, printed parts can be considered as laminate composite structures with stacked layers of bonded polymer beads. The presence of air gaps (Figure 4b and 4c) is inherent to the printed objects due to the layering approach of the FFF (and lack of any compaction force) and the arrangement of the polymer beads within the layer. Studies on ABS [38-40], polypropylene [33], and polyether-ether-ketone [40] have revealed that printed parts exhibit inferior mechanical performance to their conventionally-fabricated counterparts (i.e. injection or compression-

moulded parts) due to the porosity and the reduced effective load-bearing area of the former. Therefore, the properties of the final printed objects are not solely controlled by the feedstock material, but also by the presence of air voids and the internal structure of the objects, which are in turn controlled by the process parameters and the generated printing tool paths [39,41].

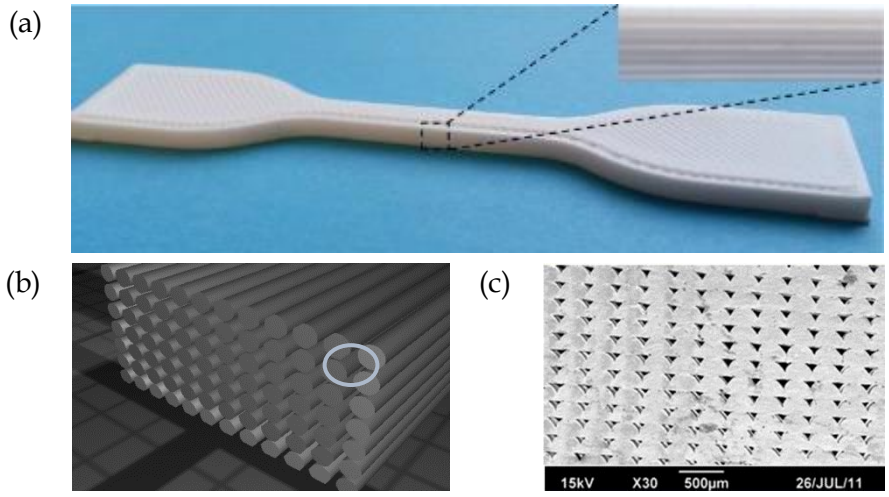

Figure 4: a) 3D printed tensile test specimen. The layered structure is emphasized in the zoomed inset. b) Illustration of internal voids (circled) of 3D printed objects. c) Scanning electron microscope (SEM) micrograph [41] of the fracture surface of printed ABS specimen, where air voids (dark triangular spots) are present.

Several experimental studies have investigated the effect of the process parameters on the mechanical properties of printed PLA [31-35,42-44], ABS [32,38-41,45] and composites [12,46-49]. The most important printing parameters that affect the mechanical performance of the printed parts are discussed below:

- *Infill orientation* is the pattern used to print each layer (Figure 5), i.e. the angle between the longitudinal dimension of the specimen and the printing direction. The infill orientation defines the internal mesostructure of the printed object. As

it was reported for both PLA and ABS, both the tensile strength and modulus of elasticity decrease, when the infill orientation increases (i.e. from 0° to 90°, suggesting an anisotropic mechanical response) [31,32,38,39,41]. In this case, the interfaces (which are weaker compared to the material within the polymer beads) between neighbouring polymer beads bear the tensile load, thus the printed parts are more likely to fail [31].

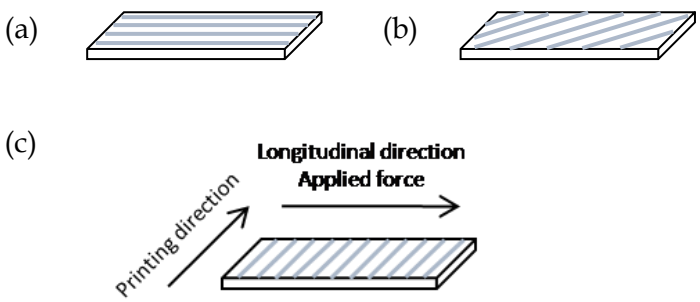

Figure 5: Illustrations of three infill orientations; a) 0°, b) 45° and c) 90°. The lines represent the printing toolpaths or polymer beads. The angle between the longest dimension of the specimen and the printing path of the infill defines the infill orientation.

- *Layer thickness* is the thickness of each layer in the printed part. A low value for the layer thickness delivers printed parts with better accuracy and smooth surface finish [31]. However, higher values require fewer layers to be printed, with fewer defects introduced, thus delivering stronger parts in a short time [42]. Therefore, the optimal value of layer thickness is determined by the desired surface quality, the mechanical properties, and the printing time.
- *Infill density* is the quantity of material the printer deposits inside the contour of the printed object. The higher the infill density, the higher the quantity of material deposited within the printed part. Furthermore, the greater the infill density, the

better the mechanical properties are, but at the cost of the printing time and material consumption [31,42].

The selection of the optimal printing parameters is usually a complex process, due to a large number of parameters involved in the process (e.g. print speed, print and platform temperature, infill/contour overlap, extrusion width etc...) and thus the difficulty in predicting the performance of printed objects. In general, printing parameters need to be optimised by taking into account the potential functionality of each object, for example when designing products with specific operational requirements [50], as mechanical properties of printed objects are direction-dependent. There is usually a trade-off between production time, surface finish, dimensional accuracy and mechanical properties [50].

2.5 Polymer/clay nanocomposites

As described in Section 2.2.2, a series of limitations inhibit the potential of FFF as a sustainable alternative to traditional manufacturing methods. There are in general two strategies to overcome such limitations and extend the applicability of FFF; the first strategy focuses on improving the process itself, while the second one focuses on the development of new feedstock materials with improved properties for 3D printing. The present work adopts the second strategy, towards the introduction of (nano)composite materials in FFF.

A material database (Appendix) of polymer composites studied in literature was constructed, focusing on the composite feedstock filaments employed in FFF. The list includes various combinations of fillers and matrices used so far in published studies. While there has been extensive research on micro-composites, only a few publications

have focused on printed polymer nano-composites and even fewer on polymer/clay nanocomposites.

A nanocomposite material with new (improved) properties can be obtained upon the introduction of nanosized fillers in the polymer feedstock. In such a system, the host matrix is usually a thermoplastic polymer that ensures compatibility with the printing process, whereas the dispersed nanofillers are plate-like fillers (such as nanoclays or graphene sheets), nanofibres (such as carbon nanotubes) or nanoparticles (such as silica particles or metal oxides) [51], as classified based on their dimensionality (Figure 6).

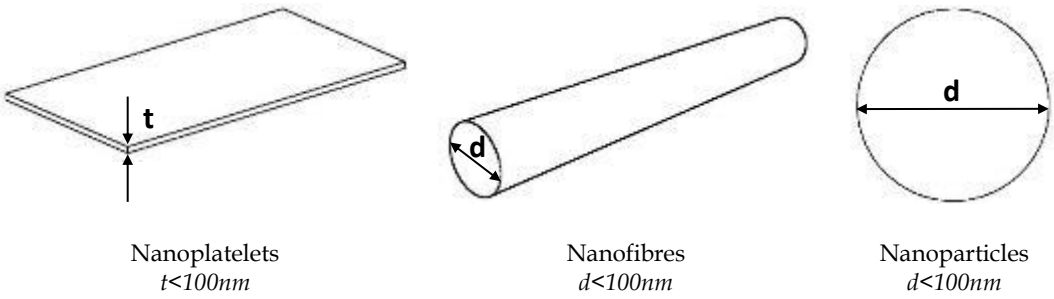

Figure 6: Schematic of different types of nanofillers with the corresponding nanoscale dimensions noted.

Nanofillers exhibit a weight advantage over conventional fillers, at very low nanofiller loadings. In the example below (Figure 7), increasing the modulus of the thermoplastic polyolefin (TPO) matrix by a factor of two requires approximately four times more mass of talc than that of montmorillonite (MMT, nanofiller) [13].

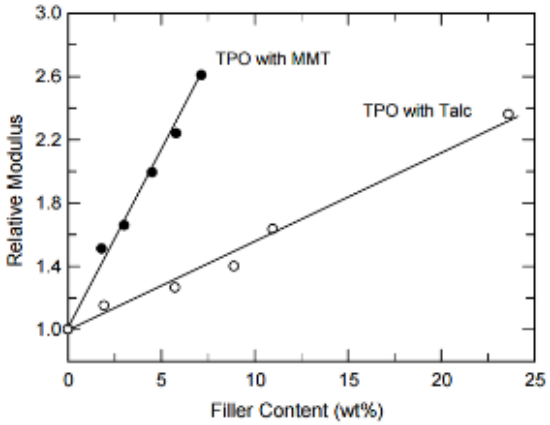

Figure 7: Comparison of modulus reinforcement for composites of TPO with nanofiller (MMT) vs composites with talc [13].

The key factors that affect the properties of a polymer nanocomposite are the nature and concentration of its components, the aspect ratio of the nanofiller, and the interfacial interaction between the nanofiller and the matrix. The high surface-to-volume-area of nanofillers along with their nanoscale dispersion within the matrix results to superior properties that have been exploited in diverse applications [52].

Polymer nanocomposites have received great attention, from both the industry and the academia, due to the combination of their superior mechanical, thermal and barrier properties with the ease of processability and their weight advantage [52]. Some of their most popular applications are in food and cosmetics packaging, in solar cells as well as in automotive parts [19].

2.5.1 Clays

Clay structure

Clays are a group of nanofillers that have been widely utilised in the preparation of polymer nanocomposites, due to their low cost, abundance and high aspect ratio.

Polymer/clay nanocomposites exhibit improved properties at low loading levels and a high level of processability [52]. Except for the mechanical reinforcement, polymer/clay nanocomposites have a broad field of applications that exploit their barrier properties, their flammability resistance, as well as their blend compatibilisation properties [53].

Layered silicates are clay-based nanofillers that consist of platelets of octahedral aluminium (Al)/magnesium (Mg) oxide sheets sandwiched between two tetrahedral silicate sheets (Figure 8) forming a 2:1 phyllosilicate layer, with a thickness of approximately 0.94nm [52,53]. When Al^{3+} ions in the octahedral sheet are partially replaced by Mg^{2+} ions (montmorillonite structure), the resulting negative charge is counterbalanced by sodium (Na), potassium (K) or calcium (Ca) cations located within the gallery between the layers (interlayer space) [53]. In a regular multilayer structure (clay stack), such as montmorillonite (MMT), the interlayer space is approximately 1nm thick. The thickness of one phyllosilicate layer and one interlayer space is equal to the d-spacing (d_{001}) of the clay stack (Figure 8). While the thickness of clay platelets is fixed, their lateral dimensions vary from 30 nm to several microns [52], which enables their high aspect ratio.

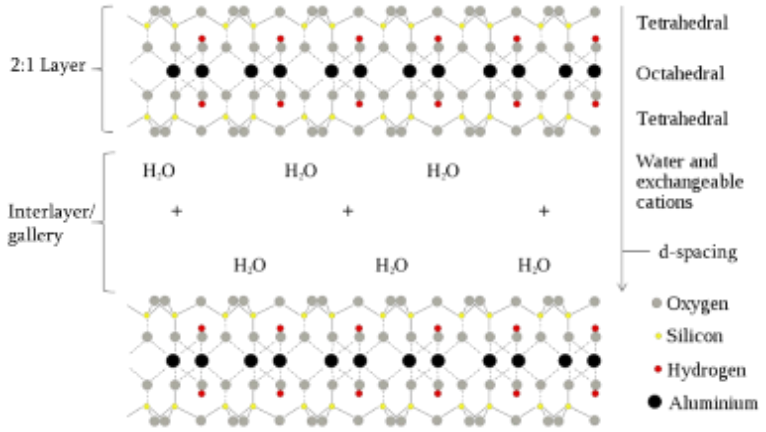

Figure 8: Molecular structure of montmorillonite [54].

Due to the weak electrostatic and Van der Waals interlayer forces, the cations can be hydrated, leading to swelling of the clays and increase of the interlayer space. Therefore, the clay platelets are soluble in water [52,53]. This intrinsic hydrophilicity of clays makes them incompatible with most polymers, which are hydrophobic. Therefore, the modification of clays with organophilic agents (organomodifiers) is necessary before the preparation of polymer/clay nanocomposites [52].

The organomodification of clay layers is performed through the exchange of Na cations with organic cations (such as ammonium cations, which have alkyl groups attached), forming organomodified clays (organoclays) (Figure 9) [53]. Common organomodifying agents act as surfactants (due to their amphiphilic nature), lowering the surface energy of clay platelets hence promoting favourable interactions with the hydrophobic matrix and the dispersion of the clay platelets.

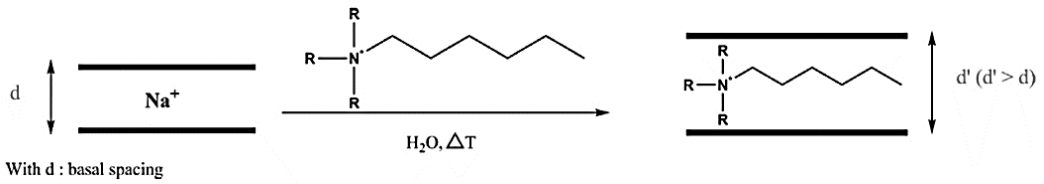

Figure 9: Organomodification of natural clays with ammonium cations [51].

The introduction of organic cations into the clay galleries not only it renders clays compatible with polymers, but also increases the interlayer space between clay platelets, promoting the intercalation of polymer chains into the galleries, during the preparation of polymer/clay nanocomposites [52]. As a result, the clay stacks can expand and delaminate into individual clay platelets in the polymer matrix. However, this is not always the case [53]. In fact, the dispersion of the organomodified clays in polymers depends on the nature of the clay and the organic

modifier, the polymer matrix employed, the thermodynamic affinity between the matrix and the clays as well as the preparation method [52].

Morphology of polymer/clay composites

Based on the dispersion degree achieved, the morphology of the obtained polymer/clay composite can be classified into three types, as illustrated in Figure 10:

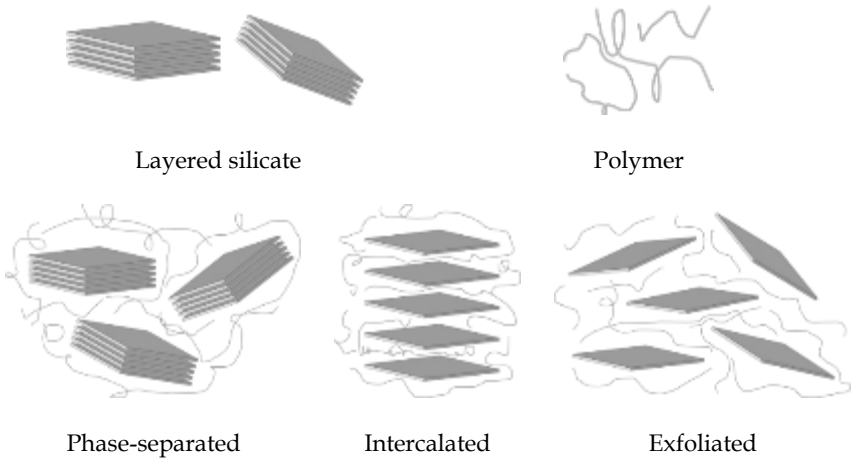

Figure 10: Structures of polymer/clay composites.

- *Phase-separated*: The clay is in the form of stacked platelets or aggregates of stacks in the polymer matrix, without separation of the platelets. This structure is common when mixing polymers with natural, unmodified clays. In this case, a microcomposite is obtained.
- *Intercalated*: Polymer chains are introduced into the organoclay galleries, increasing the interlayer space between the silicate layers, but the platelets are still stacked in a periodic array.
- *Exfoliated*: In this case, platelets are well-separated and dispersed as individual layers into the polymer matrix [52,53]. This morphology is desirable since it enables the exploitation of clays as reinforcing fillers [51].

The latter is the ideal scenario but is generally not fully achieved. Usually, the obtained morphology is a mixture of both the intercalated and exfoliated structures [51]. The dispersion and distribution state of the clays in the polymer matrix is a key factor that determines the extent of reinforcement of the obtained polymer/clay nanocomposites.

Preparation and mechanical properties of polymer/clay composites

Several methods have been developed for the preparation of polymer/clay nanocomposites, including melt intercalation, in-situ polymerisation, sol-gel processes or template synthesis [19]. The nanocomposites studied in this work have been prepared by melt compounding; therefore, the mechanism of clay intercalation and exfoliation during melt compounding are presented below.

During melt intercalation, the polymer matrix and the clays are mixed without the use of solvents. The mixture of the polymer melt and clays is annealed above the glass transition or melting point of the polymer usually under shear forces [19,51] (Figure 11). The stresses applied to the system break up solid clay particles (aggregates of clay stacks) to smaller dispersed stacks of clay platelets. Given that the affinities of the polymer and the clay match (role of organomodifier), the polymer chains diffuse into the interlayer space between the platelets, leading to the delamination of the clay platelets, forming thus nanocomposites with a range of structures [51,53,55].

As mentioned above, clays are introduced in polymers as reinforcing agents. Indeed, when properly dispersed, clays have been reported to improve either the tensile strength [11,16], the modulus of elasticity [11,15-17] or the elongation at break [16,18]. However, the opposite may occur. For example, Zaidi et al. [17] and Lai et al. [18] have reported that upon the addition of clays in the PLA matrix, a reduction in

the tensile strength occurs, that is related to the filler/matrix adhesion and the stress concentration around the clays.

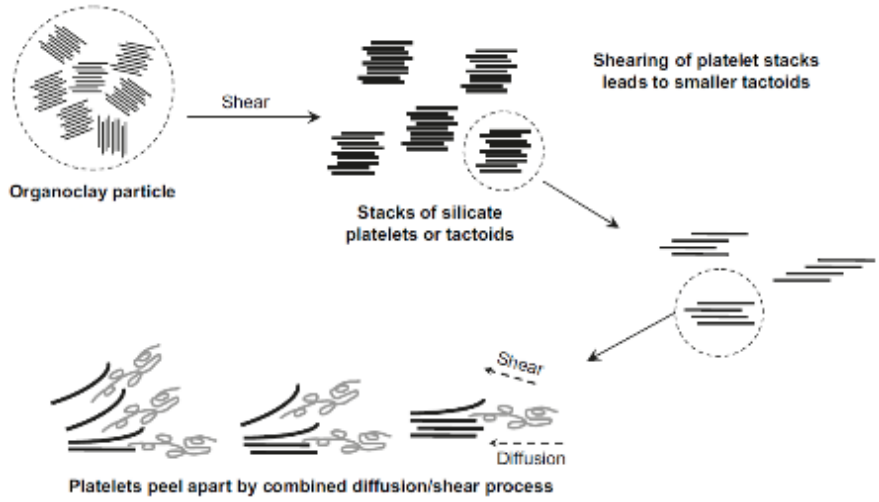

Figure 11: Mechanism of (organo)clay dispersion during melt processing [56]. *The high shear forces applied to the system break up the aggregates of clay stacks to smaller stacks of clay platelets. Given that the affinities of the polymer and the clay match, the polymer chains diffuse into the interlayer space between the platelets, leading to the delamination of the clay platelets.*

The mechanical properties of polymer/clay nanocomposites are controlled - to an extent - by the degree of exfoliation or intercalation of the clays in the polymer matrix and the interfacial interactions between them. When clay particles are highly dispersed in the matrix (intercalated/exfoliated form), a larger interfacial area becomes available between the rigid clays and the polymer, leading to strong interfacial interactions and enhanced stress transfer between the matrix and the nanofillers [52,57]. Any enhancement in the affinity between the clay and the polymer usually results in mechanical reinforcement [52]. In addition, the concentration of clays in the polymer matrix affects the mechanical reinforcement. As noted in the work of Pirani et al. [16] and Kontou et al. [15], there is an optimal concentration in

each case, for which the polymer nanocomposites exhibit the highest mechanical reinforcement. Above the optimal concentration, clay aggregates usually form, which lead to the deterioration of the mechanical properties. The optimal clay loading depends on the type of clays and the polymer matrix used and is usually met in the range of 1-5 wt% clay loading. Furthermore, the high aspect ratio nanoclays restrain the movement of polymer chains, leading to an improvement in the stiffness [57].

In order to promote further the incorporation of layered silicates in the polymer matrix, a coupling agent/compatibiliser can be added to the system of polymer and clays, which will act as a wetting agent between the nanofillers and the polymer [58]. A coupling agent can be a non-polar base polymer, which is functionalised with different monomers in a grafting process (Figure 12a). Maleic acid anhydride (MAH) is a polar monomer (Figure 12b), which has been utilised to improve the compatibility between the polymer and the filler. Specifically, it has been found that the addition of PLA grafted with maleic acid anhydride (MAH) at a low grafting percentage (e.g. 1 wt%) in a PLA/organoclay system improved the exfoliation degree of the clays [20] and the mechanical properties of the nanocomposites [20,59].

(a)

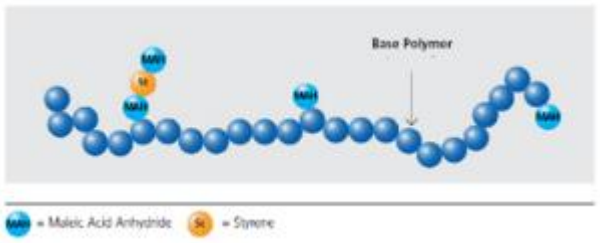

(b)

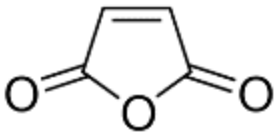

Figure 12: a) Structure of the MAH-grafted base polymer [60], and b) structure of maleic acid anhydride (source: sigma-aldrich).

2.5.2 Polymer matrix

The selection of the polymer matrix is crucial to polymer/clay composites designed for FFF, as the matrix usually determines the compatibility of the filament with the printing process. Since the polymer matrix is the main constituent of polymer/clay composites, its properties e.g. melt flow index, viscosity, etc… will play a dominant role during the preparation of the composite feedstock filament [9].

As it is concluded from the material database in the Appendix, ABS and PLA are the most common polymers employed in the preparation of polymer nanocomposite feedstock filaments for 3D printing. Compared to ABS, PLA is environmentally friendly, has a lower melting point, exhibits low warping, and higher strength, and does not require a heated build platform. These features turn it into an attractive material for the filament compounding industry. Therefore, attention was directed towards the study and utilisation of PLA here as an alternative, 'green' thermoplastic matrix.

PLA is an aliphatic polyester and a biodegradable, bioresorbable and biocompatible thermoplastic. It is derived from renewable resources, such as cornstarch or sugar canes. Its monomers can be produced on a mass scale through the microbial fermentation of agricultural by-products, mainly the carbohydrate-rich substances. Thus, it is a sustainable alternative to petrochemically derived polymers [61]. High molecular weight PLA is usually obtained through the ring-opening polymerization of lactide (an intermediate cyclic lactic acid dimer), utilising metal catalysts. Lactide comes under three stereoforms: L-lactide, D-lactide, or DL-lactide (50:50 mixture of L and D isomers). The degree of crystallinity of the final PLA product, and thus many of its properties, are determined by the ratio of D to L isomers [61]. Over the last decades, PLA/clay composites have been developed in

order to render PLA compatible with various industrial applications that require, for example, high impact strength.

2.6 Polymer/clay nanocomposites in 3D printing

The introduction of polymer/clay nanocomposites in FFF has not been studied extensively. Only few cases of such implementation are met in literature [11,21,22,24]. For example, Ahmadi et al. [21] investigated the acoustic performance of printed nanocomposite earmuffs, employing a feedstock filament of ABS/clay nanocomposite, with 4wt% clay concentration. The filament was obtained by melt-processing using a twin-screw extruder. The printed nanocomposite earmuffs exhibited better attenuation performance compared to pure ABS earmuffs, as well as weight advantage. Francis et al. [22] conducted a preliminary study on the mechanical properties and mesostructure of ABS/organomodified MMT (OMMT) nanocomposites, for various clay loadings (up to 3 wt%). A reduction in the porosity of the nanocomposite printed parts was observed compared to the pure ABS samples. Another published study on 3D printed ABS/OMMT nanocomposites [11] investigated the tensile, flexural, and thermal properties as well as the nanostructure of printed nanocomposite samples. It reported that the introduction of OMMT in the polymer feedstock improved both the tensile strength and the elastic modulus.

The quality of the feedstock filament plays a significant role in 3D printing. Ideally, the nanocomposite feedstock filaments should exhibit homogeneous dispersion of the fillers. As mentioned earlier in Section 2.3.1, the dispersion of the clays in the polymer matrix could be promoted through the organomodification of the clays and the grafting of molecules on the chain of the polymer matrix. In addition, the

mechanical properties of the feedstock filament are crucial to 3D printing, since low stiffness values, along with high viscosity, can lead to buckling of the filament and thus failure of the printing process. The properties of polymer/clay nanocomposite feedstock filaments can also be controlled by the proper selection of the additives and clay fillers [9].

Another challenge that needs to be addressed, when merging 3D printing with polymer/clay nanocomposites, is the viscosity (melt flow) at low and high shear rates. Ideally, high viscosity is needed at low shear rates (which will enable dimensional stability) and low viscosity is needed at high shear rates, which will ensure the processability of the composite filament. This rheological profile could be achieved by the addition of a thixotrope in the polymer matrix, such as the Garamite 1958 clay (Chapter 6). Formulations with Garamite exhibit a time-dependent shear-thinning behaviour (i.e. they are viscous under static conditions, but less viscous over time, when stressed). Clay fillers and grafted polymers are expected to modulate viscosity and preserve the processability of the feedstock material.

2.6.1 Preparation of polymer/clay nanocomposite filaments

Most published research on 3D printed polymer/clay nanocomposites reports the preparation of polymer/clay nanocomposite filaments through a two-step process, starting with the melt intercalation of the clay fillers in the polymer matrix for the formation of the polymer nanocomposite, followed by the filament extrusion of the obtained nanocomposite [11,21,22]. Figure 13 shows a schematic of this process.

Melt intercalation is an industrially sustainable method, as it is compatible with infrastructures common in the plastics industry, such as extrusion. Furthermore, it is considered an environmentally friendly technique, due to the absence of hazardous

solvents. During melt intercalation, the polymer, clays and any additives are mixed into a twin-screw extruder, where the polymer/clay nanocomposites are formed by melt intercalation [9,11,22,24,62], as mentioned in the Section 2.3.1.

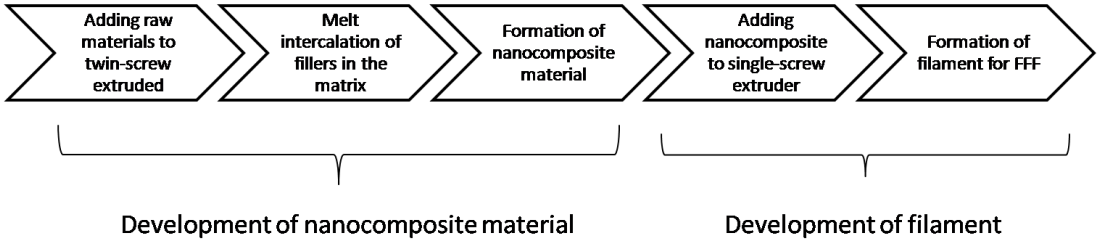

Figure 13: Schematic of the preparation of polymer/clay nanocomposite filaments.

The filament is then formed by extrusion of the polymer/clay composite through a single-screw extruder. Parameters such as the screw speed or the barrel and die temperature depend on the rheological and thermomechanical properties of the employed materials and are critical for the fabrication of homogeneous filaments with a consistent diameter [9].

2.6.2 Characterisation of polymer/clay nanocomposites

The investigation of mechanical properties is essential to predicting the functionality of 3D printed components or parts [9]. Most papers on 3D printed thermoplastics employ the ASTM D638-10 standard for investigating tensile properties [22,31,32,34,35,49]. However, it should be noted that, to date, there is neither an international standardised mechanical test procedure nor the suitable design protocol of test specimens for parts fabricated by FFF-based printing techniques [63].

Therefore, existing standards can only be treated as guidelines for the determination of the mechanical properties of printed samples.

Along with mechanical characterisation, structural characterisation of the fracture surface of the 3D printed polymer/clay composites by scanning electron microscopy (SEM) provides insights into the fracture patterns of printed parts, which can assist in understanding better their observed mechanical performance.

Investigating the rheology of the melt polymer/clay nanocomposites is also essential for accessing the printability of the composite filament and can provide insights into the relationship of the structure with mechanical properties. This would assist in designing composite feedstock materials with tailored properties, that are suitable for FFF, as well as in optimising the printing parameters for efficient part fabrication [58]. The melt flow rate is indicative of the flowability of a polymer melt and is often used as a quick alternative to viscosity [9,64]. In fact, the melt flow rate is inversely proportional to viscosity.

One of the most common features found during extrusion processes is the swelling of the extrudate, where the diameter of the extrudate (i.e. the material extruded through the nozzle of the 3D printer) appears to be larger than that of the nozzle [58]. The origin of this phenomenon is attributed to the difference in the pressure the melt material undergoes when leaving the nozzle. As shown in Figure 14, the melt is initially under stress within the nozzle, causing it to be elastically deformed. When the polymer melt leaves the nozzle, stress is relaxed (elastic recovery) leading to the radial expansion of the melt [28], thus reaching a diameter larger than that of the nozzle.

The die swell ratio is defined as the ratio of the maximum diameter of the extrudate to the diameter of the nozzle [28]. The die swell ratio is often used to quantify the

swelling behaviour of the extrudate. This swelling behaviour is affected by a series of factors, including the molecular structure, the temperature, the applied load, the ratio of the nozzle length to the diameter [64] etc…

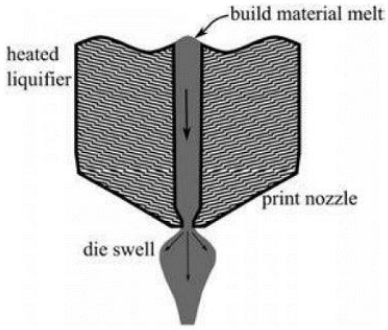

Figure 14: Schematics of die swelling during the 3D printing process [28].

The presence of nanofillers in the polymer melt, such as clays, will affect the rheology of the melt and therefore the die swell ratio. For example, the introduction of kaolin clay in PP has been found to cause a reduction of the die swell ratio of the composite material compared to that of the PP matrix, possibly due to the reduced mobility of the polymer chains caused by the presence of the rigid filler [58]. As both the die swelling and the rheology of the melt affect the final diameter of the extrudate, they will also affect the resolution of the printing process and thus the quality of the printed parts. Hence, the relationship between the melt flow and the die swelling of the polymer/clay nanocomposites needs to be further investigated.

Chapter 3: Methodology

3.1 Introduction

In this chapter, the details of the experimental procedure are presented. First, materials were selected based on the literature review conducted. These were processed at BYK Chemie GmbH to form pure thermoplastic, as well as nanocomposite filaments suitable for FFF. The effect of printing parameters on the mechanical properties and failure of printed neat thermoplastic samples were examined first by means of microscopy and mechanical tests. The nanocomposite specimens were then printed using the optimal printing conditions. The mechanical performance of the printed nanocomposites was then investigated with regards to their structure, in order to understand the evolution of properties upon the introduction of clay and additives in the polymer.

3.2 Materials

Two types of polylactide were used as the polymer matrix:

- *PLA Ingeo 2003D* (NatureWorks) (PLA 2003D), which is a high molecular weight ($M_w \approx 120$ kDa, [65]) and general-purpose extrusion grade polylactide [66]. Its typical properties are given in Table 1.
- *PLA Ingeo 3251D* (NatureWorks) (PLA 3251D), which is designed for injection moulding applications. This polymer grade has a higher melt flow capability than PLA 2003D [67]. Its typical properties are also given in Table 1.

Grafted PLA was utilised as a coupling agent, in order to improve the interfacial compatibility between the polymer matrix and the inorganic fillers and hence the dispersion of the fillers in the polymer matrix. Maleic acid anhydride (MAH) was used as the grafting polar monomer and MAH-grafted PLA (MAH-g-PLA) was obtained through a solid-state process patented by BYK Chemie. The utilised MAH-g-PLA is available by BYK Chemie under the trade name *TPPL 1112*.

Table 1: Typical properties of PLA grades employed in current work [65-68].

Physical Properties	**PLA 2003D**	**ASTM Method**	**PLA 3251D**	**ASTM Method**
Specific gravity	1.24	D792	1.24	D792
MFR, g/10 min (210^{o}C, 2.16kg)	6	D1238	80	D1238
Tensile yield strength, MPa	60	D882	62	D638
Tensile modulus, GPa	3.5	D882	-	-
Tensile elongation, %	6.0	D882	3.5	D638
Glass transition temperature, ^{o}C	-	-	55-60	D3418
Crystalline melt temperature, ^{o}C	210	-	155-170	D3418
Molecular weight (M_w), kDa	120		90-120	

The clay fillers (Table 2) employed for the preparation of PLA/clay nanocomposite filaments are available by BYK Chemie under the trade names:

- *CLOISITE 5 (Clo5)*: is bis (hydrogenated tallow alkyl) dimethyl, salt with bentonite [a type of layered silicate with the main constituent the MMT (smectite) structure] [69].
- *CLOISITE 20 (Clo20)*: is bis (hydrogenated tallow alkyl) dimethyl, salt with bentonite [70]. Both of these clays have been organomodified, for better intercalation and possibly exfoliation in the matrix.

- *CLOISITE 116 (Clo116)*: is natural bentonite [71]. All Cloisite clays exhibit a plate-like morphology.
- *GARAMITE 1958 (GA)*: is organomodified clay with a mixed clay morphology, consisting of both clay platelets and rods [72]. Its main constituents are the sepiolite and smectite structures. The typical properties of the raw nanofillers are given in Table 2.

Table 2: Typical properties of clay fillers employed [69,70-72].

Physical Properties	CLOISITE 5 (Clo5)	CLOISITE 20 (Clo20)	CLOISITE 116 (Clo116)	GARAMITE 1958 (GA)
Moisture, %	<3	<3	8-13	< 6
Typical dry particle size, µm	<40	<10	<15	-
Packed bulk density, g/l	480	175	340	130
Density, g/cm3	1.77	1.77	2.8	1.5 - 1.7
X-ray results, d001 in nm	3.27	3.16	1.25	-

3.3 Compounding and filament extrusion

Both the compounding and filament processing of the feedstock materials utilised were performed at BYK Chemie GmbH. For the preparation of PLA/clay (and grafted PLA) composites, masterbatches of 15wt% clay in PLA were prepared by melt intercalation, in order to ensure good dispersion of the clays in the matrix.

Prior to compounding, the clay powder, the PLA pellets and the grafted PLA pellets were dried in an oven, for at least 4 hours at 80°C. A co-rotating twin-screw extruder (Coperion ZSK 18, with a screw diameter of 18 mm and L/D ratio of 40, Figure 15) was employed for the preparation of the masterbatches. The screw speed was 300 rpm, the output 2 kg/h, while the processing temperatures ranged between 180°C to 200°C. The clay material was added via the side feeder of the extruder (screw speed of 60 rpm). The obtained granulated 15 wt% clay masterbatches were dried for 4 hours at 80°C. PLA/clay (and grafted PLA) composite filaments were produced by diluting the masterbatches with neat PLA to the desired concentrations, through melt compounding, following the process mentioned above.

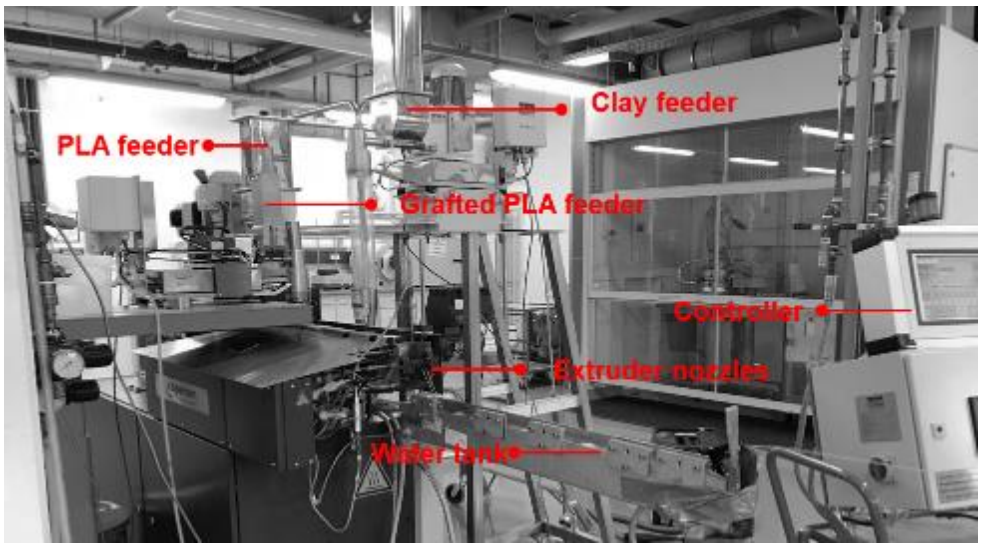

Figure 15: Twin-screw extruder system (BYK Chemie, Wesel)

The extruded nanocomposite pellets were dried and then fed into a single-screw filament extruder (NEXT, 3devo, Figure 16), where the filament was wound onto a spool as it was being extruded. The average filament diameter was 1.75mm ± 0.1mm. The composition of the composite filaments studied is shown in Table 3 and Table 4. In addition, neat PLA 2003D and 3251D filaments were prepared, in order to be used as a reference.

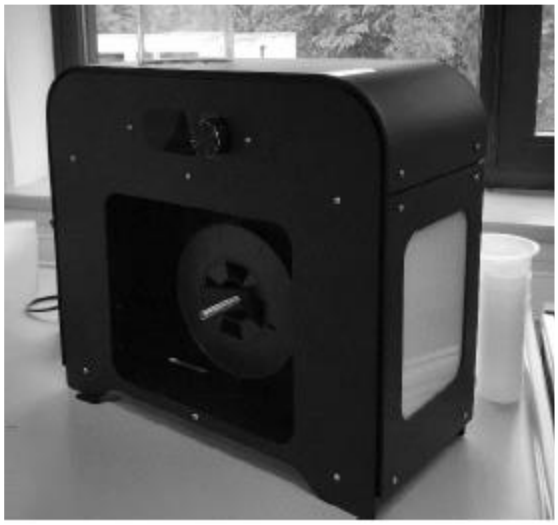

Figure 16: Filament extruder (BYK Chemie, Wesel)

Table 3: Composition of PLA 2003D-based feedstock filaments employed in this work.

Matrix type	Clay type	Clay content (wt%)
PLA 2003D	Clo5	1
PLA 2003D	Clo5	5
PLA 2003D	Clo20	1
PLA 2003D	Clo20	5
PLA 2003D	Clo116	1
PLA 2003D	GA	1
PLA 2003D	GA	5
PLA 2003D/MAH-g-PLA (10wt%)	Clo5	5
PLA2003D /MAH-g-PLA (10wt%)	GA	5
PLA2003D /MAH-g-PLA (7.5wt%)	GA	5
PLA2003D /MAH-g-PLA (5wt%)	GA	5
PLA2003D /MAH-g-PLA (2.5wt%)	GA	5

Table 4: Composition of PLA 3251D-based feedstock filaments employed in this work.

Matrix type	Clay type	Clay content (wt%)
PLA 3251D	Clo5	5

3.4 Design of test specimens

CAD models of tensile (Figure 17a) and flexural (Figure 17c) test specimens were designed following the ASTM (American Society for Testing Materials) D638-10 Type IV [73]and ISO 178:2003 [74] standard respectively. All CAD models were designed in AutoDesk Inventor Suite. Four cylindrical pads (0.5mm thick approximately) were added at the corners of the specimens (Figure 17b) to prevent warping during printing. These cylinders, though, were not a part of the specimen and were removed mechanically after the printing process was completed.

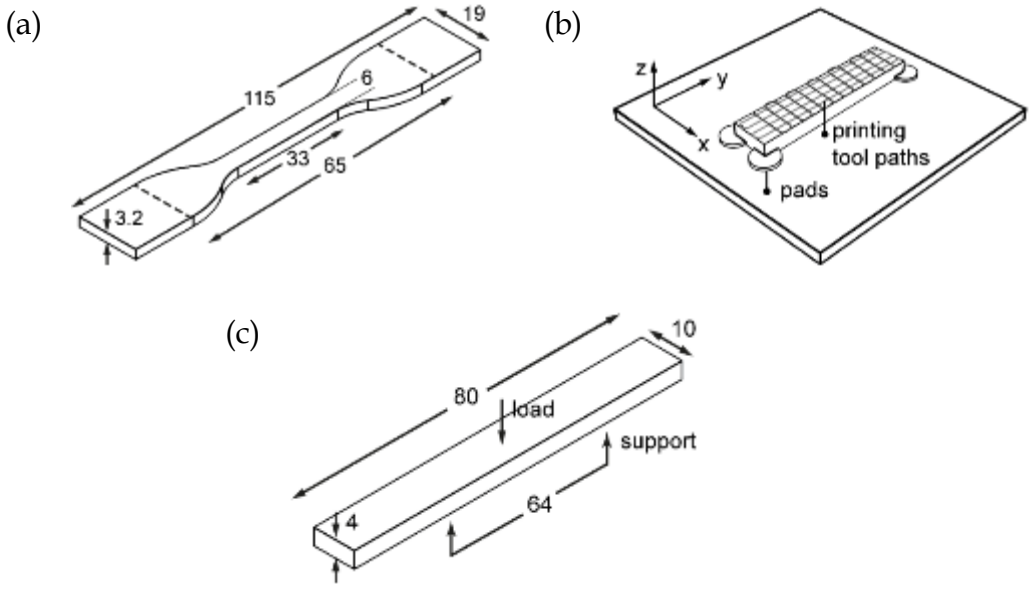

Figure 17: a) Schematics of the a) ASTM D638-10 Type IV tensile test specimen, b) the addition of circular pads in the corners of the specimens to prevent warping during printing, and c) ISO 178:2003 flexural test specimen. All dimensions are in mm.

3.5 3D printer

3.5.1 Overview

The 3D printer used in this study was the Huxley model (Figure 18), from the open-source RepRap Pro platform. The printer was provided by the Virtual Engineering Suite (VES), London South Bank University (LSBU). The basic elements of RepRap Pro Huxley are the printhead (extruder and cooling fan), the electronics' controller, the gantry, and the build platform (Figure 18). The specifications of the printer used in this work are given in Table 5.

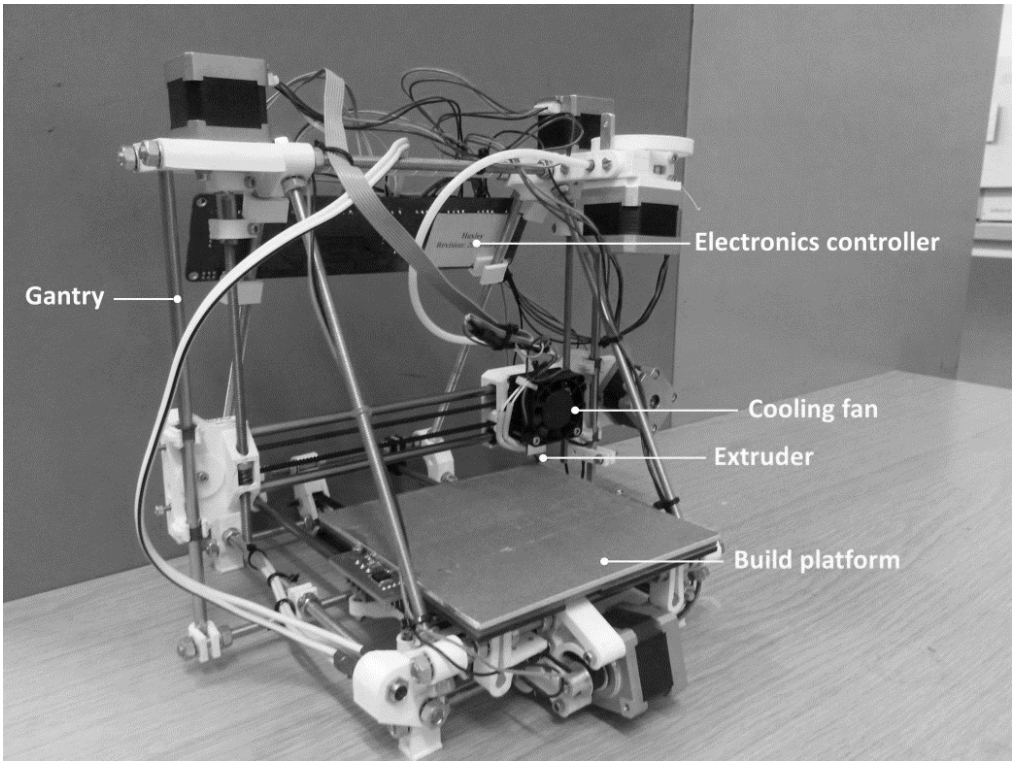

Figure 18: RepRapPro Huxley 3D printer

Table 5: Specifications of RepRap Huxley printer

Parameter	**Value**
Build volume (xyz), mm	140x140x95
Nozzle size, mm	0.5
Max. print speed, mm/s	60
Layer thickness, mm	0.1–0.5
Filament diameter, mm	1.75

3.5.2 Tool path generation

The 3D CAD models of the test specimens were formatted to an STL file, in which the surface of the 3D model is approximated with a series of linked triangles. The STL file was then loaded into Slic3r, which is a free open-source software used for the slicing of 3D models and the generation of the printing tool paths (Figure 17b). Finally, the generated g-codes were sent to the printer through Pronterface (a free

open-source software that controls the 3D printer) and the printing process was initiated. The flow of the described process can be seen in Figure 19. All programmes mentioned above are free and available online.

Figure 19: Workflow of the process followed in 3D printing.

3.5.3 Calibration

Prior to 3D printing, the printer was calibrated, in order to maximize the adhesion of the printed parts, particularly of the first layer, onto the build platform and avoid detaching and warping. The calibration process included:

- Levelling of the build platform in relation to the path of the extruder.
- Calibrating the distance between the extruder and the build platform in the z-direction. Ideally, the nozzle should barely touch the platform when the 3D printing process commences.

3.6 Experimental design

All specimens were printed in a build orientation such that the minimum part dimension (thickness) was aligned with the z-axis of the machine, i.e. perpendicular to the plane of the build platform, as shown in Figure 17b. Masking tape was applied on the build platform prior to the printing process, in order to provide sufficient adhesion of the extruded material (first layer) onto the surface of the platform. The build platform temperature was RT, as the use of masking tape does not require

heating of the build platform (the tape provides sufficient adhesion between the printed object and the platform).

3.6.1 3D printing of neat PLA

A preliminary study was conducted utilising neat PLA 2003D feedstock filament, in order to determine a set of optimal printing parameters, which would be used for 3D printing all nanocomposite samples. Variables like extrusion temperature or printing speed (Table 6) were at first selected based on the quality of the printed layers through visual inspection and the oozing of the nozzle (e.g. at an extruder temperature of 210^{o}C there was material oozing through the nozzle, due to the very low viscosity of PLA at this temperature). Subsequently, the infill orientation, layer thickness, and infill density were optimised, with regards to the mechanical properties of the obtained parts.

Table 6: General printing parameters used in 3D printing.

Printing parameters	**Value**
Extruder temperature, ^{o}C	200
Build platform temperature	RT, use of masking tape
Printing speed, mm/s	60
Perimeters	1

Infill orientation

In order to select the optimal infill orientation, PLA specimens were printed using four different infill orientations (Figure 20), based on the angle of the printed polymer beads (printing tool paths) relative to the longitudinal direction (direction of the

tensile force) of the tensile test (dumbbell) specimens. The infill orientations tested were:

- 0°: polymer beads aligned with the longitudinal dimension of the specimen
- 45°: polymer beads at 45° to the longitudinal dimension of the specimen
- 90°: polymer beads perpendicular to the longitudinal dimension of the specimen
- 0°/90°: cross-hatched polymer beads representing the default printing pattern

(a)

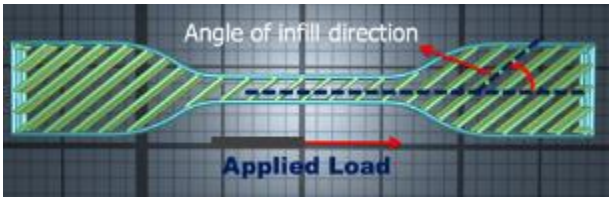

(b)

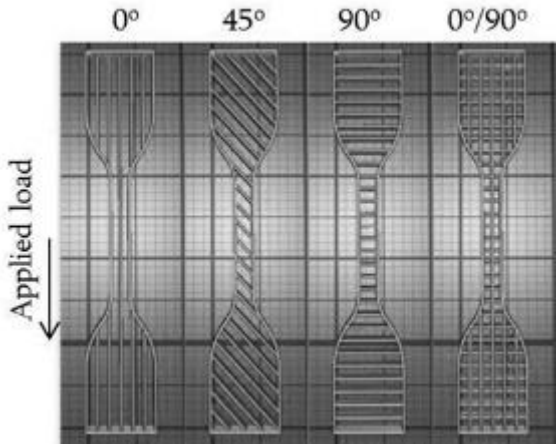

Figure 20: a) Typical sliced CAD model of a tensile test (dumbbell) specimen. The lines represent the printing paths or polymer beads. The angle between the longest dimension of the specimen and the printing path of the infill defines the infill orientation and b) Infill orientations tested.

Five dumbbell specimens were printed for each infill orientation. The rest of the printing conditions used are given in Table 7. All samples were printed with a 100% infill density (refers to the parameter in the slicing software, not the actual physical

density). This was chosen as it is the one that best mimics the compaction of samples produced by injection-moulding [33].

Table 7: Printing parameters used in the 3D printing of PLA specimens during the optimisation process of the infill orientation. The varied parameter is in bold.

Printing parameters	**Value**
Extruder Temperature, ^{o}C	200
Build platform temperature	ambient, use of masking tape
Printing speed, mm/s	60
Perimeters	1
Infill orientation, angle	**0°, 45°, 90°, 0°/90°**
Layer thickness, mm	0.2
Infill density, %	100

Layer thickness

In addition, five specimens were printed for each layer thickness tested, as shown in Table 8. In this case, a lower infill density of 50% was used, in order to have a faster printing process and reduced material consumption.

Infill density

Infill density defines the amount of material placed in the interior of a specimen. In this experiment, five PLA specimens were printed for each infill density tested, as shown in Table 9.

Table 8: Printing parameters used in the 3D printing of PLA specimens during the optimisation process of the layer thickness. The varied parameter is in bold.

Printing parameters	**Value**
Extruder Temperature, ^{o}C	200
Build platform temperature	23, use of masking tape
Printing speed, mm/s	60
Perimeters	1
Infill orientation, angle	0°/90°
Layer thickness, mm	**0.1, 0.2, 0.3 & 0.4**
Infill density, %	50

Table 9: Printing parameters used in the 3D printing of PLA specimens during the optimisation process of the infill density. The varied parameter is in bold.

Printing parameters	**Value**
Extruder Temperature, ^{o}C	200
Build platform temperature	23, use of masking tape
Printing speed, mm/s	60
Perimeters	1
Infill orientation, angle	0°/90°
Layer thickness, mm	0.3
Infill density, %	**25, 50, 75 & 100**

Table 10: Printing parameters used in the 3D printing of nanocomposites.

Printing parameters	**Value**
Extruder Temperature, ^{o}C	200
Build platform temperature	ambient, use of masking tape
Printing speed, mm/s	60
Perimeters	1
Infill orientation, angle	0°/90^{o}
Layer thickness, mm	0.3
Infill density, %	100

3.6.2 3D printing of PLA/clay and PLA/grafted-PLA/clay composites

The composite feedstock filaments listed in Table 3 and Table 4 were printed employing the parameters reported in Table 10. These values were selected based on the results of the optimisation process, which are described in the following chapter.

3.7 Characterisation of 3D printed samples

3.7.1 Mechanical characterisation

Tensile and flexural tests were performed on a Tinius Olsen H25KS universal testing machine following the ASTM D638-10 Type IV and ISO 178:2003 respectively. The system had a 5kN load capacity and a displacement resolution of 0.001mm.

Prior to tensile testing, specimens were secured between a clamped and a moving crosshead grip, with an initial distance of 65mm (Figure 21a), and the longest dimension of the samples being parallel to the crosshead movement. A direct contact extensometer (25mm gauge length) was attached to the gauge area of the specimens for recording the extension along the direction of the applied load. Tensile tests were run at a crosshead speed of 5mm/min until fracture occurred. The tensile strength and tensile strain were calculated from the obtained stress-strain curves, using the following equations (ASTM D638-10) [73].

$$\sigma_T = F_{max} / A_o \quad [1]$$

$$\% \varepsilon = \Delta L / L_o \times 100 \quad [2]$$

where σ_T is the tensile strength [MPa], F_{max} is the maximum load [N] sustained by the specimen, A_o is the average original cross-sectional area [mm^2] in the gauge length segment of the specimen, ε is % the tensile strain, ΔL is the increment of distance [mm] between the edges of the extensometer at any time and L_o is the gauge length of the extensometer (25 mm). The modulus of elasticity was equal to the slope of the tensile stress-strain curve in the strain interval between 0.05% and 0.25%.

Flexural tests (using a three-point bending configuration) were performed with a span length (distance between two supports) of 64mm (Figure 21b). The specimens were placed symmetrically on top of the supports and force was applied at midspan, while a deflectometer was recording the deflection on the bottom side of the specimen. Flexural tests were performed with a crosshead speed of 2 mm/min until fracture occurred. The flexural stress and strain were calculated using the following equations (ISO 178:2003) [74]:

$$\sigma_f = \frac{3FL}{2bh^2} \quad [3]$$

$$\varepsilon_f = \frac{6sh}{L^2} \quad [4]$$

where σ_f is the flexural stress, F is the applied load [N], L is the span [mm], b is the width of the specimen [mm], h is the thickness of the specimen [mm], ε_f is the flexural strain and s is the deflection [mm]. Both the force-extension and force/displacement data were recorded through the QMAT 5.46 S-series software.

(a) (b)

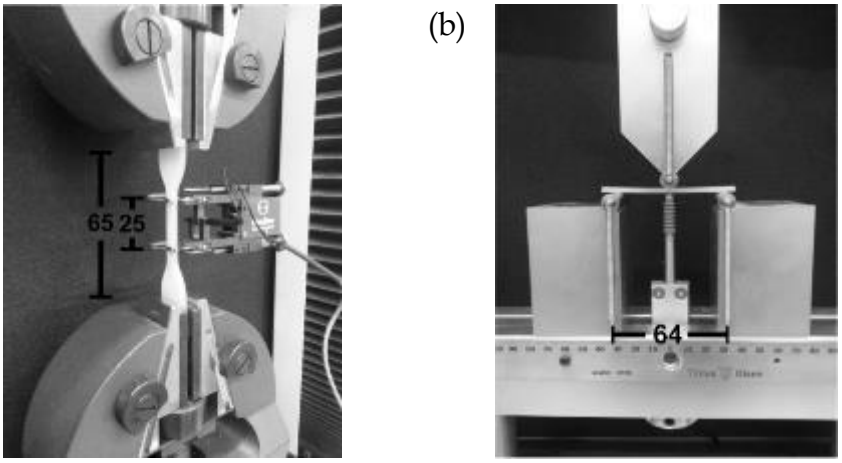

Figure 21: a) Tensile test setup with extensometer attached on the specimen, and b) bending test setup. All noted dimensions are in mm.

3.7.2 Structural characterisation

The fracture surface of the printed specimens was investigated using a Hitachi S-4300 field-emission scanning electron microscope (FESEM). The accelerating voltage used was 5kV. Prior to observation, all specimens were sputter-coated with gold, in order to prevent electrostatic discharge.

3.7.3 Melt flow rate

The melt flow rate test is used in the polymer industry as a simple, inexpensive, and direct method for checking the quality of a material in terms of its flowability (processability). The melt flow tests were performed on GÖTTFERT-MI-3 'Facelift' melt index tester. During this test, the materials were pre-heated at 210^{o}C in a barrel and then extruded under the application of a 2.16 kg load, while the extruded volume was recorded for 10 minutes (melt volume flow rate-MVR). MVR tests were performed by BYK Chemie.

3.7.4 Die swell ratio

Die swell measurements were performed in the RepRapPro 3D printer. The die swell (as described in Section 2.4.2) ratios have been calculated for each filament composition using the following equation:

$$\text{Die swell} = \frac{extrudate\ diameter}{nozzle\ diameter} \quad [5]$$

where the nozzle diameter was taken equal to 0.5 mm. The extrudate diameter corresponds to the mean diameter of the extruded filament through the 3D printer. The extrudate diameter was determined [64] for each filament composition by extruding five strands (20mm long) of each filament through the nozzle of the printer at a speed of 150mm/min. After the extruded material cooled down (for approximately one hour), its diameter was measured by a Vernier calliper at three random points per strand and the mean value was calculated.

3.8 Statistical analysis

Statistical tests, such as one-way analysis of variance (ANOVA) or independent samples t-test can be used to compare the means between two (or more, in the case of ANOVA) independent groups on the same variable and evaluate whether there are any statistically significant differences between them [75,76]. These techniques were employed here in order to assess whether or not the observed variations in the mechanical properties amongst samples were significant. All tests were performed using the IBM SPSS Statistics 21 software.

3.8.1 One-way ANOVA

One-way ANOVA is used to determine whether there are any statistically significant differences between the means of two or more independent groups of one categorical variable. Specifically, it tests the null hypothesis (H_0):

$$H_0: \mu_1 = \mu_2 = \mu_3 = ... = \mu_k \quad [6]$$

where μ is the group mean (i.e. mean value of the dependent variable for a specific group of the independent variable) and k is the number of groups (groups of the independent variable). If the one-way ANOVA returns a statistically significant result, the alternative hypothesis is true, which is that there is at least a pair of groups that exhibit statistically significantly different means [77]. As an omnibus test statistic, it cannot provide information on which specific groups are statistically significantly different from each other [76]. Hence, a post hoc test, e.g. Tukey, is necessary, in order to determine which specific pairs of means are different [77,78].

The test statistic F and its components are usually exported in a table in SPSS, as shown below:

Table 11: Structure of one-way ANOVA results in SPSS.

Source	**SS**	**df**	**MS**	**F**	**Sig.**
Between	SS_b	$df_b = k-1$	MS_b	MS_b/MS_w	*p* value
Within	SS_w	$df_w = N-k$	MS_w		
Total	$SS_b + SS_w$	N-1			

where SS is the sum of squares (SS_b between groups and SS_w within groups), df is the degrees of freedom (df_b between groups and df_w within groups), n is the total number

of observations and k the number of groups, MS is the mean square (MS_b between groups and MS_w within groups) and Sig. is the significance that is illustrated by the obtained p-value that corresponds to the likelihood that the results have occurred by chance. The significance level a (alpha) here was taken as 0.05, hence for $p \leq 0.05$ the H_0 is rejected and there is a statistically significant difference between the means [78]. The general form of reporting the results of a one-way ANOVA is as follows:

F (dfb, dfw) = F-statistic, p = p-value [7]

ANOVA and post-hoc Tukey multiple comparisons [79] were employed in order to investigate whether the infill orientation of 3D printed PLA specimens has a significant effect on the mechanical properties. Five infill orientations were tested and five identical specimens were employed for each infill orientation, as described in Section 3.6.1. An alpha level of 0.05 was used for all statistical tests.

3.8.2 Independent-samples t-test

The independent-samples t-test (or independent t-test) compares the means between two independent groups in order to determine whether there is statistical evidence that the group means are significantly different [75,80]. Following the formality of ANOVA, the general form of reporting the results of an independent-samples t-test is as follows:

t (df) = t-statistic, p = p-value [8]

In the investigation of the effect of filament composition on the mechanical properties, the properties of all composite filaments were compared only to those of the neat PLA filament. Therefore, independent-samples t-test was found to be a more suitable method to employ than ANOVA in this case. The significance level a was taken as 0.05, similar to the ANOVA tests.

Chapter 4: Optimisation of printing parameters

The mechanical properties of 3D printed parts are determined not only by the properties of the feedstock filament itself but also by the printing parameters, which in turn affect the mesostructure of the 3D printed parts [31,42,81]. The investigation of the effect of the employed processing parameters on the mechanical properties is thus essential, and in industry, it could prove crucial when designing components that need to meet specific operating requirements. A preliminary study was conducted utilising neat PLA 2003D, in order to determine the optimal printing parameters, prior to printing the nanocomposite feedstock filaments.

4.1 Effect of infill orientation

To evaluate the effect of infill orientation on the tensile properties, five PLA 2003D dumbbell specimens were printed per infill orientation and tested to failure, as described in Section 3.6.1, Table 7. Figure 22 shows typical tensile stress-strain curves for all infill orientations.

In general, the curves revealed a brittle behaviour for all samples, due to the brittle nature of PLA [61]. Initially, all samples exhibited a linear elastic behaviour. The samples with 0° and 45° infill orientation failed before yielding, whereas the 90° and the 0°/90° exhibited little plastic deformation before failure.

Figure 23 gives the digital images of typical fracture patterns of printed PLA for all infill orientations. A brittle fracture is clearly indicated for all infill orientations,

which is consistent with the stress-strain curves shown in Figure 22. The 0° samples (Figure 23a) displayed a typical fracture and failed in the transverse direction, perpendicular to the PLA beads.

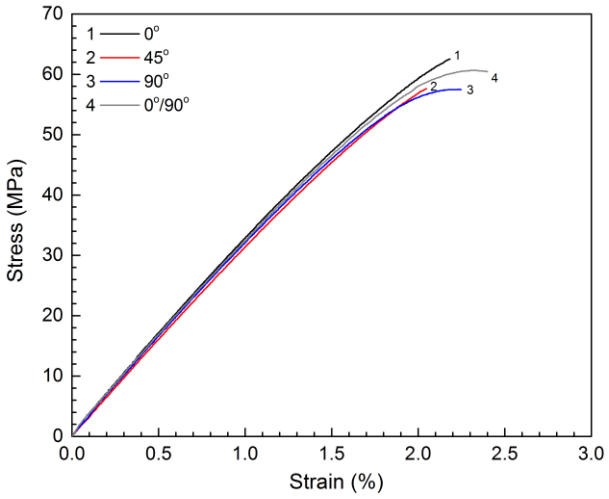

Figure 22: Typical stress-strain curves of 3D printed PLA samples for each infill orientation.

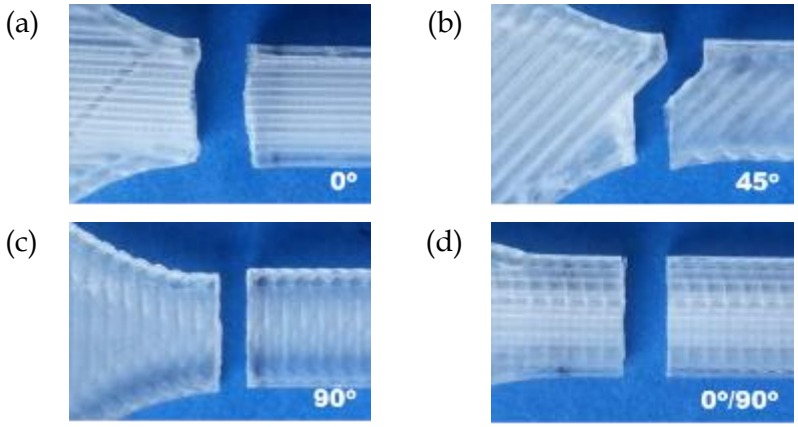

Figure 23: Digital images of 3D printed PLA with the following infill orientations: a) 0°, b) 45°, c) 90°, and d) 0°/90°, showing the through-thickness fracture after tensile test.

The 90° samples (Figure 23c) failed also in the transverse direction, along the weak interface between adjacent PLA beads. The 45° samples (Figure 23b) exhibited a characteristic partially shear failure along the 45° direction, which corresponds to the

direction of the bonding between the PLA beads, whereas the 0°/90° samples (Figure 23d) failed at intersecting paths along the 0°/90° directions. Samples with +45°/-45° infill orientation were also printed and tested. It was found that these samples exhibited similar behaviour to the 0°/90° samples.

In order to investigate the mode of failure and understand the failure mechanism, the fracture surfaces of the samples were inspected at microscopic level. FESEM micrographs from the centre of the fracture surfaces (cross-section) of the printed PLA specimens are presented in Figure 24. The schematics of the geometry of the cross-section for each infill orientation are given in the corresponding insets. All specimens exhibited a relatively smooth surface, due to the predominantly brittle fracture. The FESEM micrographs revealed that the cross-section (perpendicular to the loading direction) of the printed specimens was formed of consecutively stacked layers, where individual printed beads and layers were visible (Figure 24a, Figure 24d). The triangular air voids (Figure 24a, Figure 24d) were due to the layering approach of the 3D printing process.

The 90° (Figure 24c) specimen exhibited failure in the transverse direction along the interfaces between the PLA beads, while the 0°/90° (Figure 24d) specimen failed both along the weak interfaces between the polymer beads and across the beads.

The measured modulus of elasticity, tensile strength, and per cent elongation at break of the printed PLA samples are summarised in Table 12. The measured properties of each infill orientation sample were compared to those of the rest infill orientations samples.

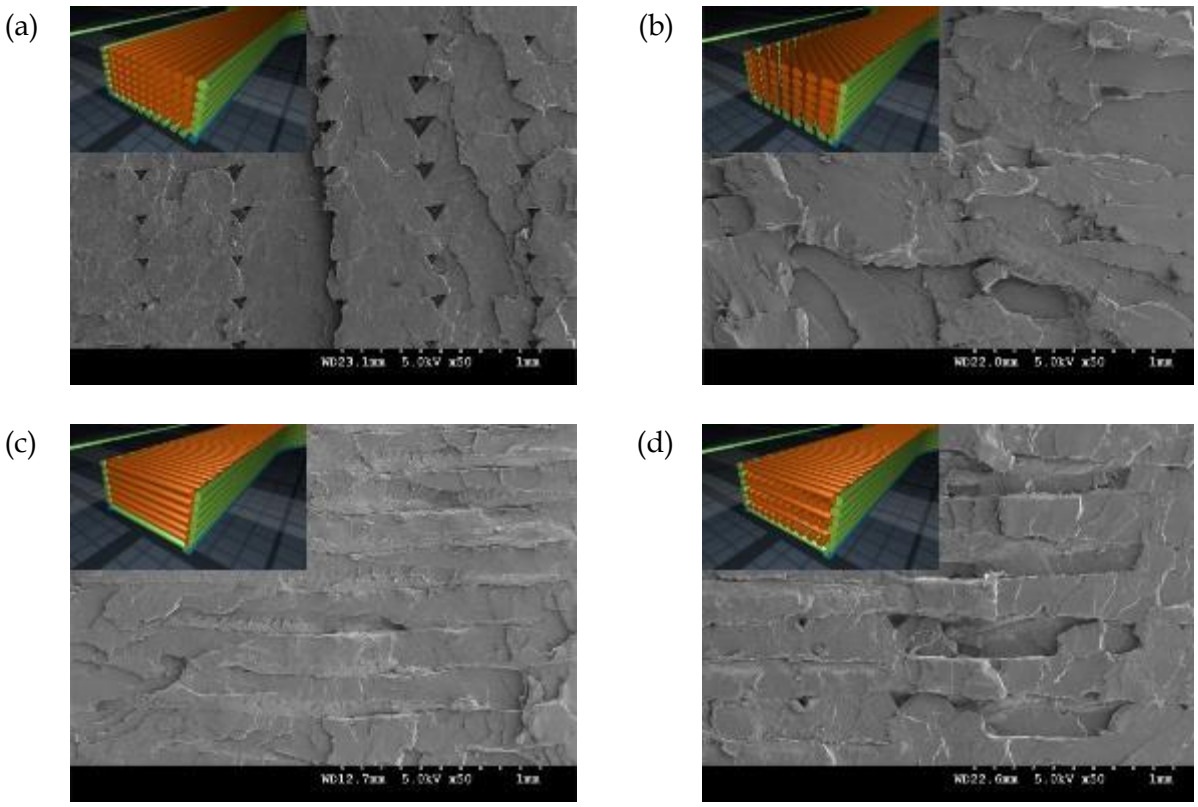

Figure 24: FESEM micrographs of the fracture surface of 3D printed PLA dumbbell specimens with a) 0°, b) 45°, c) 90°, and d) 0°/90° infill orientation. Illustrations of each corresponding cross-section are depicted in the insets.

Table 12: Tensile properties of the printed PLA samples with different infill orientations.

Infill orientation	**Modulus of elasticity (GPa)**	**Tensile strength (MPa)**	**Ductility (%)**
0°	3.22 ± 0.1	59.06 ± 5.18	2.06 ± 0.22
45°	3.21 ± 0.1	55.60 ± 5.80	1.93 ± 0.23
90°	3.2 ± 0.07	56.69 ± 1.52	2.17 ± 0.18
0°/90°	3.31 ± 0.07	60.32 ± 1.50	2.37 ± 0.14

A one-way ANOVA and subsequent post-hoc Tukey comparisons were performed, in order to evaluate the effect of the infill orientation on the mechanical properties of the printed samples. ANOVA results showed that there was no

statistically significant effect of the infill orientation on the modulus of elasticity [calculated F-test statistic of $F(3,16)=15.93$, $p=0.230$]. The 0°/90° sample exhibited 6.4% higher tensile strength than the 90° sample ($p = 0.016$) and 22.3% higher elongation at break than the 45° sample ($p = 0.012$). The rest of the comparisons did not give any statistically significant difference. Overall, it could be concluded that the 0°/90° behaved the best, as its properties exhibited the smallest standard deviations among all samples.

In literature, a significant improvement in the mechanical properties was reported, as the infill orientation shifted from 90° to 0° [31,32,42]. This discrepancy might be attributed to the different air gap between the beads used in these cases. In fact, in a published work on ABS [38], it was observed that the effect of the air gap on the tensile strength was not the same for all infill orientations. For example, the use of zero air gap led to more pronounced differences in the tensile strength between the infill orientations, compared to the use of negative air gap.

In the current study, the air gap was determined automatically by the Slic3r software (beads overlapped), with the user not being able to control it directly. The air gap value was the same for all infill orientations. The employed air gap led to the polymer beads being printed sufficiently close together, thus resulting in good bonding and a solid-like structure, as shown in Figure 24. Overall, it could be concluded that the 0°/90° infill orientation behaved the best, as its properties exhibited the smallest standard deviations among all sample, so 0°/90° was selected as the optimal printing orientation.

4.2 Effect of layer thickness

To evaluate the effect of layer thickness on the tensile properties, five PLA 2003D dumbbell specimens were printed per layer thickness and tested to failure. As explained in Section 3.6.1, Table 8, the specimens were printed with 0°/90° infill orientation and 50% infill density. Tensile tests were performed to failure, without the use of extensometer.

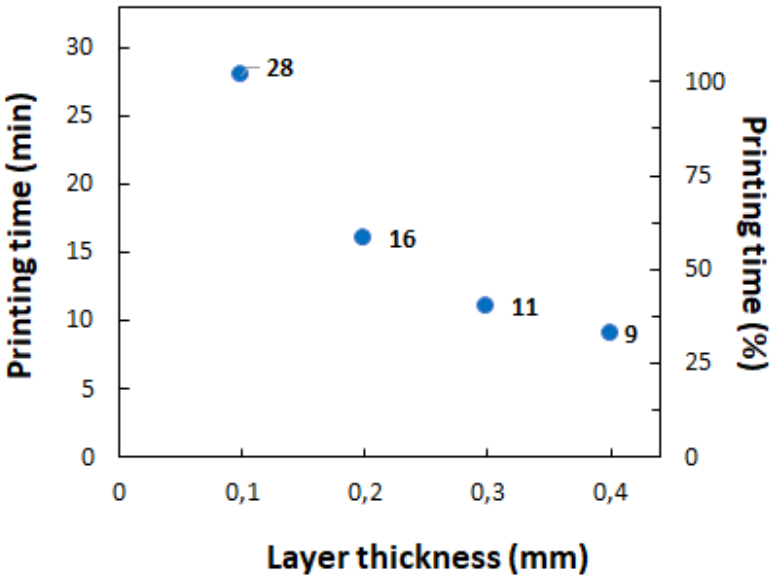

Figure 25: Printing time of 3D printed PLA specimens vs layer thickness.

The impact of layer thickness on the total printing time per specimen is shown in Figure 25. The printing time for 0.4mm layer thickness was approximately 20 minutes shorter than that for 0.1mm layer thickness, as in this case fewer layers are required to reach the same final desired thickness.

The tensile test results are presented in Figure 26. Both the modulus of elasticity (Figure 26a) and the tensile strength (Figure 26b) exhibited similar trend; initially increasing, as the layer thickness increased from 0.1mm to 0.2mm, and then decreasing, as the layer thickness increased from 0.3mm to 0.4mm. Samples with

0.2mm and 0.3mm layer thickness exhibited a similar modulus of elasticity and tensile strength, with no statistically significant difference. Moreover, these samples exhibited lower standard deviation in the modulus of elasticity than the 0.1 and 0.4mm samples, possibly due to their more uniform mesostructure, as shown in Figure 27 and discussed below.

Figure 27 shows FESEM micrographs from the fracture surface of 3D printed PLA specimens of different layer thickness after tensile testing. Two groups of individual polymer beads are visible in all micrographs, which correspond to the 0° (pointing towards the normal on the page) and 90° (on the page plane) infill orientation (0°/90° used here). Due to the 50% infill used in this experiment, there is no overlap between adjacent beads.

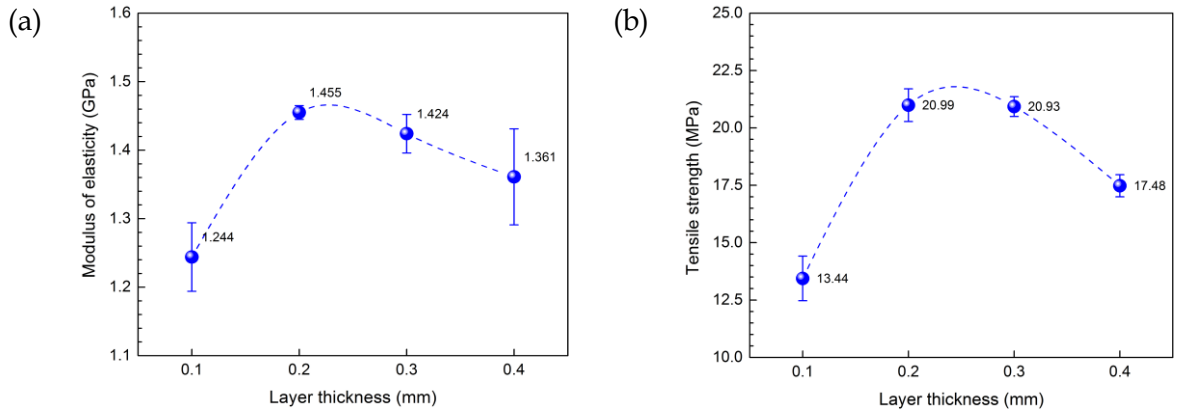

Figure 26: a) Modulus of elasticity, and b) tensile strength of 3D printed PLA specimens vs layer thickness.

The specimen with 0.1mm layer thickness (Figure 27a) exhibited low print quality and uneven bead spacing. The polymer strands the extruder is attempting to merge together are very thin and poorly controlled at low layer thickness, leading to the printing of a structure that cannot support itself [42]. In general, low layer thickness

(0.1mm) increases the numbers of layers that need to be printed, resulting in more flaws and distortions within the printed sample [42].

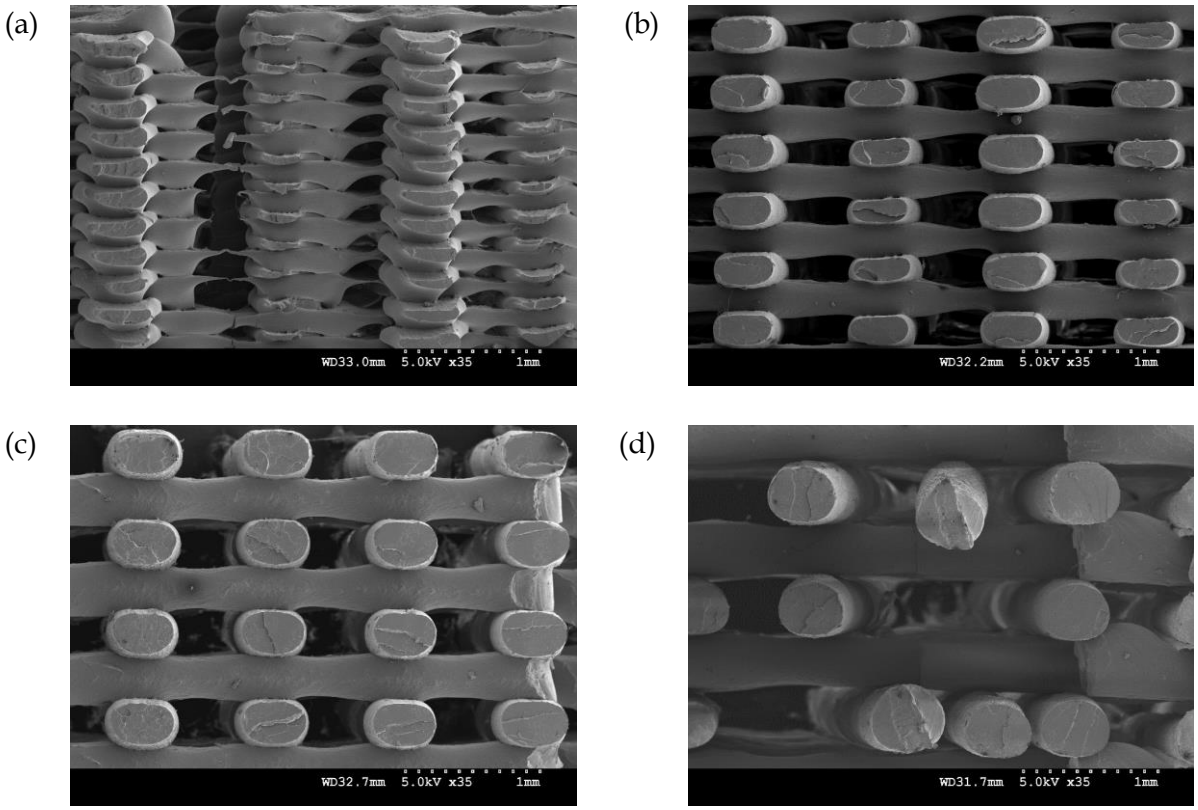

Figure 27: FESEM micrographs of the fracture surface of 3D printed PLA dumbbell specimens with a layer thickness of a) 0.1mm, b) 0.2mm, c) 0.3mm, and d) 0.4mm.

These flaws could be responsible for the weak mechanical properties of the 0.1mm sample. Higher layer thickness (0.2mm and 0.3mm) (Figure 27b and Figure 27c) produces fewer but thicker layers with fewer faults, resulting in strong strands that support higher tensile loads, thus leading to higher stiffness and strength (Figure 26). For 0.4mm layer thickness (Figure 27d), a decrease in the tensile strength was observed (Figure 26b). This effect could be attributed to the larger air voids between the stacked polymer beads, which have an impact on the maximum tensile load that the specimens withstand before failure. Taking into account both the mechanical

properties and the printing time, there is an optimal layer thickness that delivers better properties in shorter printing time; in this case, it was found to be the 0.3mm layer thickness.

4.3 Effect of infill density

To evaluate the effect of infill density on the tensile properties, five PLA 2003D dumbbell specimens were printed per infill density and tested to failure, as described in Section 3.6.1, Table 9. Tensile tests were performed to failure, without the use of extensometer.

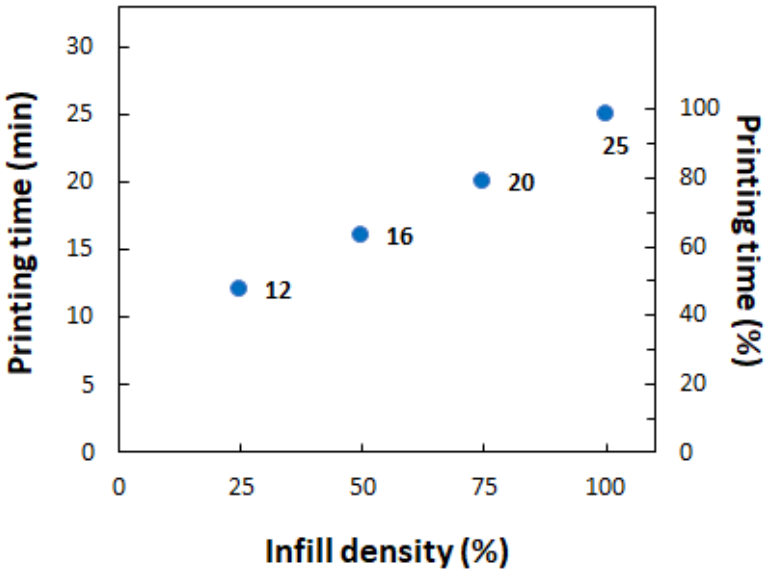

Figure 28: Printing time of 3D printed PLA specimens vs infill density.

As shown in Figure 28, increasing the infill density from 25% to 100% gave rise to the printing time by 14 minutes. However, the higher the infill density, the better the mechanical properties were, as shown in Figure 29. Specimens with low infill density (e.g. 25% or 50%) exhibited both a largely porous structure (as shown in Figure 30a and Figure 30b), which resulted in low modulus (e.g. 0.82 GPa for the sample with

25% infill density) (Figure 29a) and tensile strength (9.5 MPa for the sample with 25% infill density) (Figure 29b).

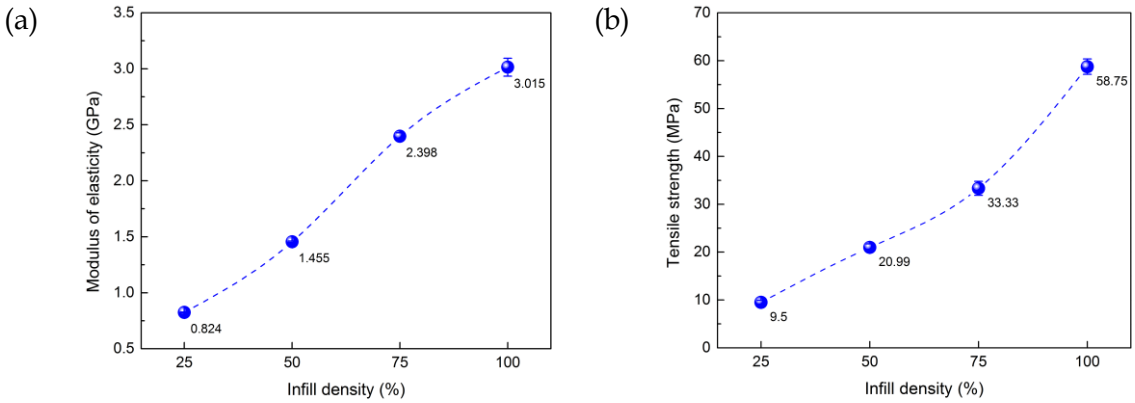

Figure 29: a) Modulus of elasticity, and b) tensile strength of 3D printed PLA specimens vs infill density.

As the infill density increased (Figure 30c,d), the samples exhibited better mechanical performance, which is attributed to the fact that when a component has more material over which to distribute an applied loading, it will be more resistant to failure.

As explained above, increasing infill density means longer printing time and higher material consumption. This has an impact on the ratio modulus of elasticity/printing time per specimen and modulus of elasticity/weight per specimen (Figure 31a), or tensile strength/time and strength/weight (Figure 31b). Figure 31 shows that the 25% and 50% infill densities are the least efficient from both material usage and printing time standpoints, as they exhibited the lowest ratios. The 100% infill density is the most efficient from both material consumption and printing time standpoints, as it exhibited the highest ratios among all densities.

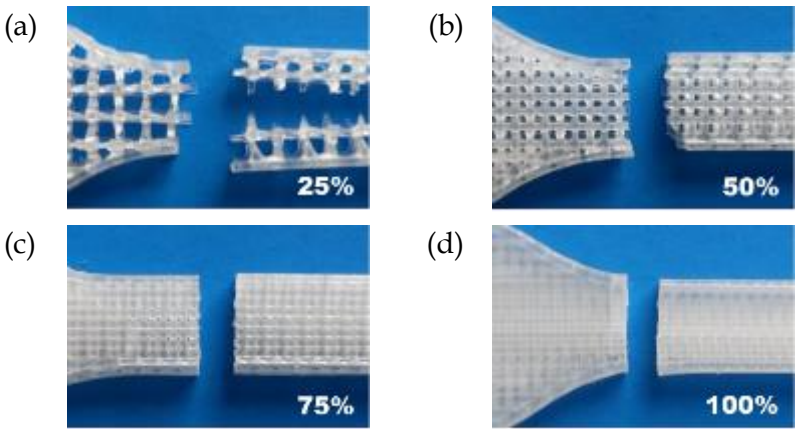

Figure 30: Digital images of 3D printed PLA with the following infill densities: a) 25%, b) 50%, c) 75%, and d) 100%, showing the through-thickness fracture after tensile test.

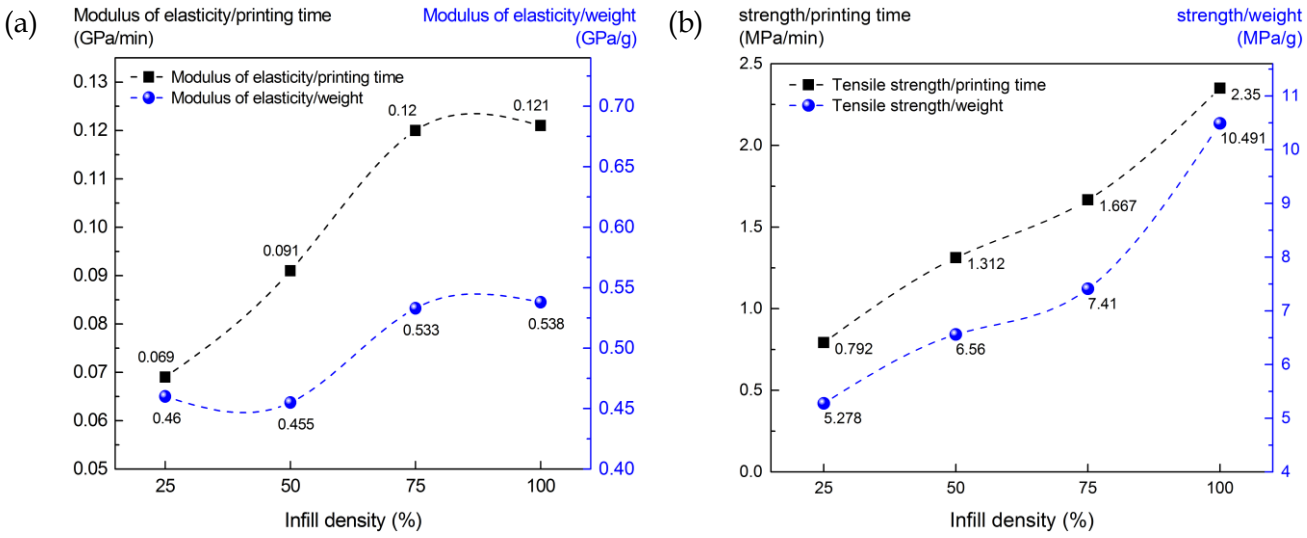

Figure 31: a) Modulus of elasticity/printing time per specimen and modulus of elasticity/weight per specimen vs infill density, and b) tensile strength/printing time and tensile strength/weight vs infill density.

4.4 Summary

The samples with 0°/90° infill orientation behaved the best, as they gave the smallest variability in all properties. The optimal layer thickness was determined as a balance between mechanical performance and printing time and it was found to be 0.3mm.

Higher infill densities exhibited better mechanical properties, but in general, required longer printing times. Summarising, the optimal printing parameters for achieving the best mechanical performance are listed in Table 13.

Table 13: Optimised printing parameters used in the 3D printing of polymer/clay composite filaments.

Printing parameters	**Value**
Infill orientation, angle	0°/90°
Layer thickness, mm	0.3
Infill density, %	100

Figure 32 shows a typical SEM micrograph of the fracture surface of a PLA specimen (after the tensile test) printed with the optimal parameters.

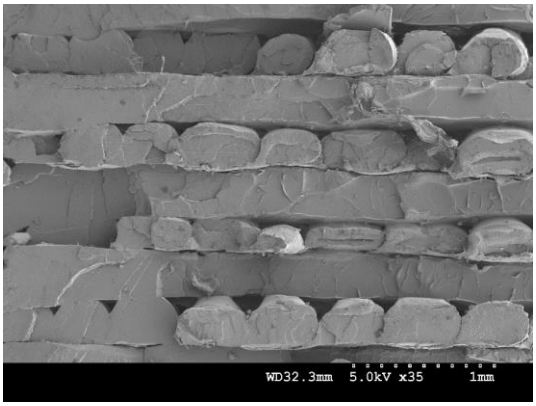

Figure 32: FESEM micrograph of the fracture surface of a neat PLA specimen after the tensile test, printed using the optimal parameters.

Chapter 5: 3D printing of PLA/Cloisite nanocomposites

As explained in Section 2.3, a possible approach for tailoring the properties of printing materials for FFF and expanding the range of their applications is by the addition of clays to the polymer feedstock, in order to obtain polymer/clay composite filaments. This chapter investigates the effect of the filament composition (clay type, content, and effect of the matrix) on the mechanical properties of the printed composite samples and correlates them with the extent of intercalation of different types of clays.

5.1 Selection of PLA Ingeo:clay composite system

A screening experiment was performed initially, in order to assess the performance of PLA composites, based on two different grades of PLA matrix. As mentioned in Section 3.2, the two types of polylactide that were used as the polymer matrix were:

- *PLA Ingeo 2003D* (NatureWorks), which is a high molecular weight and general-purpose extrusion grade polylactide [66], and
- *PLA Ingeo 3251D* (NatureWorks), which is designed for injection moulding applications. This polymer grade has a higher melt flow capability than PLA 2003D [67]. Their typical properties are given in Section 3.2, Table 1.

Clo5 was utilised as the clay filler and its typical properties are listed in Section 3.2, Table 2. Both neat PLA and PLA composite specimens (for tensile testing) were printed by employing the optimal printing parameters, as determined in Section 4.4,

Table 13. Tensile tests were performed following the process described in Section 3.7.1.

Typical stress-strain curves of the printed neat PLA 2003D and PLA 3251D samples, obtained from the tensile tests are presented in Figure 33. Both printed samples exhibited an initial linear elastic deformation. After that, the samples behaved differently. PLA 2003D yielded with increasing load and reached maximum tensile stress prior to fracture, while PLA 3251D fractured before yielding, suggesting PLA 3251D is more brittle than PLA 2003D. The mechanism of this behaviour is not fully understood but it may be related to the molecular weight of the 3251D grade (Table 2 in Section 3.2 shows that PLA 3251D has a higher MFR, than the PLA 2003D, suggesting lower viscosity and possibly lower molecular weight for this grade), which could in turn result to its observed weaker tensile properties (e.g. stiffness, tensile strength, ductility) compared to that of PLA 2003D.

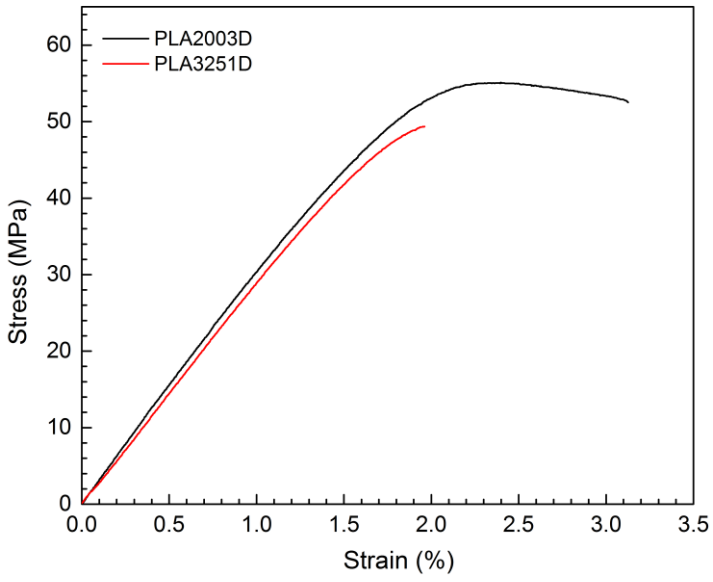

Figure 33: Typical stress-strain curves of 3D printed PLA samples.

Figure 34 gives the digital images showing the typical fracture patterns of both printed PLA 2003D (Figure 34a) and PLA 3251D (Figure 34b). A brittle fracture is clearly indicated with little overall plastic deformation. This fracture character is consistent with the stress-strain behaviour shown in Figure 33.

(a) (b)

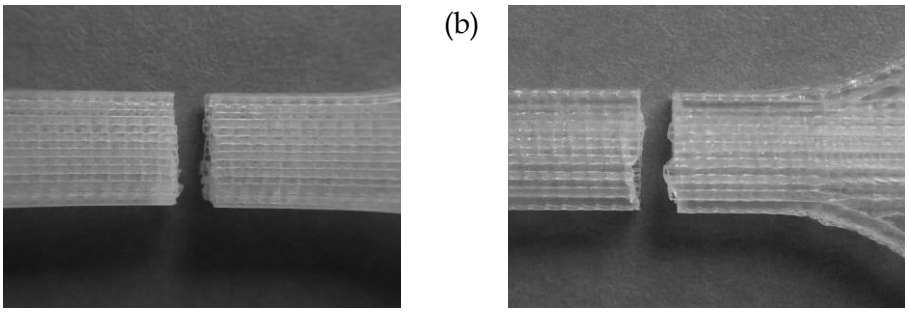

Figure 34: Digital images of 3D printed a) PLA 2003D and b) PLA 3251D specimens, showing the through-thickness fracture after the tensile test.

The measured tensile properties of the printed PLA samples are summarised in Table 14. Both PLA grades were found to exhibit a similar modulus of elasticity (3.27 ± 0.08 GPa for PLA2003D and 3.14 ± 0.24 GPa for PLA3251D, Table 14).

The tensile strength and ductility of PLA 3251D were lower than that of PLA 2003D due to possibly the lower molecular weight of this grade (as mentioned above). As it was observed in Figure 33, PLA 3251D exhibited higher brittleness than the PLA 2003D and failed before yielding, so the tensile strength was in fact not reached. The corresponding composite exhibited even lower ductility, as shown in Table 14, due to the addition of the nanoclay in the polymer matrix. The modulus of elasticity of PLA/clay composites appeared to be overall higher than that of the neat PLA matrices, for both PLA grades. PLA/clay composites exhibited lower tensile strength compared to neat PLA, for both PLA grades. In summary, PLA 2003D-based samples were found to exhibit better mechanical performance than the PLA 3251D samples.

Hence, the rest of the research is focused on studying the PLA 2003D-based composites.

Table 14: Tensile properties of the printed neat PLA and PLA/clay composite samples.

Material	Modulus of elasticity (GPa)	Tensile strength (MPa)	Elongation at break (%)
PLA 2003D	3.27 ± 0.08	55.58 ± 1.2	2.88 ± 0.58
5wt% Clo5	3.6 ± 0.10	47.11 ± 2.38	1.7 ± 0.13
PLA 3251D	3.14 ± 0.24	49.43 ± 3.39	1.89 ± 0.14
5wt% Clo5	3.7 ± 0.25	28.53 ± 2.27	0.85 ± 0.09

5.2 Tensile properties of printed PLA/clay composites

PLA 2003D/Cloisite composite specimens (for tensile testing) were printed by employing the optimal printing parameters, as determined in Section 4.4, Table 13. The typical properties of all Cloisite clays are given in Section 3.2, Table 2. Tensile tests were performed following the process described in Section 3.7.1.

Typical tensile stress-strain curves of the printed neat PLA and PLA/Cloisite composite samples are presented in Figure 35. All printed samples exhibited an initial linear elastic deformation. The neat PLA 2003D and the composite samples containing 1wt% organoclay (Clo5 and Clo20) yielded, while the 1 wt% natural clay (Clo116) sample fractured before yielding (Figure 35a). The 5 wt% organoclay samples (Figure 35b) also exhibited little plastic deformation before fracture. These results show that the clay content and type have a significant effect on the mechanical behaviour of the printed composites.

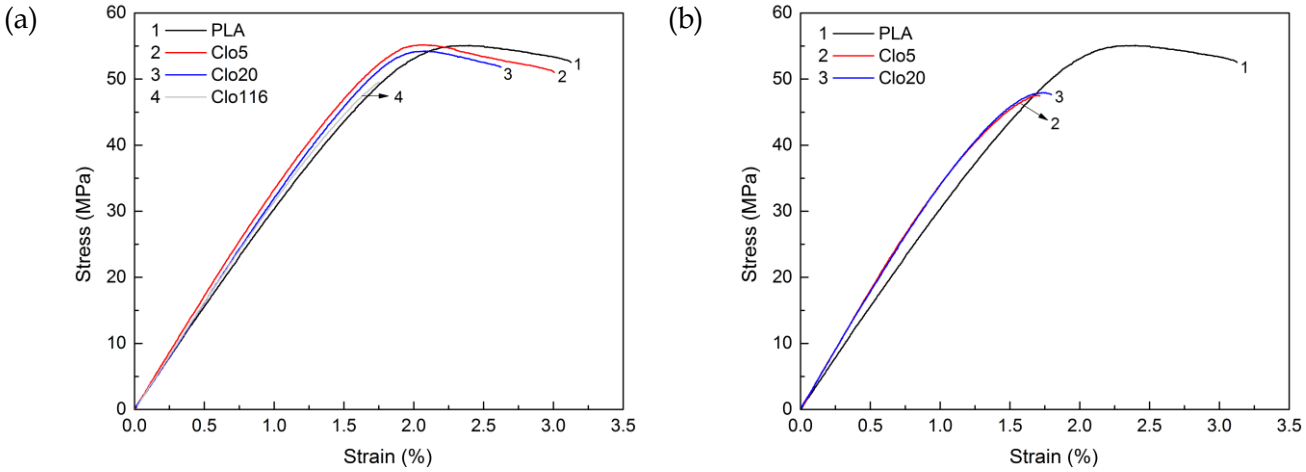

Figure 35: Typical tensile stress-strain curves of 3D printed neat PLA and PLA/clay samples for clay content of a) 1 wt%, and b) 5 wt%.

Figure 36 gives the digital images of typical fracture patterns of both printed neat PLA 2003D (Figure 36a) and PLA/Cloisite composite samples (Figure 36b). A brittle fracture is observed with overall little plastic deformation. This fracture character is consistent with the stress-strain behaviour shown in Figure 35.

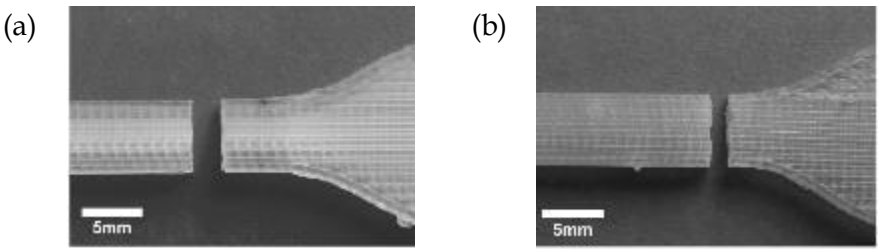

Figure 36: Digital images of 3D printed a) PLA 2003D and b) PLA/clay composite specimens, showing the through-thickness fracture after tensile test.

The modulus of elasticity, tensile strength, and percent elongation at break of the printed composites are summarised in Table 15. The measured properties of the composites were compared to that of the neat PLA and reported as percent relative difference (% R.D.) in Table 15.

Independent-samples t-tests were performed in order to compare the tensile properties between neat PLA and each obtained PLA/clay composite. The average values in Table 15 were calculated from five specimens. The obtained p-values are also listed in Table 15. Each p-value represents the results of the comparison of the properties between neat PLA and the corresponding composition.

Independent-sample t-test results (Table 15) showed that there was a statistically significant effect of the composition of the filament on the tensile strength, the percent elongation at break, and the modulus of elasticity of the printed samples. In detail, there was no statistically significant difference between the tensile strength and percent elongation at break of the composite samples with 1 wt% organoclay (Clo5 and Clo20) and that of neat PLA. However, 1 wt% natural clay (Clo116) and 5 wt% organoclay samples exhibited a statistically significant reduction in both the tensile strength and percent elongation at break (e.g. for Clo5 clay, a reduction of 15.2% and 40.8% respectively) compared to that of neat PLA (Table 15). Therefore, the results in Table 15 indicate that adding 1 wt% of organoclay did not alter neither the tensile strength nor the ductility of the PLA matrix. Increasing the organoclay content to 5 wt% though, resulted in a significant reduction in the ductility and the tensile strength of the composites.

Table 15: Tensile properties of the printed PLA 2003D/Cloisite samples and results of t-tests (p-value)[2].

Material	Modulus of elasticity (GPa)	% R.D.	p-value	Tensile strength (MPa)	% R.D.	p-value	Elongation at break (%)	% R.D.	p-value
PLA 2003D	3.27 ± 0.08	-	-	55.58 ± 1.2	-	-	2.88 ± 0.58	-	-
1wt% Clo5	3.5 ± 0.07	+7.0	0.001	54.42 ± 1.14	-2.1	0.154	2.75 ± 0.63	-4.5	0.743
5wt% Clo5	3.6 ± 0.10	+10.1	0.000	47.11 ± 2.38	-15.2	0.000	1.7 ± 0.13	-40.8	0.009
1wt% Clo20	3.33 ± 0.10	+1.8	0.308	54.13 ± 1.76	-2.6	0.168	2.58 ± 0.12	-10.1	0.323
5wt% Clo20	3.56 ± 0.13	+8.9	0.003	46.12 ± 4.1	-17.1	0.001	1.71 ± 0.31	-40.4	0.004
1wt% Clo116	3.29 ± 0.06	+0.6	0.700	46.74 ± 2.56	-15.9	0.000	1.61 ± 0.17	-43.9	0.006

[2]p-value stands for the comparison between the properties of neat PLA and each PLA/clay composition.

As shown in Table 15, all composite samples exhibited a higher modulus of elasticity compared to that of neat PLA. Independent-sample t-tests confirmed that the observed increase in the modulus of elasticity was statistically significant for the organoclay samples, and was more pronounced at higher clay content (e.g. 7.0% and 10.1% increase in the average modulus for the samples with 1wt% and 5 wt% of Clo5 in PLA respectively). The observed increase in the modulus values for the 1wt% natural clay was not statistically significant. Further investigation was then carried out in order to understand the mechanism behind the mechanical behaviour of the printed samples.

5.3 Flexural properties of printed PLA/clay composites

PLA 2003D/Cloisite composite specimens (for flexural testing) were printed by employing the optimal printing parameters, as determined in Section 4.4, Table 13. Flexural tests were performed following the process described in Section 3.7.1.

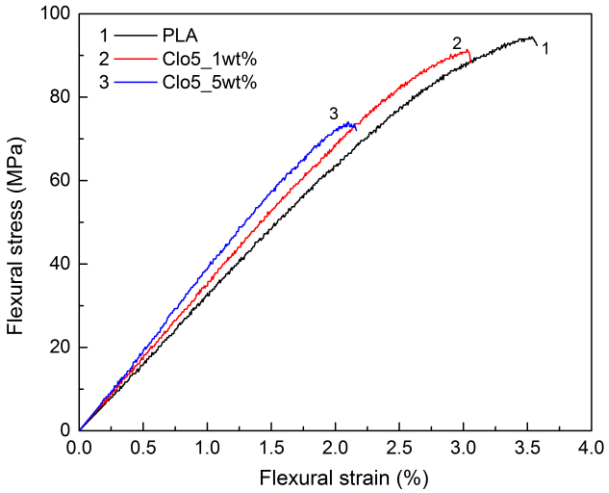

Figure 37: Typical flexural stress-strain curves of 3D printed neat PLA and PLA/clay samples.

Typical flexural stress-deflection curves of PLA/clay samples, obtained by three-point bending tests, are illustrated in Figure 37. Independent-sample t-test results (Table 16) showed that there was a statistically significant effect of the composition of the filament on the flexural strength, the flexural strain at break, and the flexural modulus of the printed samples. The results follow a similar trend to that observed in the tensile tests: significantly increased flexural modulus and reduced strength and ductility for the 5wt% samples, but no significant difference neither in the strength nor the ductility for the 1wt% samples. As shown in Table 16, the flexural modulus exhibited a statistically significant increase of 13.9% only for the 5 wt% Clo5 sample compared to the modulus of neat PLA. Compared with the neat PLA sample, there is a 21.1% reduction in the flexural strength for the 5 wt% clay sample, while no significant difference was observed for the 1wt% Clo5 sample. It is noted that the increase of elastic modulus of 1wt% Clo5 was found to be statistically significant in the case of tensile tests (Table 15, $p=0.001$) but insignificant in the case of flexural tests (Table 16, $p = 0.146$). This could be attributed to the larger standard deviation (±0.19 GPa) of the flexural modulus compared to that of the tensile modulus (±0.06 GPa). Taking into account that flexural tests are surface-sensitive, the inherent surface roughness of the printed specimens could give rise to the high standard deviation of the test results.

Table 16: Flexural properties of the printed samples and results of t-tests (p-value)[3].

Material	Flexural modulus (GPa)	% R.D.	p-value	Flexural strength (MPa)	% R.D.	p-value	Flexural strain at break (%)	% R.D.	p-value
PLA 2003D	3.17 ± 0.17	-	-	89.98 ± 8.56	-	-	3.54 ± 0.37	-	-
1wt% Clo5	3.36 ± 0.19	+6.0	0.146	84.54 ± 9.52	-6.0	0.370	3.02 ± 0.44	-14.7	0.079
5wt% Clo5	3.61 ± 0.15	+13.9	0.004	70.96 ± 4.21	-21.1	0.002	2.3 ± 0.2	-35.0	0.000

[3]p-value stands for the comparison between the properties of neat PLA and each PLA/clay composition.

5.4 Structure

5.4.1 Mesostructure of PLA/Cloisite composites

FESEM micrographs from the fracture surface (cross-section) of printed neat PLA and composite specimens after tensile testing are presented in Figure 38. All specimens were printed employing the optimal printing parameters, as described in Section 4.4. All specimens exhibited a relatively smooth surface, due to the brittle fracture. This brittle character is again consistent with the low ductility of the printed samples observed in Figure 35. The FESEM micrographs revealed that the cross-section of the printed specimens is formed of consecutively stacked layers, where individual printed beads and layers were visible. It is clear that the printed specimens were inherently porous. The triangular air voids present in all specimens were due to the layering approach of the 3D printing process.

The printed polymer beads are mostly visible in PLA (Figure 38f) and Clo5 (Figure 38a and b) specimens, whereas Clo20 (Figure 38c,d) or Clo116 (Figure 38e) composite specimens appear to be less porous, with the adjacent layers having fused together more than in other samples. In order to evaluate whether the difference in the overlap of the printed beads affects the mechanical properties of the printed parts, the porosity of the printed specimens was measured and compared among all clay types.

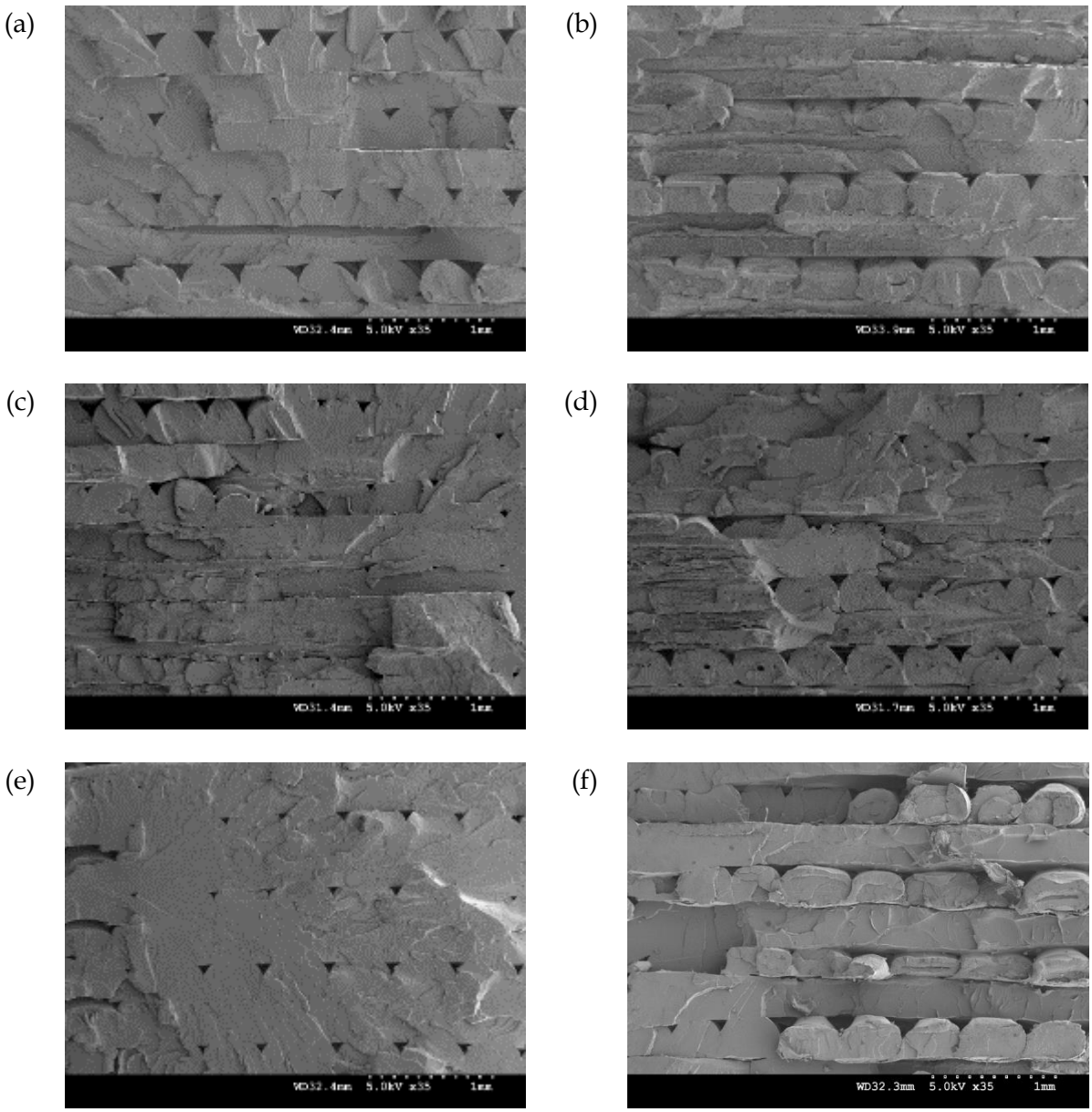

Figure 38: FESEM micrographs of the fracture surface of 3D printed dumbbell specimens of a) PLA/1wt% Clo5, b) PLA/5wt% Clo5, c) PLA/1wt% Clo20, d) PLA/5wt% Clo20, e) PLA/1wt% Clo116 composite specimens, and f) neat PLA.

The porosity P of the printed specimens was determined [52] from Eq.9:

$$P = \frac{V_t - V_a}{V_t} \% \qquad [9]$$

where V_t is the volume of the printed parts and V_a the actual volume of the solid (PLA+clay). Regularly shaped pieces were cut off from the gauge area of the printed dumbbell specimens and V_t was calculated based on the dimensions of each cut piece. The mass (m) of each cut piece was measured utilising a precision balance (Mettler AJ 150), and Va was then derived employing Eq.10:

$$V_a = \frac{m*\text{clay content wt\%}}{\rho_{clay}} + \frac{m*\text{PLA content wt\%}}{\rho_{PLA}} \quad [10]$$

where ρ_{clay} and ρ_{PLA} are the densities of the clay and the PLA respectively (Section 3.2, Table 2). The reported porosity for each sample represents the average porosity from five specimens.

The overall porosity of the printed PLA/clay specimens determined using Eq. 9 is presented in Figure 39. It can be seen that the lowest measured average porosity is recorded for the composite sample with 1wt% natural clay (Clo116). The 5wt% organoclay samples appeared to have the highest average porosity values. All tested clay samples showed higher standard deviation values than that of neat PLA samples. Taking into account the standard deviations, it could be considered that all samples containing Clo5 and Clo20 clay exhibited similar porosity to that of neat PLA. Pores are generally expected to have a negative impact on the load bearing behaviour of materials. However, it is noted that Clo116 sample exhibited the lowest performance in terms of tensile behaviour (Figure 35, Table 15) of all composite samples, whereas its measured porosity was the lowest among all clays. This suggests that the overall porosity of the printed samples did not seem to be the major reason accounting for the observed differences in the mechanical properties among the 3D printed PLA/clay composites.

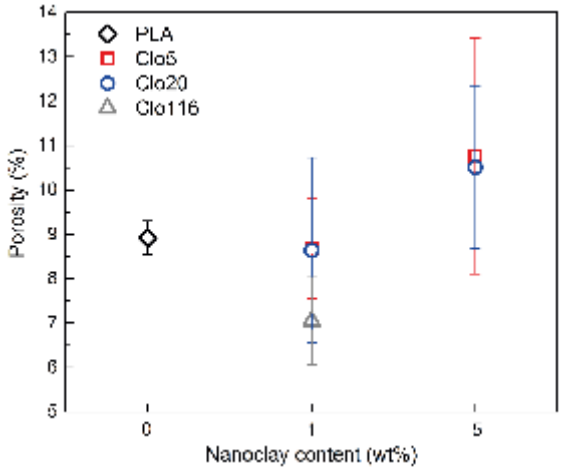

Figure 39: Porosity of the 3D printed PLA/clay composites and neat PLA samples.

5.4.2 Micro- and nanostructure of PLA/Cloisite composites

In their powder form, the raw clays (organomodified or natural) consist of large aggregates of stacked aluminosilicate platelets, as shown in Figure 40a, which gives a FESEM micrograph of typical organomodified clay powder, before dispersion in the PLA matrix. Upon the application of high shear forces during the melt processing of the PLA/clay systems (in the fabrication of the feedstock filaments), the aggregated clay platelets were delaminated (Section 2.3.1, Figure 11) into smaller stacks of platelets as shown in Figure 40b. The quality of the clay dispersion depended on the clay type and the shear forces.

Figure 40b is a typical TEM micrograph of 5 wt% organoclay in the PLA matrix presenting the main constituents of the structure. It shows a heterogeneous clay distribution, consisting of a mixture of clay agglomerates, coexisting with intercalated clay stacks, and exfoliated platelets. The large dark features in Figure 40b are clay agglomerates and the regions in between them show a uniform dispersion of exfoliated nanosized platelets. These appear in the micrograph as thin dark linear features of approximately 100 nm in length and 30 nm in thickness. Therefore, the

dispersion of platelets may be considered as providing a nanostructure within the polymer matrix.

(a) (b)

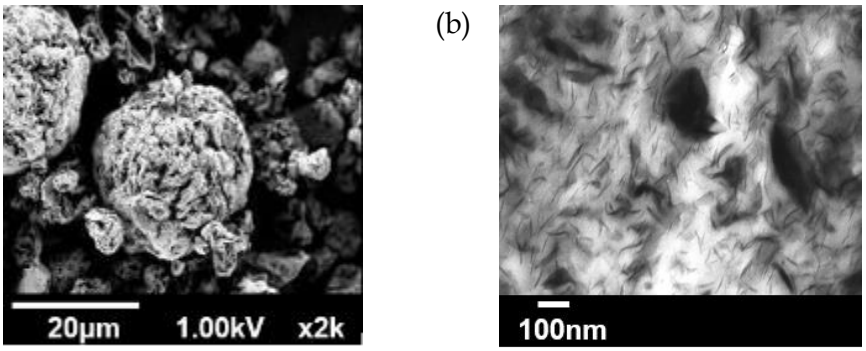

Figure 40: a) Typical SEM micrograph of organomodified Cloisite powder, and b) typical TEM micrograph showing the dispersion of clay platelets in the polymer matrix.

Many of the exfoliated platelets appear to be in contact with one another, forming a network, possibly with interactive bonding with the polymer matrix. Providing the stacks of the platelets are thin enough, uniformly dispersed, well bonded to the matrix and sufficiently close together, substantial reinforcement of the polymer matrix is enabled through a load-transfer mechanism and molecular interaction [52]. The interaction will involve intercalation of the polymer into the clay and may be quantified by the average number of platelets per clay stack: the greater the intercalation, the smaller the number of platelets per stack. It is pointed out that the reinforcement is related to the extent of intercalation and/or exfoliation of the clays in the polymer matrix [52], hence the effect of intercalation on the mechanical behaviour of the composites is investigated in the following section.

5.5 Modelling the elastic modulus of PLA/Cloisite composites

Halpin-Tsai's [82] model was applied to calculate the modulus of elasticity of the PLA/Cloisite composites. PLA/Cloisite composites were considered as two-component systems [Cloisite clay platelets as the dispersed phase (filler) and PLA as the matrix]. The properties of each component were considered the same as those of the raw materials, before blending (Section 3.2, Table 2). Only the density of the high modulus clay platelets is considered in the determination of the volume fraction of the clay phase (Table 17). In this case, the density of the natural clay Clo116 (2.8 g/cm^3) is used in the calculations. In addition, both clays and matrix were considered to be linearly elastic, isotropic and well bonded to each other before yield.

Table 17: Composition of the PLA/clay filaments investigated.

Clay type	**Clay content in PLA**			
	wt%	**vol%**	**wt%**	**vol%**
Clo5	1	0.45	5	2.3
Clo20	1	0.45	5	2.3
Clo116	1	0.45	-	-

The Halpin-Tsai model incorporates both the geometry and elastic modulus of the filler as well as its content and has been used to predict the stiffness of polymer composites with fibre or disk-like fillers, including polymer/nanoclay composites [14,18]. The normalised elastic modulus can be written in the form:

$$\frac{E_C}{E_m} = \frac{1 + \zeta\eta V_f}{1 - \eta V_f} \quad [11]$$

where E_c and E_m are the moduli of elasticity of the composite and the matrix respectively, and V_f is the volume fraction of the filler. In this equation, ζ is an adjustable shape parameter that depends on the geometry of the filler and η is given by:

$$\eta = \frac{\frac{E_f}{E_m} - 1}{\frac{E_f}{E_m} + \zeta} \quad [12]$$

where E_f is the modulus of elasticity of the filler.

This model is applied to the current composites under study in which the controlling filler is taken to be the organically modified and natural clay platelets. Figure 40b shows that the clay platelets are randomly oriented and distributed within the PLA matrix. The applied shear forces on the polymer melt, during printing, are not sufficient to align the clay platelets along the printing direction. However, in the analysis used here, all the clay platelets were assumed to be oriented along the loading direction and consequently, a longitudinal modulus was determined. The predicted results will therefore only represent the upper limit of the elastic modulus of the composite and the experimentally measured moduli should be below this limit. The platelet stacks are assumed to be disc-like and for a longitudinal modulus, the shape parameter ζ can be taken to be [26]:

$$\zeta = 2l/t \quad [13]$$

where l and t are the length and thickness of the platelet respectively. Equations [11] to [13] link the stiffness of the composite to the aspect ratio of the platelets. This enables a quantified relationship with the fineness of the dispersion and extent of

intercalation/exfoliation to be determined. The gradual exfoliation of a platelet stack reduces its thickness (t) and hence gives a larger aspect ratio (l/t). The average length (l) of the clay platelets was estimated using TEM observations to be 100 nm, while the average thickness of the clay stacks (t_{clay}) was calculated using the following equation:

$$t_{clay} = (n\text{-}1)\, d_{001} + t_{platelet} \quad [14]$$

where n is the number of platelets per clay stack, d_{001} is the d-spacing within the clay stack and $t_{platelet}$ is the thickness of a single clay platelet taken equal to 0.94nm [14,18]. The d-spacing values (d_{001}) of the as-received clays were used in the calculations and the corresponding values for all three clays are listed in Section 3.2, Table 2.

Only the high modulus clay platelets were considered as a reinforcing phase in the current PLA/clay system. The effective modulus of the clay platelets was taken as the modulus of the filler E_f and determined by the rule of mixtures:

$$E_f = E_{MMT} V_{clay} + E_{gallery} V_{gallery} \quad [15]$$

where E_{MMT} is the modulus of the pure clay (montmorillonite) platelets taken as having a magnitude of 178 GPa [18,83,84], $E_{gallery}$ is the modulus of the organic modifiers within the galleries of the clay platelets for which $E_{gallery} << E_{MMT}$ in the case of organoclay, and $E_{gallery} = 0$ for natural clay. V_{clay} and $V_{gallery}$ are the volume fractions of the clay platelets and the galleries respectively. Hence:

$$E_f = E_{MMT} \times \frac{n t_{platelet}}{t_{clay}} = 178 \times \frac{0.94n}{(n-1)d_{001} + t_{platelet}} = 178 \times \frac{0.94n}{(n-1)d_{001} + 0.94} \quad [16]$$

5.6 Effect of clay intercalation on the mechanical performance of PLA/Cloisite composites

As obtained from the Halpin-Tsai model, the calculated normalised (longitudinal) modulus of elasticity of the composites E_c/E_m is plotted against the clay content in Figure 41a and Figure 41b.

In general, the calculated ratio E_c/E_m of the PLA/clay composites increased linearly with clay content. However, the efficiency of the reinforcement (as reflected by the gradient of the calculated trend lines) reduced significantly with increasing number of platelets per clay stack (reduced extent of clay intercalation). For example, in Figure 41a, the gradient of the n=2 predicted line (high extent of intercalation/exfoliation) was approximately 5 times greater than the gradient of the n=13 line, suggesting that the extent of clay intercalation greatly affected the performance of the composites.

The measured modulus values are also shown in Figure 41 in order to compare the effect of the clay dispersion. It is noted that the measured E_c/E_m value for 1 wt% Clo5 organoclay (Figure 41a) was close to the predicted trend line of n=2, while the E_c/E_m value for the 5 wt% sample was close to the line of n=13. This indicates that the 1wt% Clo5 clay sample exhibited on average a higher extent of clay intercalation than that of the 5 wt% Clo5 sample. As it has been reported [16], there is usually an optimal loading level of clays in the polymer matrix, for which the clay dispersion is uniform. For higher loading levels, agglomeration of clays can take place. As a result, the 5 wt% clay sample would have exhibited a much higher elastic modulus if the same intercalation (n=2) had been achieved: an E_c/E_m value of 1.36 instead of the measured value on Figure 41a of only 1.10. The experimental results for both 1 wt% Clo20 and 5 wt% Clo20 (Figure 41a) samples lie on the calculated trend line of n=16, implying

that the Clo20 samples have a lower average extent of clay intercalation than that of the Clo5 samples (which is explained below, in terms of the d-spacing and gallery volume). This is consistent with the inferior mechanical performance of Clo20 relative to that of Clo5. The results indicate that increasing the extent of intercalation is much more efficient than increasing the clay content.

The measured ratio E_c/E_m for the Clo116 natural clay sample (Figure 41b) was consistent with a calculated line of n=80, which corresponds to an aspect ratio of unity and indicates no significant intercalation. This is to be expected as the Clo116 natural clay contained no organic modifier and so behaved like a conventional filler. The latter could not sufficiently improve the stiffness of the composite at the current 1 wt% content. The low experimentally measured values of Clo116 are due to the lack of both interaction and subsequent exfoliation in this clay. In particular, Clo116 has a much larger number of platelets per stack (n=80) compared with Clo5 and Clo20, which only have n values between 2 and 16.

Figure 41 and Table 15 show that the nanoclays (Clo5 and Clo20) provide higher reinforcement than the natural Clo116 clay. It is noted that Clo5 has the largest d-spacing (Section 3.2, Table 2) and hence gallery volume, which is expected to promote the intercalation of the clay platelets, their dispersibility and exfoliation in the PLA matrix [52,85]. As a result, PLA/Clo5 shows the highest mechanical properties amongst all of the composites, as given in Table 15.

Further improvement of the modulus of elasticity with the natural clay may be achieved through higher clay content (Figure 41). However, as shown in Figure 35a, the 1 wt% Clo116 sample fractured before the matrix yielded, possibly due to insufficient adhesion between the clay and PLA matrix, resulting in reduced ductility

and fracture strength. In practice, the process of incorporating 5 wt% Clo116 in PLA to achieve a uniform clay distribution was found to be difficult.

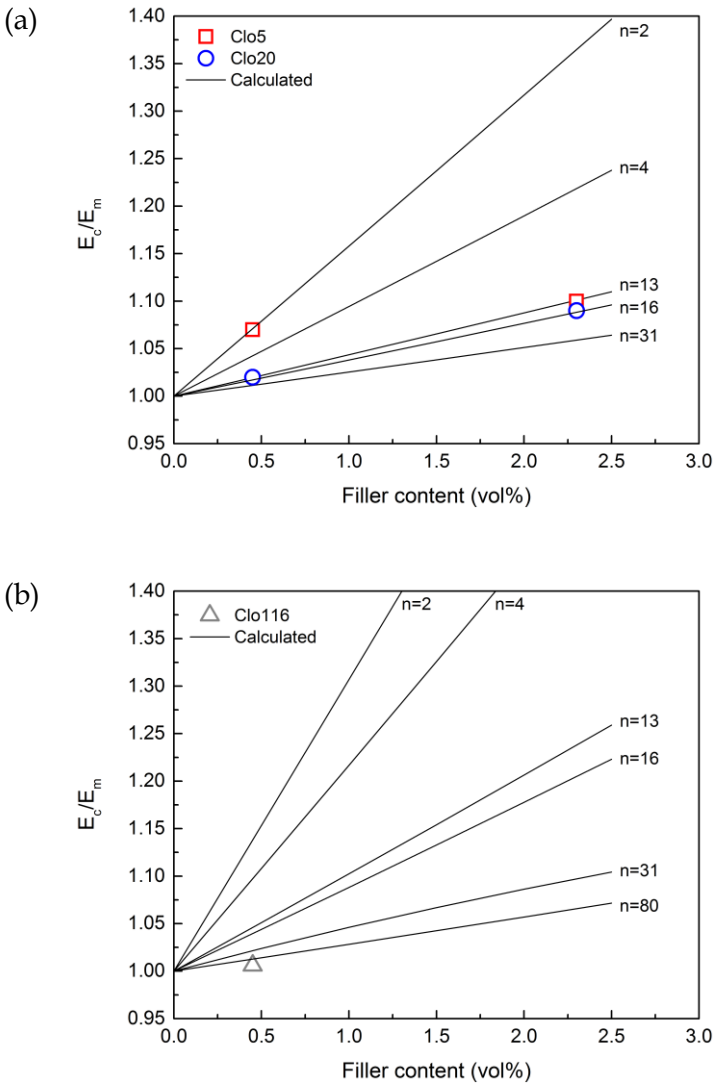

Figure 41: Normalised modulus of elasticity (Ec/Em) for the PLA/clay composites, as determined from both experimental measurements and theoretical calculations based on the Halpin-Tsai model for a) Clo5 and Clo20 and b) Clo116 composite samples.

Although the Halpin-Tsai model applies mainly to elastic behaviour, it can provide useful insights into tensile strength. Specifically, the Halpin-Tsai model indicated that less intercalation took place in the printed 5 wt% organoclay and the 1 wt% Clo 116

(natural clay) samples. This reduction in intercalation will affect the underlying structure of the composite by increasing the amount of non-exfoliated agglomerates and decreasing the clay-matrix interfacial contact and adhesion. These effects are expected to lead to the observed fall in tensile strength and ductility (Table 15). It is pointed out that the observed evolution of tensile strength of the PLA/clay composites with increased clay content is similar to that observed in compression-moulded PLA/clay composites reported in the literature [15,17]. These findings were published in the Elsevier journal Composites Part B [86].

5.7 Summary

PLA and PLA/clay nanocomposites were successfully printed by an open-source 3D printer based on fused filament fabrication. PLA 2003D grade and its composites were found to exhibit better mechanical performance than the PLA 3251D. The porosity of the printed PLA/Cloisite composite samples was not significantly different from that of neat PLA samples. However, the mechanical behaviour of the printed composite samples was influenced significantly by the clay content. The tensile moduli of the printed nanocomposites were increased by 7% for the 1 wt% and 10.1% for the 5 wt% organoclay (Clo5) samples, while the tensile strength and ductility were reduced by 15.2% and 40.8% respectively for the 5 wt% organoclay content and remain unchanged for the 1 wt% samples. The clay type also affected significantly the mechanical behaviour of the printed composite samples. For the same clay content, the samples containing organomodified clay exhibited both better modulus of elasticity and strength than the samples with natural clay, while the organoclay with the highest d-spacing value (Clo5) gave the best performance. The

natural clay had the lowest mechanical performance mainly due to an absence of intercalation. The experimental results were found to be consistent with those predicted by the Halpin-Tsai model, which enables the prediction of their mechanical behaviour. An implication from the research is that clay intercalation is more effective as a reinforcement technique than raising the total clay content.

Chapter 6: 3D printing of PLA/Garamite nanocomposites

As the results of Chapter 5 indicate, clay dispersion is the key for sufficient reinforcement of the mechanical properties of the PLA/Cloisite composites. The PLA/organoclay printed composites exhibited an improvement of the elastic modulus compared to neat PLA, but reduced ductility, followed by no improvement of the tensile strength, due to the limited intercalation of the Cloisite clays in the polymer matrix.

In order to improve the tensile strength of the polymer/clay composites, Garamite (GA) clay was utilised. As described in Section 3.2, GA is an organomodified clay with a mixed clay morphology, consisting of both clay platelets and rods [72]. Its main constituents are the sepiolite and smectite structures. In its powder form, the raw Garamite consists of aggregated organomodified smectite platelets along with organomodified sepiolite rods. Figure 42 gives a typical FESEM micrograph of GA powder before dispersion in the PLA matrix.

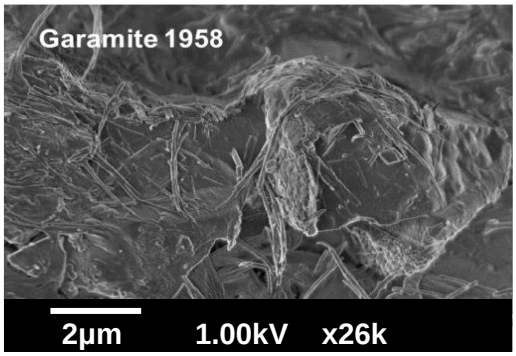

Figure 42: Typical SEM micrograph of organomodified clay powder of Garamite 1958.

The randomly-oriented fibrous structures are due to the sepiolite phase present in GA [87]. The presence of clay rods leads to the formation of a loosely packed clay structure, which is expected to enable the ease of dispersion of GA in the polymer matrix and promote the mechanical reinforcement of the respective composites.

6.1 Mechanical properties

PLA/Garamite composite specimens were printed by employing the optimal printing parameters, as determined in Section 4.4, Table 13. Tensile tests were performed following the process described in Section 3.7.1. Figure 43 shows typical stress-strain curves of neat PLA 2003D and PLA/GA printed composite samples.

(a)

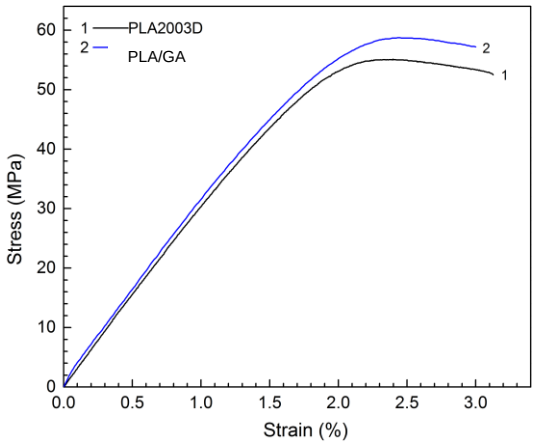

(b)

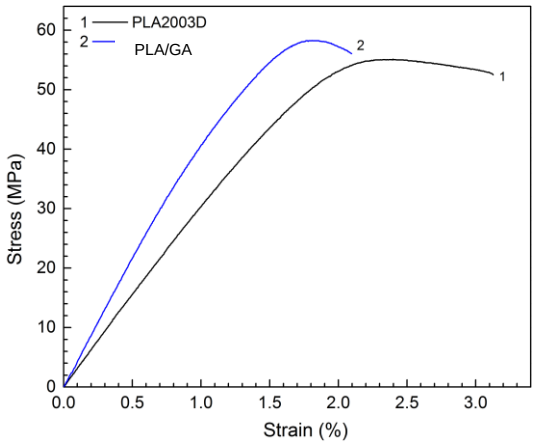

Figure 43: Typical tensile stress-strain curves of 3D printed neat PLA and PLA/GA samples for clay content of a) 1 wt%, and b) 5 wt%.

As shown in Figure 43a, PLA and 1wt% GA exhibited an initial linear elastic deformation, followed by yielding and failure. A different tensile behaviour was observed for the sample with 5wt% clay content (Figure 43b). In detail, the 5wt% GA sample exhibited a more brittle character than the 1wt% clay sample and neat PLA. Overall, the stress-strain curves in Figure 43 show that the printed PLA/Garamite composite samples exhibited an improved modulus of elasticity, yield and tensile strength compared to neat PLA.

The measured modulus of elasticity, tensile strength, and per cent elongation at break of the printed composites are summarised in Table 18. Independent-samples t-tests were performed using SPSS Statistics software, in order to compare the tensile properties between neat PLA and each obtained PLA/clay composite. The obtained p-values and R.D% are listed in Table 18. Each p-value represents the results of the comparison of the properties between neat PLA and the corresponding composition.

At 1wt% clay content, the modulus of PLA/GA was similar to that of PLA. At 5wt% clay content, a 30% increase in the modulus was observed. The tensile strength of PLA/1wt% GA was 5.2% higher than the neat PLA. At 5wt% clay content, PLA/GA exhibited no significant difference in the strength from neat PLA. The ductility of 1wt% clay composite was not significantly different than that of neat PLA, but the ductility of the PLA/5wt% GA sample decreased by 27.1%. Compared to the PLA/Cloisite printed samples, PLA/Garamite composites exhibited a reduction only in the ductility, at 5wt% clay content, as shown in Table 18.

Table 18: Tensile properties of the printed PLA 2003D Garamite samples and results of t-tests (p-value).

Material	modulus of elasticity (GPa)	% R.D.	p-value	Tensile strength (MPa)	% R.D.	p-value	elongation at break (%)	% R.D.	p-value
PLA 2003D	3.27 ± 0.08	-	-	55.58 ± 1.2	-	-	2.88 ± 0.58	-	-
1wt% GA	3.36 ± 0.17	+2.8	0.326	58.48 ± 1.44	+5.2	0.009	2.7 ± 0.45	-6.3	0.608
5wt% GA	4.25 ± 0.17	+30.0	0.000	57.47 ± 2.23	+3.4	0.135	2.1 ± 0.29	-27.1	0.028

Therefore, the results in Table 18 indicate that adding 1 wt% of GA did not alter the ductility of the PLA matrix, but led to an increase in the tensile strength. Increasing the clay content to 5 wt% though, resulted in a significant reduction in the ductility and an increase in the modulus of elasticity. The tensile strength at the same content was maintained for the composite sample.

Taking into account the results for the Clo5 composite samples (Section 5.2, Table 15), at 1wt% clay content, Clo5 was more efficient in improving the elastic modulus, whereas GA was more efficient in improving the tensile strength (compared to neat PLA). At 5wt% clay content, GA was more efficient in improving the overall mechanical performance of the composite than Clo5, as it raised the modulus while maintaining the tensile strength (and inducing limited brittleness). This behaviour could be related to the better dispersion of GA in the polymer matrix (due to its loosely packed clay structure as explained in the introduction of Chapter 6).

6.2 Structure and rheology

FESEM micrographs from the fracture surface of printed PLA/GA composite specimens after tensile testing are shown in Figure 44. PLA/5 wt% GA specimen exhibited a relatively smoother fracture surface than the 1wt% clay specimen, due to its brittle behaviour observed in Table 18. In addition, PLA/5wt% GA sample seems to consist of fewer layers than the ones observed for the 1wt% sample. The printing parameters were the same for both samples. Therefore, this observed difference could be due to the better fusion between the adjacent printed layers in PLA/5wt% GA during the printing process, which allowed for better bonding between consecutive layers.

(a) 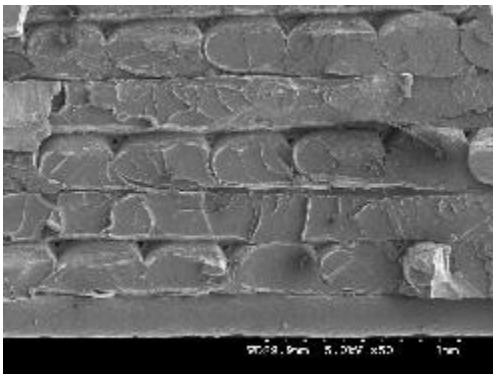 (b) 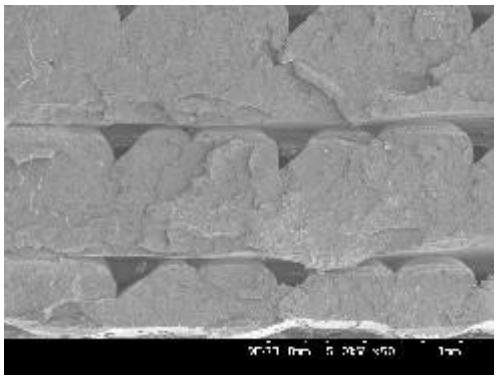

Figure 44: FESEM micrographs of the fracture surface of 3D printed dumbbell specimens of a) 1wt% and b) 5wt% GA in PLA 2003D.

The melt volume flow rates (MVRs) and die swell ratios for neat PLA and PLA/clay composites are listed in Table 19. The MVR of both composite samples was higher than that of neat PLA, suggesting that adding GA clay results to the reduction of the melt viscosity of the PLA/clay composite significantly, possibly due to the thixotropic nature of GA, as described in Section 2.4. In addition, the MVR was found to increase by increasing the clay content (e.g. from 13 cm^3/10min for the PLA/1 wt% GA to 31 cm^3/10 min for PLA/5 wt% GA). This observed increase in the melt flow rate of the PLA/clay composite samples could lead to better bonding between the polymer beads in the 5wt% clay sample (Figure 44b). In general, the bond formation (overlap) between the adjacent polymer beads is known as neck formation and is a phenomenon driven by the surface tension, rheology and heat transfer between the polymer beads and the surrounding atmosphere [14,22]. It is expected that a higher clay content will increase the thermal conductivity of the melt, promoting thus the neck formation between the beads and leading to a greater overlap between them. In order to estimate the neck formation and the overlap between the printed polymer beads, further investigation (future work) is necessary, including sintering

experiments (for measuring the surface tension of the feedstock materials) and thermal conductivity measurements.

Table 19: MVRs and die swell ratios of neat PLA 2003D and PLA/clay composite samples.

Material	**Melt volume flow rate (cm^3/10 min) @ 210°C, 2.16kg**	**Die swell**
PLA 2003D	6	1.32
1wt% GA	13	1.16
5wt% GA	31	0.96

Furthermore, the above increase in the melt flow rate was followed by a decrease in the die swell ratio of the composite samples. For example, the extrudate swell of PLA/1 wt% GA was 1.16, whereas PLA/5 wt% GA exhibited a die swell of 0.96, which was the lowest observed die swell value across all samples. The observed reduced die swell could be due to the greater deformation resistance of the composites samples, in the presence of the fillers. [58]. In fact, the observed reduced die swell suggests that the addition of the GA particles increased the stiffness of the extrudate/filament and hence reduced the deformation within the die and the latter resulted in less elastic recovery. Both composite samples exhibited lower die swell than that of neat PLA.

Die swell is highly sensitive to the measuring technique, and any attempt made here to directly correlate the MVR with the die swell is only rough. The MVR was measured using a die with specific length and diameter, at a pressure of 2.16 kg and temperature of 210°C, whereas the die swell was measured on a different system (i.e. the printer), through a nozzle of a diameter of 0.5mm and total length (tube + die) of 1cm and at 200°C (printing temperature).

The experimental data indicate that upon the introduction of GA at 1wt% in the polymer matrix, the flowability of the melt is improved. Increasing the clay content from 1wt% to 5wt% further improves the flowability. The improved flowability, the low die swell, and the enhanced mechanical performance of the composite samples compared to the neat PLA mean that these composite feedstock filaments are easier to print and provide better resolution than neat PLA (as smaller die swell means smaller extrudate diameter), without compromising the mechanical properties as shown in chapters 5 and 6. These features could prove of utmost importance to the existing filament market and be exploited further, for example for the printing of parts with improved surface finish.

6.3 Summary

At 5wt% clay content, GA was more efficient in improving the overall mechanical performance of the composite than Clo5, as it raised the modulus while maintaining the tensile strength (and inducing limited brittleness). PLA/5wt% GA sample exhibited better bonding between consecutive layers compared to the PLA/1wt% GA sample, resulting in a more compact structure. Upon the introduction of clays at 1wt% in the polymer matrix, the flowability of the melt was improved. Increasing the clay content from 1wt% to 5wt% further improved the flowability. This increase in the melt flow rate was followed by a decrease in the die swell ratio of the composite samples. The improved flowability, the low die swell, and the enhanced mechanical performance of the composite samples compared to neat PLA mean that these composite feedstock filaments are easier to print and can provide better print resolution than neat PLA.

Chapter 7: 3D printing of MAH-g-PLA/PLA/clay composites

Chapters 5 and 6 investigated the effect of the clay fillers on the mechanical properties of the printed composites. In this chapter, the effect of grafted PLA on the properties of PLA/clay composites is investigated. As explained in Section 2.3.1, a coupling agent/compatibiliser can be added to the system of polymer and clays (through grafting it onto a polymer), which will act as a wetting agent between the nanofillers and the polymer [58], promoting their dispersion in the polymer matrix and improving the mechanical properties of the nanocomposites [20,59]. The coupling agent used here was maleic acid anhydride (MAH), which was grafted onto PLA (MAH-g-PLA, grade: TPPL 1112, BYK Chemie) at a low grafting percentage.

7.1 MAH-g-PLA/Clo5 system

The grafted PLA (i.e. MAH-g-PLA) was added into the PLA/Clo5 composite system through the compounding (Section 3.3). The employed MAH-g-PLA/PLA/Clo5 composite feedstock filaments are listed in Section 3.3, Table 3. The composite specimens were printed by employing the same optimal printing parameters, as determined in Section 4.4, Table 13. Tensile tests were performed following the process described in Section 3.7.1.

Figure 45 shows typical stress-strain curves of neat PLA 2003D, MAH-g-PLA(10wt%)/PLA/Clo5(5wt%) and PLA/Clo5(5wt%) composites. As shown in Figure 45, PLA/Clo5(5wt%) exhibited a higher modulus of elasticity but lower tensile

strength and ductility compared to neat PLA. Upon the addition of MAH-g-PLA in the PLA/Clo5 composite, both the modulus of elasticity and the tensile strength increased (Figure 45, Table 20), whereas the ductility remained unchanged. This observed increase could be attributed to the improved interfacial interaction/adhesion and wetting between PLA and Clo5 platelets.

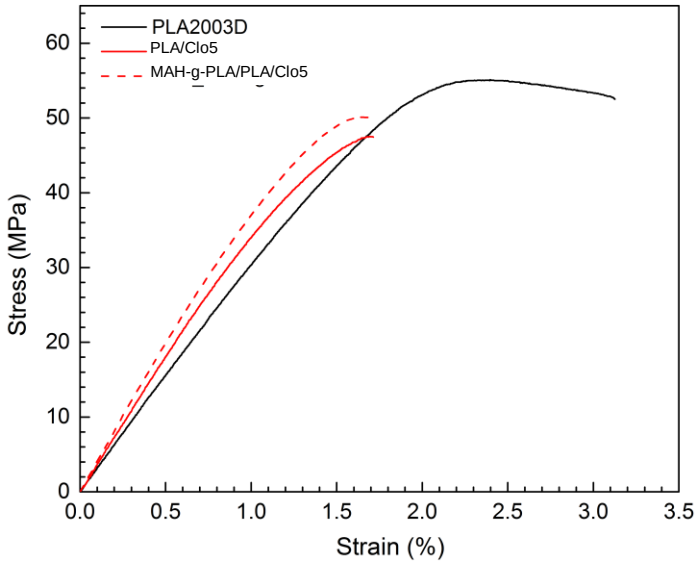

Figure 45: Typical stress-strain curves for neat PLA2003D, PLA/ Clo5 (5wt%) and MAH-g-PLA (10wt%)/PLA/Clo5 (5wt%) composites.

The possible mechanism behind this observed behaviour is shown in Figure 46. When MAH-g-PLA (obtained when MAH is chemically anchored to the PLA chains) is added in the PLA/clay system, the MAH moieties will interact with the clay surface, as shown in Figure 46, whereas the non-grafted PLA is expected to go through this formed network by entanglement. As a result, a hybrid network is expected to form between the clay and the polymer, with the MAH-g-PLA acting as a bridge between the PLA and the clay fillers [59]. This could further lead to efficient stress transfer between the matrix and the fillers (in the exfoliated state) and thus

explain the observed increased tensile strength [59] of the MAH-g-PLA(10wt%)/PLA/Clo5(5wt%) compared to the PLA/Clo5(5wt%) sample.

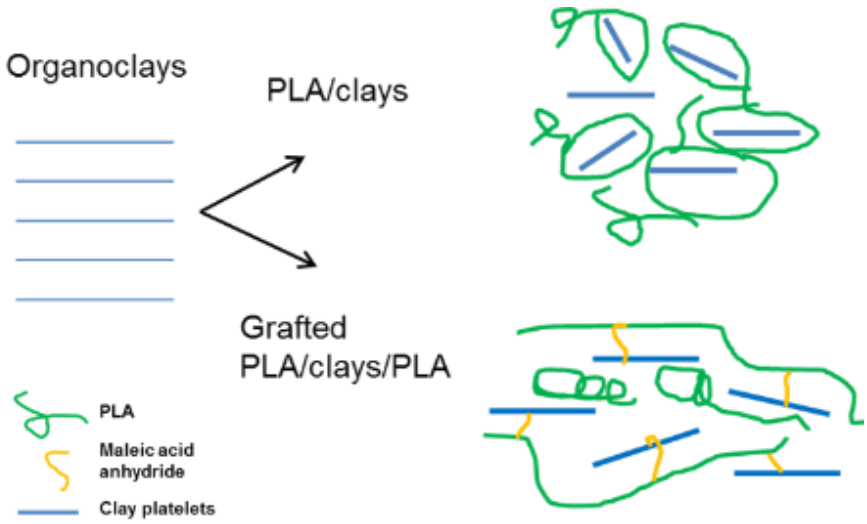

Figure 46: Schematics of possible reaction mechanism for PLA, MAH-g-PLA and Cloisite clay.

Table 20: Tensile properties of the printed neat PLA and MAH-g-PLA/PLA/clay composites and results of t-tests.

Material	modulus of elasticity (GPa)	% R.D.	p-value	Tensile strength (MPa)	% R.D.	p-value	elongation at break (%)	% R.D.	p-value
PLA 2003D	3.27 ± 0.08	-	-	55.58 ± 1.2	-	-	2.88 ± 0.58	-	-
5wt% Clo5	3.6 ± 0.10	+10.1	0.000	47.11 ± 2.38	-15.2	0.000	1.7 ± 0.13	-40.8	0.009
MAH-g-PLA/5wt% Clo5	4.06 ± 0.32	+24.2	0.001	49.08 ± 2.05	-11.7	0.001	1.77 ± 0.26	-38.5	0.005
5wt% GA	4.25 ± 0.17	+30.0	0.000	57.47 ± 2.23	+3.4	0.135	2.1 ± 0.29	-27.1	0.028
MAH-g-PLA/5wt% GA	4.15 ± 0.11	+26.9	0.000	56.43 ± 1.48	+1.5	0.351	1.74 ± 0.78	-39.6	0.003

FESEM micrographs from the fracture surface of printed MAH-g-PLA(10wt%)/PLA/Clo5(5wt%) and PLA/Clo5(5wt%) composite specimens after tensile testing are shown in Figure 47. The sample with the MAH-g-PLA (Figure 47b) exhibited a more compact structure and better merging between the adjacent polymer beads. This could be explained through the neck formation between the adjacent printed polymer beads (practically how much the beads overlap), as Francis et al. [22] and Bellehumeur et al. [88] described in their work.

(a) (b)

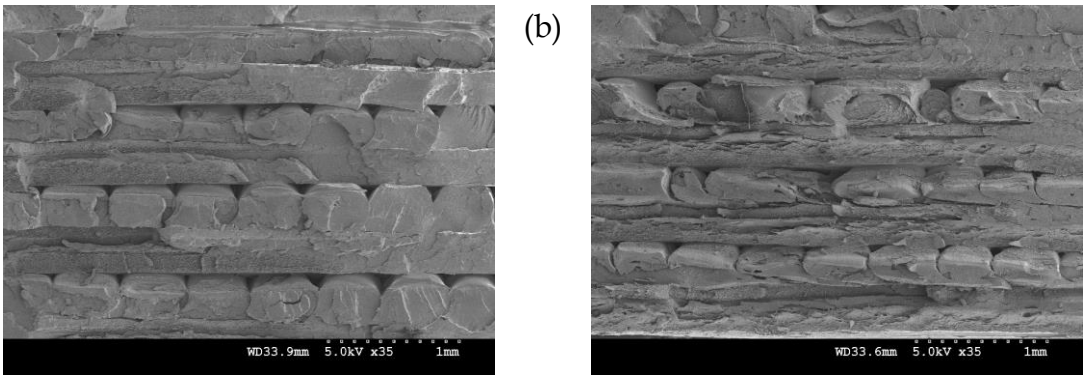

Figure 47: FESEM micrographs of the fracture surface of 3D printed dumbbell specimens of Clo5-based nanocomposites: a) PLA/Clo5(5wt%) and b) MAH-g-PLA(10wt%)/PLA/Clo5(5wt%).

7.2 MAH-g-PLA/GA system

The grafted PLA (i.e. MAH-g-PLA) was added into the PLA/GA composite system through the compounding (Section 3.3). The employed MAH-g-PLA/PLA/GA composite feedstock filaments are listed in Section 3.3, Table 3. The composite specimens were printed by employing the same optimal printing parameters, as determined in Section 4.4, Table 13. Tensile tests were performed following the process described in Section 3.7.1.

Figure 48 shows typical stress-strain curves of neat PLA 2003D, MAH-g-PLA(10wt%)/PLA/GA(5wt%) and PLA/GA(5wt%) composites. The modulus, tensile strength and ductility of the MAH-g-PLA(10wt%)/PLA/GA(5wt%) (Figure 48, Table 20, Figure 49-material 6) were similar to those of PLA/GA(5wt%) (Figure 48, Table 20, Figure 49-material 2).

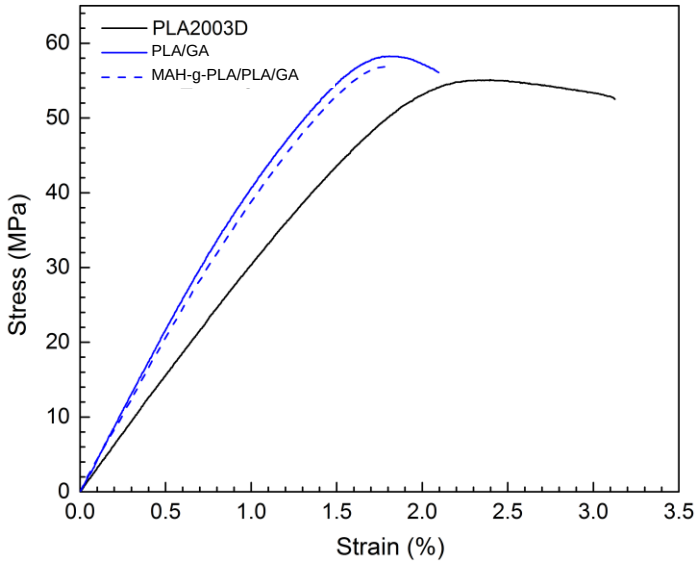

Figure 48: Typical stress-strain curves for neat PLA2003D, PLA/ GA (5wt%) and MAH-g-PLA (10wt%)/PLA/GA (5wt%) composites.

In Section 7.1, it was mentioned that the MAH-g-PLA could act as a bridge between the PLA and the clay fillers [59], promoting the entanglement of the PLA 2003D matrix and resulting in mechanical reinforcement. Following this concept, the wt% of MAH-g-PLA (TPPL 1112) in the composite feedstock material was varied and the mechanical properties of the obtained printed composites were investigated.

The employed MAH-g-PLA/PLA/GA composite feedstock filaments are listed in Section 3.3, Table 3. The clay content in each case remained constant at 5wt%, whereas the wt% of the MAH-g-PLA in the composite varied, from 2.5wt% to 10wt%.

The composite specimens were printed by employing the same optimal printing parameters, as determined in Section 4.4, Table 13. Tensile tests were performed following the process described in Section 3.7.1. Figures 49a,b,c show the tensile properties of neat PLA 2003D, PLA/GA (5wt%) and the MAH-g-PLA/PLA/GA composites with varying content of MAH-g-PLA. Each number on the x-axis of the graphs corresponds to a different filament composition, as shown in the legend of Figure 49a. Material 1 stands for neat PLA (reference sample). Material 2 represents the PLA/ GA (5wt%), without any grafted PLA. Overall, the mechanical properties of the printed samples remain almost the same, as the content of MAH-g-PLA changes.

Therefore, the addition of MAH-g-PLA in the PLA/GA composite system did not seem to have the same influence on the tensile properties as the addition of MAH-g-PLA in the PLA/Clo5 system. This could be due to the easier dispersion of GA in the polymer matrix. In fact, the initial PLA/GA composite exhibited better mechanical performance than the PLA/Clo5 composite at 5wt% clay content (Section 6.1, Table 20). This could mean that MAH-g-PLA does not promote any further interaction between the clay platelets and the PLA matrix, in the case of the GA composite system.

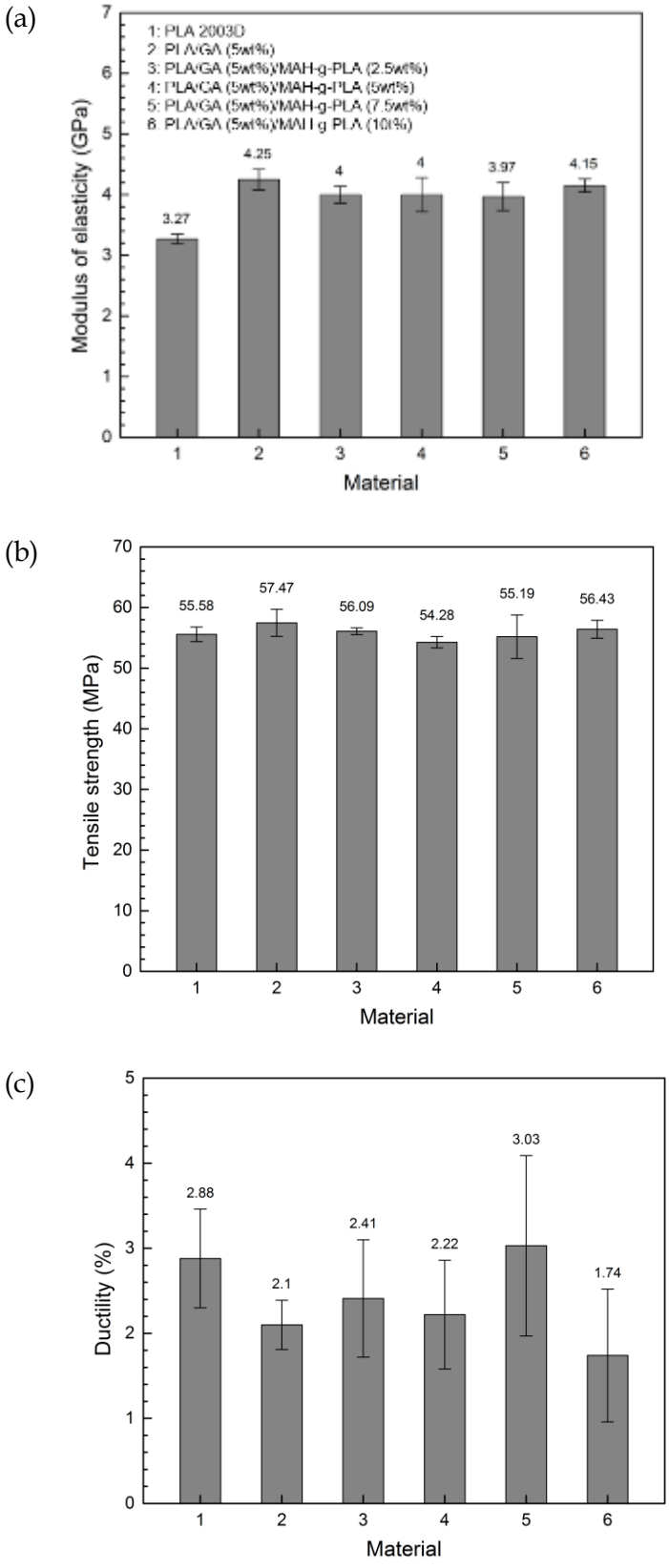

Figure 49: a) Modulus of elasticity, b) tensile strength, and c) ductility of the printed neat PLA and MAH-g-PLA/PLA/GA(5wt%) composites.

FESEM micrographs from the fracture surface of composite MAH-g-PLA/PLA/GA samples with varying content of MAH-g-PLA are presented below. All samples exhibited a smooth fracture surface, with inherent pores present. It is noted here that the sample 5wt% MAH-g-PLA (Figure 50c) in the composite exhibited a more uniform structure, with good inter- and intralayer merging (no significant air voids observed), whereas the rest of the samples exhibited large pores. However, this sample did not give the best mechanical performance as indicated in Figure 49. As explained in Section 7.1, further investigation (future work) is necessary in order to justify the bond between the polymer beads with regards to the surface tension and thermal conductivity of each feedstock material composition.

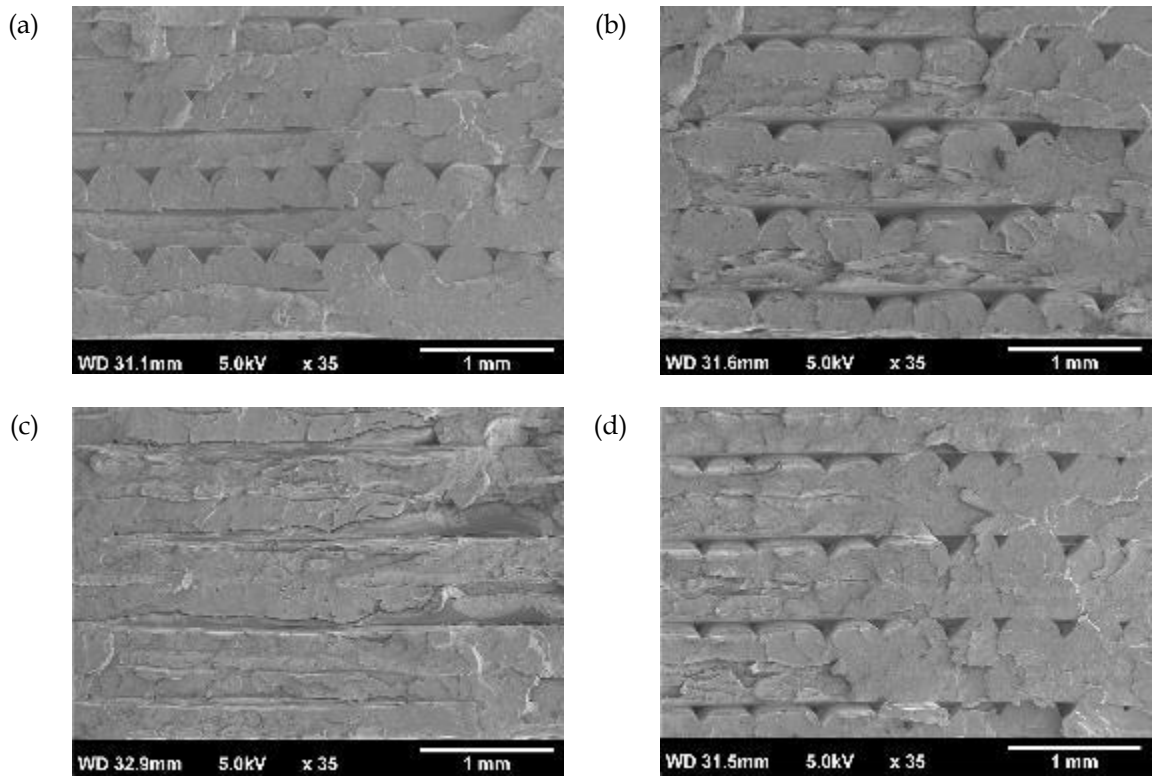

Figure 50: FESEM micrographs of the fracture surface of 3D printed dumbbell specimens of PLA 2003D based nanocomposites at 5wt% GA content, and the following content of MAH-g-PLA: a) 10wt%, b)7.5wt%, c) 5wt% and d)2.5wt%.

7.3 Summary

Upon the addition of MAH-g-PLA in the PLA/5wt% Clo5 composite, both the modulus of elasticity and the tensile strength increased (whereas the ductility remained unchanged), due to possibly the efficient stress transfer between the matrix and the fillers (in the exfoliated state) caused by the presence of MAH-g-PLA as a bridge between the fillers and the matrix. A different behaviour was observed when MAH-g-PLA was introduced into the PLA/GA system, with the tensile properties of PLA/GA being similar to that of the MAH-g-PLA/PLA/GA composite. MAH-g-PLA/PLA/GA exhibited overall better mechanical performance (higher strength and modulus) than MAH-g-PLA/PLA/Clo5 at the 5wt% clay content. In addition, the mechanical properties of the printed samples remained the same, as the content of MAH-g-PLA in the composites changed. This could be due to the easier dispersion of GA in the polymer matrix being the dominant mechanical performance mechanism in this PLA/clay system.

Chapter 8: Conclusion

8.1 Conclusions

- A series of PLA/clay composites were successfully developed and printed by an open-source 3D printer based on fused filament fabrication.
- The optimisation of printing parameters showed that the infill orientation (for 100% infill density) did not have a statistically significant effect on the mechanical properties of the printed samples. Increasing the layer thickness from 0.1mm to 0.2mm or 0.3mm improved the mechanical properties. Increasing it further though, had a negative impact on the tensile properties. The optimal layer thickness was determined as a balance between mechanical performance and printing time. Infill density of 100% was proven to be the most efficient, as shown by the highest ratios of strength (and modulus)/weight and strength (and modulus)/printing time.
- PLA matrix affected the mechanical properties of PLA/clay composites, as PLA 2003D-based composite samples were found to exhibit better mechanical performance than the PLA 3251D samples.
- The mechanical behaviour of the printed PLA/Cloisite composite samples was influenced significantly by the clay content. For example, the tensile moduli of the printed nanocomposites were increased by 7% for the 1 wt% and 10.1% for the 5 wt% organoclay (Clo5) samples, while the tensile strength and ductility were reduced by 15.2% and 40.8% respectively for the 5 wt% organoclay content and remain unchanged for the 1 wt% samples. The tensile modulus of the printed

PLA/GA composites at 5wt% clay content was increased by 30% and its ductility reduced by 27% compared to neat PLA, whereas its tensile strength remained unchanged.

- The clay type also affected significantly the mechanical behaviour of the printed PLA/Cloisite composite samples. For the same clay content, the samples containing organoclay exhibited both better modulus of elasticity and strength than the samples with natural clay, while the organoclay with the highest d-spacing value (Clo5) gave the best performance. The natural clay had the lowest mechanical performance mainly due to an absence of intercalation.
- The Halpin-Tsai model was used to predict the elastic moduli of the printed PLA/Cloisite composite samples. The model relates the moduli of the composites with the extent of intercalation and the clay content. The experimental results were found to be consistent with those predicted by the Halpin-Tsai model, which indicated that the lower performance of 5wt% organoclay and 1 wt% natural clay printed samples was due to less intercalation taking place compared to the 1wt% organoclay samples. An implication from the model is that clay intercalation is more effective as a reinforcement technique than raising the total clay content.
- The morphology of the clay particles affected the mechanical reinforcement of the printed clay composites. For example, at 5wt% clay content, GA was more efficient in improving the overall mechanical performance of the composite than Clo5, as it raised the modulus while maintaining the tensile strength of neat PLA. This effect is possibly due to the efficient stress transfer between the matrix and the GA fillers (in the exfoliated state) caused by the better dispersion of GA compared to that of Clo5.

- Upon the introduction of GA in the polymer matrix, the flowability of the melt was improved. This increase in the melt flow rate was followed by a decrease in the die swell ratio of the composite samples, compared to neat PLA, which means that these composite feedstock filaments could provide better print resolution than neat PLA.
- Upon the addition of grafted PLA in the PLA/Clo5 composite, both the modulus of elasticity and the tensile strength increased, whereas the ductility remained unchanged. This observed increase could be attributed to the improved interfacial interaction/adhesion and wetting between PLA and Clo5 platelets, due to the grafted PLA acting as a bridge between the PLA and the clay fillers and resulting in mechanical reinforcement.
- A different behaviour was observed when grafted PLA was introduced into the PLA/GA system, with the tensile properties of MAH-g-PLA/PLA/GA being similar to those of the PLA/GA system. This could be due to the easier dispersion of GA particles in the polymer matrix being the dominant mechanical performance mechanism in this PLA/clay system.
- Varying the content of the grafted PLA in the PLA/GA system had no significant impact on the mechanical properties of the printed composite samples.

8.2 Original contribution to knowledge

Despite the fact that there are widespread activities in both additive manufacturing and in nanocomposite materials, little research has been reported in the literature that merges these two major technologies together. The current project is aimed at promoting this merging by producing new materials for mechanically reinforced 3D

printed parts. Combining polymer/clay nanocomposites with 3D printing could therefore facilitate new advances in both fields.

This thesis provides for the first time a systematic investigation of the effect of various clay types, including natural clay, organomodified Cloisite and Garamite, on the mechanical properties of 3D printed polymer/clay composites. For the same clay content, the new samples containing organoclay exhibited both a better modulus of elasticity and a better strength than the samples with natural clay.

The mechanical behaviour of the newly printed composite samples was also influenced significantly by the clay content. For example, the tensile modulus of the printed PLA/GA composites at 1wt% clay content was similar to that of neat PLA, whereas, at 5wt% clay content, the modulus was increased by 30%.

In addition, the Halpin-Tsai model was implemented in order to explain (and predict) the observed mechanical behaviour of the printed nanocomposite samples. Specifically, the model provided a correlation between the elastic modulus and the extent of intercalation within the composite samples. The research has revealed new results on how clay intercalation is more effective as a reinforcement technique than raising the total clay content.

Furthermore, MAH-g-PLA/PLA/clay composite systems were designed and developed in order to increase the quality of the clay dispersion in the polymer matrix and enhance the mechanical properties of the corresponding composites. The mechanism underlying the mechanical performance of the MAH-g-PLA/PLA/clay composites was dependent on the clay morphology of Cloisite and Garamite. This is particularly applicable in the design and development of feedstock filaments, as it provides a guideline for the selection of the clay type.

The research has generated new results on how the melt flow rate can be increased and the die swell ratio reduced by introducing Garamite into the polymer matrix. This has the practical benefit of showing how the composite feedstock filaments can be designed to provide better print resolution than neat PLA.

The current research has combined the knowledge from the growing field of 3D printing with that from the more established field of polymer nanocomposites. This has delivered new knowledge that can be exploited further in the 3D printing filament industry as, for example, in the production of printing filaments with lower die swelling than neat PLA. In more general terms, the research has extended and promoted a model that facilitates the design of new nanomaterials that lead to the fabrication of printed components with enhanced mechanical performance and structural integrity.

8.3 Recommendations

The properties of 3D printed objects are process-dependent, as shown in Chapter 4, where the effect of the three most important printing parameters on the mechanical properties was investigated. Hence, it is recommended that more print settings are investigated in the future.

Last but not least, the enhanced mechanical performance of the composites with grafted PLA could be studied further, through TEM images, which will provide more information on the precise mechanism that governs the interaction between the grafted PLA and the clay fillers. This could prove helpful in improving the design of such systems even further and delivering composites with enhanced mechanical performance.

References

1. Campbell, T. et al. Could 3D printing change the world? Strategic Foresight Report. Washington D.C., 2011. Available from: http://www.atlanticcouncil.org/images/files/publication_pdfs/403/101711_ACUS_3DPrinting.PDF [Accessed 13 February 2018]
2. Hubs, 3D. What is 3D Printing? The definitive guide. [no date]. Available from: https://www.3dhubs.com/what-is-3d-printing [Accessed 13 February 2018]
3. Wang, X. et al. 3D printing of polymer matrix composites: A review and prospective. Composites Part B: Engineering, 2017, 110, pp. 442–458.
4. De Leon, A.C. et al. High performance polymer nanocomposites for additive manufacturing applications. Reactive and Functional Polymers, 2016, 103, pp. 141–155.
5. Farahani, R.D. et al. Three-Dimensional Printing of Multifunctional Nanocomposites: Manufacturing Techniques and Applications. Advanced Materials, 2016, 28 (28), pp. 5794–5821.
6. Caspar de Vries. Volkswagen Autoeuropa: Maximizing production efficiency with 3D printed tools, jigs, and fixtures. Ultimaker 3D Printers, 2017. Available from: https://ultimaker.com/en/stories/43969-volkswagen-autoeuropa-

maximizing-production-efficiency-with-3d-printed-tools-jigs-and-fixtures [Accessed 14 February 2018]

7. Lana Lozova. 3D printing in landscape architecture and pool design. Ultimaker 3D Printers, 2017. Available from: https://ultimaker.com/en/stories/37401-3d-printing-in-landscape-architecture-and-pool-design [Accessed 14 February 2018]
8. Jones, R. et al. RepRap – the replicating rapid prototyper. Robotica, 2011, 187 (29), pp. 177–191.
9. Boparai, K.S. et al. Development of rapid tooling using fused deposition modeling: a review. Rapid Prototyping Journal, 2016, 22 (2), pp. 281–299.
10. Campbell, T.A. et al. 3D printing of multifunctional nanocomposites. Nano Today, 2013, 8 (2), pp. 119–120.
11. Weng, Z. et al. Mechanical and thermal properties of ABS/montmorillonite nanocomposites for fused deposition modeling 3D printing. Materials & Design, 2016, 102, pp. 276–283.
12. Shofner, M.L. et al. Nanofiber-reinforced polymers prepared by fused deposition modeling. Journal of Applied Polymer Science, 2003, 89 (11), pp. 3081–3090.
13. Lee, H. et al. TPO based nanocomposites. Part 1. Morphology and mechanical properties. Polymer, 2005, 46 (25), pp. 11673–11689.

14. Fornes, T.D., P.D. Modeling properties of nylon 6/clay nanocomposites using composite theories. Polymer, 2003, 44 (17), pp. 4993–5013.
15. Kontou, E. et al. Comparative study of PLA nanocomposites reinforced with clay and silica nanofillers and their mixtures. Journal of Applied Polymer Science, 2011, 122 (3), pp. 1519–1529.
16. Pirani, S.I. et al. Optimum loading level of nanoclay in PLA nanocomposites: Impact on the mechanical properties and glass transition temperature. Journal of Thermoplastic Composite Materials, 2013, 27 (11), pp. 1461–1478.
17. Zaidi, L. et al. Relationship between structure and rheological, mechanical and thermal properties of polylactide/Cloisite 30B nanocomposites. Journal of Applied Polymer Science, 2010, 116 (3), pp. 1357–1365.
18. Lai, S.-M. et al. Unusual mechanical properties of melt-blended poly(lactic acid) (PLA)/clay nanocomposites. European Polymer Journal, 2014, 52, pp. 193–206.
19. Müller, K. et al. Review on the Processing and Properties of Polymer Nanocomposites and Nanocoatings and Their Applications in the Packaging, Automotive and Solar Energy Fields. 2017, 7.
20. Petersson, L. et al. Using maleic anhydride grafted poly(lactic acid) as a compatibilizer in poly(lactic acid)/layered-silicate nanocomposites. Journal of Applied Polymer Science, 2006, 102 (2), pp. 1852–1862.

21. Ahmadi, S. et al. Acoustic Performance of 3D Printed Nanocomposite Earmuff. Global journal of health science, 2015, 8 (1), p. 45157.
22. Francis, V. et al. Experimental investigations on fused deposition modelling of polymer-layered silicate nanocomposite. Virtual and Physical Prototyping, 2016, pp. 1–13.
23. Abdul Haq, R.H. et al. Fused Deposition Modeling of PCL/HA/MMT Biocompatible Polymer Nano-composites. In: In: Öchsner A., A. H. (eds) (ed.) Machining, Joining and Modifications of Advanced Materials. Advanced Structured Materials. Springer, Singapore, 2016, pp. 23–32. DOI: 10.1007/978-981-10-1082-8_3
24. Coppola, B. et al. Layered silicate reinforced polylactic acid filaments for 3D printing of polymer nanocomposites. In: 2017 IEEE 3rd International Forum on Research and Technologies for Society and Industry (RTSI). IEEE, 2017, pp. 1–4.
25. EY. If 3D printing has changed the industries of tomorrow, how can your organization get ready today? 2016. Available from: http://www.ey.com/Publication/vwLUAssets/Accelerate_your_3D_technology_journey_in_oil_and_gas/$FILE/ey-3dprinting-journey-oil-and-gas.pdf [Accessed 8 November 2017]
26. EY. How will 3D printing make your company the strongest link in the value chain? 2016. Available from: http://www.ey.com/Publication/vwLUAssets/ey-global-3d-

printing-report-2016-full-report/$FILE/ey-global-3d-printing-report-2016-full-report.pdf [Accessed 8 November 2017]

27. Sculpteo. The state of 3D printing. 2017. Available from: https://www.sculpteo.com/media/ebook/State of 3DP 2017_1.pdf [Accessed 8 November 2017]
28. Turner, B.N. et al. A review of melt extrusion additive manufacturing processes: II. Materials, dimensional accuracy, and surface roughness. Rapid Prototyping Journal, 2015, 21 (3), pp. 250–261.
29. N. Turner, B. et al. A review of melt extrusion additive manufacturing processes: I. Process design and modeling. Rapid Prototyping Journal, 2014, 20 (3), pp. 192–204.
30. Ford, S. et al. Additive manufacturing and sustainability: an exploratory study of the advantages and challenges. Journal of Cleaner Production, 2016, 137, pp. 1573–1587.
31. Lanzotti, A. et al. The impact of process parameters on mechanical properties of parts fabricated in PLA with an open-source 3-D printer Eujin Pei, D. (ed.). Rapid Prototyping Journal, 2015, 21 (5), pp. 604–617.
32. Casavola, C. et al. Orthotropic mechanical properties of fused deposition modelling parts described by classical laminate theory. Materials & Design, 2016, 90, pp. 453–458.
33. Carneiro, O.S. et al. Fused deposition modeling with polypropylene. Materials & Design, 2015, 83, pp. 768–776.

34. Tymrak, B.M. et al. Mechanical properties of components fabricated with open-source 3-D printers under realistic environmental conditions. Materials & Design, 2014, 58, pp. 242–246.
35. Wittbrodt, B. et al. The Effects of PLA Color on Material Properties of 3-D Printed Components. Additive Manufacturing, 2015, 8, pp. 110–116.
36. Senatov, F.S. et al. Mechanical properties and shape memory effect of 3D-printed PLA-based porous scaffolds. Journal of the mechanical behavior of biomedical materials, 2015, 57, pp. 139–148.
37. Espalin, D. et al. Fused deposition modeling of patient-specific polymethylmethacrylate implants Bourell, D. (ed.). Rapid Prototyping Journal, 2010, 16 (3), pp. 164–173.
38. Ahn, S.-H. et al. Anisotropic material properties of fused deposition modeling ABS. Rapid Prototyping Journal, 2002, 8 (4), pp. 248–257.
39. Ziemian, S. et al. Tensile and fatigue behavior of layered acrylonitrile butadiene styrene. Rapid Prototyping Journal, 2015, 21 (3), pp. 270–278.
40. Wu, W. et al. Influence of Layer Thickness and Raster Angle on the Mechanical Properties of 3D-Printed PEEK and a Comparative Mechanical Study between PEEK and ABS. Materials, 2015, 8 (9), pp. 5834–5846.
41. Constance Ziemian, Mala Sharma, S.Z. Anisotropic Mechanical Properties of ABS Parts Fabricated by Fused Deposition Modelling. In:

Dr. Murat Gokcek (ed.) Mechanical Engineering. InTech, 2012. DOI: 10.5772/2397

42. Torres, J. et al. An approach for mechanical property optimization of fused deposition modeling with polylactic acid via design of experiments. Rapid Prototyping Journal, 2016, 22 (2), pp. 387–404.
43. Jaya Christiyan, K.G. et al. Flexural Properties of PLA Components Under Various Test Condition Manufactured by 3D Printer. In: Journal of The Institution of Engineers (India): Series C. Springer India, 2016, pp. 1–5.
44. Song, Y. et al. Measurements of the mechanical response of unidirectional 3D-printed PLA. Materials & Design, 2017, 123, pp. 154–164.
45. Dawoud, M. et al. Mechanical behaviour of ABS: An experimental study using FDM and injection moulding techniques. Journal of Manufacturing Processes, 2016, 21, pp. 39–45.
46. Ferreira, R.T.L. et al. Experimental characterization and micrography of 3D printed PLA and PLA reinforced with short carbon fibers. Composites Part B: Engineering, 2017, 124, pp. 88–100.
47. Dul, S. et al. Fused deposition modelling with ABS–graphene nanocomposites. Composites Part A: Applied Science and Manufacturing, 2016, 85, pp. 181–191.
48. Torrado, A.R. et al. Characterizing the effect of additives to ABS on the mechanical property anisotropy of specimens fabricated by

material extrusion 3D printing. Additive Manufacturing, 2015, 6, pp. 16–29.

49. Ning, F. et al. Additive manufacturing of carbon fiber reinforced thermoplastic composites using fused deposition modeling. Composites Part B: Engineering, 2015, 80, pp. 369–378.
50. Mohamed, O.A. et al. Optimization of fused deposition modeling process parameters: a review of current research and future prospects. Advances in Manufacturing, 2015, 3 (1), pp. 42–53.
51. Raquez, J.-M. et al. Polylactide (PLA)-based nanocomposites. Progress in Polymer Science, 2013, 38 (10–11), pp. 1504–1542.
52. Olad, A. Polymer/Clay Nanocomposites. In: Dr. Boreddy Reddy (Ed.) (ed.) Advances in Diverse Industrial Applications of Nanocomposites. InTech, 2011. Available from: http://www.intechopen.com/books/advances-in-diverse-industrial-applications-of-nanocomposites/polymer-clay-nanocomposites [Accessed 24 October 2015]
53. Paul, D.R. et al. Polymer Nanotechnology: Nanocomposites. Polymer, 2008, 49 (15), pp. 3187–3204.
54. Andreas Trepte. File:Montmorillonit.svg -. Wikimedia Commons, 2006. Available from: https://commons.wikimedia.org/wiki/File:Montmorillonit.svg [Accessed 28 February 2018]

55. Fornes, T.D. et al. Nylon 6 nanocomposites: the effect of matrix molecular weight. Polymer, 2001, 42 (25), pp. 09929–09940.
56. Fornes, T.D. et al. Formation and properties of nylon 6 nanocomposites. Polímeros, 2003, 13 (4), pp. 212–217.
57. Jiang, L. et al. Comparison of polylactide/nano-sized calcium carbonate and polylactide/montmorillonite composites: Reinforcing effects and toughening mechanisms. Polymer, 2007, 48 (26), pp. 7632–7644.
58. Ariff, Z.M. et al. Rheological Behaviour of Polypropylene Through Extrusion and Capillary Rheometry. In: Dr. Fatih Dogan (ed.) Polypropylene. InTech, 2012. DOI: 10.5772/36395
59. Chow, W. et al. Effects of maleated-PLA compatibilizer on the properties of poly(lactic acid)/ halloysite clay composites. Journal of Thermoplastic Composite Materials, [no date], 26 (10), pp. 1349–1363.
60. BYK Additives & Instruments. Modifiers for Wood Plastic Composites (WPC). [no date]. Available from: https://www.byk.com/fileadmin/byk/additives/highlights/additives_for_thermoplastics/BYK_TP-A1_WPC_Modifiers_EN_1_.pdf [Accessed 2 March 2018]
61. Madhavan Nampoothiri, K. et al. An overview of the recent developments in polylactide (PLA) research. Bioresource Technology, 2010, 101 (22), pp. 8493–8501.

62. Haq, R.H.A. et al. Fabrication Process of Polymer Nano-Composite Filament for Fused Deposition Modeling. Applied Mechanics and Materials, 2013, 465–466, pp. 8–12.
63. Ryan, J. et al. Mechanical characterization of 3D-printed polymers. Additive Manufacturing, 2018, 20, pp. 44–67.
64. Wong, A.C.-Y. Factors affecting extrudate swell and melt flow rate. Journal of Materials Processing Technology, 1998, 79 (1–3), pp. 163–169.
65. Detyothin, S. et al. Effects of molecular weight and grafted maleic anhydride of functionalized polylactic acid used in reactive compatibilized binary and ternary blends of polylactic acid and thermoplastic cassava starch. Journal of Applied Polymer Science, 2015, 132 (28), p. 42230.
66. NatureWorks. IngeoTM Biopolymer 2003D Technical Data Sheet For Fresh Food Packaging and Food Serviceware. [no date]. Available from: http://www.natureworksllc.com/~/media/Technical_Resources/Technical_Data_Sheets/TechnicalDataSheet_2003D_FFP-FSW_pdf.pdf [Accessed 22 November 2016]
67. NatureWorks. IngeoTM Biopolymer 3251D Technical Data Sheet Injection Molding Process Guide. [no date]. Available from: http://www.natureworksllc.com/~/media/Technical_Resources/Te

chnical_Data_Sheets/TechnicalDataSheet_3251D_injection-molding_pdf.pdf [Accessed 22 November 2016]

68. Hossain, K.M.Z. et al. The effect of cellulose nanowhiskers on the flexural properties of self-reinforced polylactic acid composites. Reactive and Functional Polymers, 2014, 85, pp. 193–200.
69. BYK-Chemie GmbH. CLOISITE-5. [no date]. Available from: https://www.byk.com/en/additives/additives-by-name/cloisite-5.php [Accessed 22 November 2016]
70. BYK-Chemie GmbH. CLOISITE-20. [no date]. Available from: https://www.byk.com/en/additives/additives-by-name/cloisite-20.php [Accessed 22 November 2016]
71. BYK-Chemie GmbH. CLOISITE-116. [no date]. Available from: https://www.byk.com/en/additives/additives-by-name/cloisite-116.php [Accessed 22 November 2016]
72. BYK Chemie GmbH. GARAMITE-1958. [no date]. Available from: https://www.byk.com/en/additives/additives-by-name/garamite-1958.php [Accessed 7 March 2018]
73. ASTM International. D638-10, Standard Test Method for Tensile Properties of Plastics. 2010. DOI: 10.1520/D0638-10
74. Standardization, I. organization for. ISO 178:2003 - Plastics -- Determination of flexural properties. 2003. Available from: https://www.iso.org/standard/45091.html [Accessed 19 March 2018]

75. Independent t-test in SPSS Statistics. [no date]. Available from: https://statistics.laerd.com/spss-tutorials/independent-t-test-using-spss-statistics.php [Accessed 25 April 2018]
76. Statistics, L. One-way ANOVA in SPSS Statistics. [no date]. Available from: https://statistics.laerd.com/spss-tutorials/one-way-anova-using-spss-statistics.php [Accessed 25 April 2018]
77. Laerd Statistics. One-way ANOVA. [no date]. Available from: https://statistics.laerd.com/statistical-guides/one-way-anova-statistical-guide.php [Accessed 25 April 2018]
78. Yeager, K. SPSS Tutorials: One-Way ANOVA. Kent State University, University Libraries, [no date]. Available from: https://libguides.library.kent.edu/SPSS/OneWayANOVA [Accessed 25 April 2018]
79. Faherty, V.E. One-Way Analysis of Variance (ANOVA) with Post Hoc Tests. In: Compassionate Statistics: Applied Quantitative Analysis for Social Services, with exercises and instructions in SPSS. California, United States: SAGE Publications, Inc., [no date], pp. 231–246. DOI: 10.4135/9781483329543.n14
80. Yeager, K. SPSS Tutorials: Independent Samples t Test. Kent State University, University Libraries, [no date]. Available from: https://libguides.library.kent.edu/SPSS/IndependentTTest [Accessed 25 April 2018]

81. Rodríguez, J.F. et al. Mechanical behavior of acrylonitrile butadiene styrene (ABS) fused deposition materials. Experimental investigation. Rapid Prototyping Journal, 2001, 7 (3), pp. 148–158.
82. Halpin, J.C. Stiffness and Expansion Estimates for Oriented Short Fiber Composites. Journal of Composite Materials, 1969, 3 (4), pp. 732–734.
83. Chen, B. et al. A critical appraisal of polymer-clay nanocomposites. Chem. Soc. Rev., 2008, 37 (3), pp. 568–594.
84. Chen, B. et al. Elastic moduli of clay platelets. Scripta Materialia, 2006, 54, pp. 1581–1585.
85. Pavlidou, S. et al. A review on polymer–layered silicate nanocomposites. Progress in Polymer Science, 2008, 33 (12), pp. 1119–1198.
86. Paspali, A. et al. The influence of nanostructure on the mechanical properties of 3D printed polylactide/nanoclay composites. Composites Part B: Engineering, 2018, 152, pp. 160–168.
87. Ingram, S. et al. Influence of clay type on exfoliation, cure and physical properties of in situ polymerised poly(methyl methacrylate) nanocomposites. Polymer International, 2008, 57 (10), pp. 1118–1127.
88. Bellehumeur, C. et al. Modeling of Bond Formation Between Polymer Filaments in the Fused Deposition Modeling Process. Journal of Manufacturing Processes, 2004, 6 (2), pp. 170–178.

Appendix

Material database

Fillers	Matrix	Application
Alumina	ABS	For studying mechanical anisotropy [1]
Carbon fibres	ABS	Mechanical reinforcement [2]
Carbon nanofibres	ABS	Mechanical reinforcement [3]
Copper & iron particles	ABS	Large-scale printing of metal structures [4]
Graphene	ABS, PLA	Mechanical & conductivity enhancement [5]
HA	PLA	Biomaterials for porous scaffolds [6]
Jute fibres	ABS	New feedstock materials [7]
Multi-wall carbon nanotubes	Polyolefin	Conductivity [8]
Nanoclay	ABS	Attenuation performance [9]
Nanoclay & HA	PCL	New feedstock materials [10]
Organoclay	ABS	For studying mechanical anisotropy [1]
Titania particles	ABS	New feedstock materials [7]
Tricalcium phosphate	PP	Bioresorbable ceramics [11]
Tungsten particles	PC	X-ray shielding [12]
Zinc oxide nanorods	ABS	For studying mechanical anisotropy [1]

1 Torrado, A.R. *et al. Additive Manufacturing*, 2015, 6, pp. 16–29. DOI: 10.1016/j.addma.2015.02.001

2 Ning, F. *et al. Composites Part B: Engineering*, 2015, 80, pp. 369–378. DOI: 10.1016/j.compositesb.2015.06.013

3 Shofner, M.L. *et al. Journal of Applied Polymer Science*, 2003, 89 (11), pp. 3081–3090. DOI: 10.1002/app.12496

4 Hwang, S. *et al. Journal of Electronic Materials*, 2014, 44 (3), pp. 771–777. DOI: 10.1007/s11664-014-3425-6

5 Wei, X. *et al. Scientific reports*, 2015, 5, p. 11181. DOI: 10.1038/srep11181

6 Senatov, F.S. *et al. Journal of the mechanical behavior of biomedical materials*, 2015, 57, pp. 139–148. DOI: 10.1016/j.jmbbm.2015.11.036

7 Torrado Perez, A.R. *et al. Journal of Failure Analysis and Prevention*, 2014, 14 (3), pp. 343–353. DOI: 10.1007/s11668-014-9803-9

8 Daver, F. *et al. Composites Part A: Applied Science and Manufacturing*, 2016, 80, pp. 13–20. DOI: 10.1016/j.compositesa.2015.10.002

9 Ahmadi, S. *et al. Global journal of health science*, 2015, 8 (1), p. 45157. DOI: 10.5539/gjhs.v8n1p180

10 Haq, R.H.A. *et al. Applied Mechanics and Materials*, 2013, 465-466, pp. 8–12. DOI: 10.4028/www.scientific.net/AMM.465-466.8

11 Kalita, S.J. *et al. Materials Science and Engineering: C*, 2003, 23 (5), pp. 611–620. DOI: 10.1016/S0928-4931(03)00052-3

12 Shemelya, C.M. *et al. Journal of Electronic Materials*, 2015, 44 (8), pp. 2598–2607. DOI: 10.1007/s11664-015-3687-7